



**Max-Planck-Institut für Metallforschung
Stuttgart**

Influence of nanomaterials on cell function

Furong Tian

Dissertation
an der
Universität Stuttgart

Bericht Nr. 181
Januar 2006

Influence of nanomaterials on cell function

Von der Fakultät Chemie der Universität Stuttgart

Zur Erlangung der Würde eines

Doktors der Naturwissenschaften (Dr. rer. nat.)

genehmigte Abhandlung

vorgelegt von

FURONG TIAN

aus China

Hauptberichter: Prof. Dr. E. Arzt

Mitberichter: Prof. Dr. J. Spatz

Tag der Einreichung: 10. November 2005

Tag der Prüfung: 12. Januar 2006

MAX-PLANCK-INSTITUT FÜR METALLFORSCHUNG STUTTGART

2006

“For a successful technology, reality must take precedence over public relations, for Nature cannot be fooled”

Dick Feynman

Parts of this thesis were published in the following papers:

1. Tian F.R., Cui D., Schwarz H. and Estrada G. Influence of different size carbon materials on human Fibroblasts. The 4th world congress of the world society of *Cellular and molecular biology*TM 2005, 88.
2. Tian F.R., Nakahara T. and Miyakoshi J. Transitorily influence of magnetic fields and ionizing radiation on c-jun, c-fos and BRCA1. *Bull. Health Sci. Hirosaki*, 2005, 4, 123-128.
3. Cui D., Tian F.R., Kong Y., Titushikin I. and Gao H., Effects of single walled Carbon nanotubes on the polymerase chain reaction. *Nanotechnology* 2004, 15, 154-157.
4. Cui D., Tian F.R., Ozkan C.S., Wang M. and Gao H. Effect of single wall carbon nanotubes on human HEK293 cells. *Toxicology Letters* 2005, 155, 73-85.
5. Cui D., Jin G., Gao T., Sun T., Tian F.R., Estrada G., Gao H. and Sarai A. Characterization of BRCAA1 and its novel antigen epitope identification. *Cancer Epidemiology, biomarkers and prevention* 2004, 13, 1136-1145.

Contents

	List of abbreviations	13
	Summary	15
Chapter 1	General introduction	17
1.1	Nanoscale materials	17
1.2	Carbon nanotubes	18
1.2.1	Carbon nanotube application in biology	19
1.2.2	Influence of carbon nanotube on cells and tissues	20
1.3	Nanostructures	20
	Nanostructures in biology	
Chapter 2	Effects of single wall carbon nanotubes on PCR	21
2.1	Introduction	22
2.1.1	Parameters influencing the yield and specificity of PCR	22
2.1.2	Purification of SWCNTs	24
2.1.3	XPS - X-ray photoelectron spectroscopy	25
2.2	Materials and methods	26
2.2.1	XPS analysis	26
2.2.2	PCR preparation	27
2.2.3	Pt-labeled DNA fragment preparation and observation	27
2.3	Results and discussion	30
2.4	Conclusion	32
Chapter 3	Cytotoxicity of single wall carbon nanotube on human fibroblasts	33
3.1	Introduction	34
3.1.1	Influence of carbon nanotubes and associated nanomaterials on human cells and environment	34
3.1.2	Extracellular signals	36
3.2	Materials and methods	37
3.2.1	Types of particle	37
3.2.2	Cell culture	37
3.2.3	Cell survival assay	38
3.2.4	Specimen preparation for TEM and observation	39
3.2.5	Scanning electron microscopy	39
3.2.6	Immunocytochemical analysis	40
3.2.7	Western blot analysis	40
3.2.8	Cell death assay	40
3.2.9	Statistical analysis	41
3.3	Results	42
3.3.1	Influences of the different materials on cell survival	42

3.3.2	Cell death assays	42
3.3.3	Effect of SWCNT on cell morphology	44
3.3.4.1	Immunostaining assays	46
3.3.4.2	Western blot assays	47
3.4	Discussion	49
Chapter 4	Effect of single wall carbon nanotube on human HEK293 cells	52
4.1	Introduction	53
4.1.1	Apoptosis and cell cycle progression	53
4.2	Materials and methods	54
4.2.1	Antibodies	55
4.2.2	Cell viability and proliferation assay	55
4.2.3	Detection of adhesion ability	55
4.2.4	Observation under scanning electron microscopy	55
4.2.5	DNA fragmentation	55
4.2.6	Flow cytometry analysis	55
4.2.7	SDS-PAGE analysis and western blot analysis	56
4.2.8	Immunofluorescent staining analysis	56
4.2.9	Microarray analysis	56
4.2.9.1	Fabrication of microarrays	56
4.2.9.2	Hybridization and washing	57
4.2.9.3	Detection and analysis	57
4.2.10	Data analysis	57
4.3	Results	58
4.3.1	Effect of SWCNTs on the viability and proliferation of HEK293 cells	59
4.3.2	Effect of SWCNTs on cell adhesion	60
4.3.3	Induction of apoptosis of HEK293 cells by SWCNTs	61
4.3.4	Effect of SWCNTs on adhesive proteins and cyclin D3 in HEK293 cells	58
4.3.5	Active responses of HEK293 cells to SWCNTs	64
4.3.6	Gene expression profile between HEK293 cells with or without SWCNTs by oligonucleotide microarrays	65
4.4	Discussion	67
Chapter 5	Binding RGD to a nanostructured hydrogel	70
5.1	Introduction	70
5.1.1	Polymers	70
5.1.2	Cell adhesion and the extracellular matrix	72
5.1.3	RGD Peptides on the surface	72
5.1.4	Immobilization of RGD and proteins on the surface	73

5.2	Proceduce of immobilization RGD on nanostructured hydrogel	75
5.2.1	Gold dot nanostructures	77
5.2.1.1	Diblock copolymer micelles	77
5.2.1.2	Calculation of the quantity of gold acid	77
5.2.1.3	Formation of thin polymer films	77
5.2.1.4	Tessellations in micelles order	78
5.2.1.5	Reduction and deposition of metal clusters	79
5.2.2	Preparation of polymers	80
5.3	Analytics	82
5.3.1	Detection of nanopatterned surfaces	82
5.3.2	Cryo SEM observation of nanostructured surfaces	83
5.4	Materials and methods	83
5.4.1	Nanopatterned glass substrate preparation	83
5.4.2	Polymer preparation	83
5.4.2.1	PEG (Mw=800kDa)	84
5.4.2.2	PEG (Mw=700kDa)	85
5.4.2.3	PEG (Mw=575kDa)	86
5.4.3	Sterilization of hydrogels	87
5.5	Results and discussion	87
5.5.1	Nanosturctures on glass surface	88
5.5.2	Micro and nanostructures on hydrogel	88
5.6	Conclusion	90
Chaper 6	Cell adhesion on Nanostructured hydrogel	91
6.1	Introduction	92
6.2	Materials and methods	93
6.2.1	General methods for cell culture	94
6.2.2	Cell counting	94
6.2.3	Observation under phase contrast microscopy	96
6.3	Results	96
6.3.1	Cell spreading on PEG gel	96
6.3.2	Cell adhesion on PEG gel modulated by the distance between RGD-nanodots	96
6.4	Discussion	97
	Zusammenfassung	101
	Appendix	108
	Acknowledgements	132
	Curriculum vitae	134
	Reference	135

List of abbreviations

3D	=	Three dimensional
AFM	=	Atomic force microscopy
ANOVA	=	One-way analysis of variance
CAMs	=	Cell-adhesion molecules
DAPI	=	4', 6-diamidino-phenylindole
DMEM	=	Dulbeccos modified Eagle medium
HEK293 cells	=	Human embryo kidney cells
ECM	=	Extracellular matrix
Ig	=	Immunoglobulin
MTT	=	3-(4,5-Dimethylthiazol-z-yl)-2,5-dipheny-tetrazotium bromide
PBS	=	Phosphate-buffered saline
P2VP	=	Poly-2-vinylpyridine
PS	=	Polystyrene
NHS	=	N-hydroxysuccinimide
RGD	=	Arg-Gly-Asp
PA	=	Polyacrylamide
PDMS	=	Poly(dimethylsiloxane)
PEG	=	Polyethylene glycols
PEGDA	=	PEG Diacrylats
PCR	=	Polymerase chain reaction
PVDF	=	Polyvinylidene di-fluoride
SDS-PAGE	=	Sodium dodecyl sulfate-polyacrylamide gel electrophoresis
SAM	=	Self-assembled monolayer
SWCNT	=	Single wall carbon nanotube
TAE	=	Eicosapentaenoic acid
TEM	=	Transmission electron microscopy
SEM	=	Scanning electron microscopy
XPS	=	X-ray photoelectron spectroscopy

Summary

The intention of this work was to study the mechanisms of the interactions between nanomaterials and cells. The experiments carried out during this thesis focused on two kinds of nanomaterials: single wall carbon nanotube (SWCNT) and nanostructured hydrogels. The biological applications of novel nanomaterials that have emerged in this field during the past decade are illustrated with the help of selected examples and discussed. Different approaches for the description of the interactions of nanomaterials and cells are described in chapters 2 to 6. The influences of SWCNT are shown in chapters 2 to 4. Nanostructured hydrogels were created with the use of lithographic techniques. The application of these hydrogels is described in chapters 5 and 6.

Chapter 1 provides a general introduction to the field of nanomaterials such as SWCNT and nanostructured hydrogels.

In chapter 2, the effects of SWCNT on the polymerase chain reaction (PCR) are investigated via quantitative PCR product measurements using scanning electron microscopy (SEM), high-resolution transmission electron microscopy (HRTEM) and X-ray photoelectron spectroscopy (XPS). The measurements show that adding SWCNTs to the reaction liquid increase the amount of PCR product at SWCNT concentrations below 3 $\mu\text{g}/\mu\text{l}$, but have a reversed effect at higher SWCNT concentrations. Similar results were obtained in PCR reactions with or without Mg^{2+} additive. Both SEM and HRTEM measurements show that the DNA templates and Taq enzymes are attached to bundles of SWCNTs in PCR products. XPS spectra show that the C 1s binding energy in PCR products increased after the reaction because of the emergence of two new peaks beside the main peak, if compared with carbon nanotubes before the reaction. This suggests a chemical reaction between the SWCNT and the PCR components. SWCNT may increase the PCR efficiency at a concentration range of less than 3 $\mu\text{g}/\mu\text{l}$ in the reaction liquid and have the potential to act as catalysts in a variety of biochemical reactions.

Chapter 3 shows a systematic study on human fibroblasts in the presence of refined CNTs with different geometries and sizes. The results were compared to other carbon materials. Particularly the cell survival has been studied with five kinds of carbon materials. In increasing order these are: i) SWCNT, ii) active carbon, iii) carbon black, iv) multiwall carbon nanotubes, and finally, v) carbon graphite. Interestingly, we found a strong size, time, and dose effect of carbon materials upon the cell survival. Furthermore, we observed that lower concentrations of SWCNTs than those reported in the literature induce cell death. Since

carbon materials disturb cell membranes, thereby inducing cells to detach from substrates, we measured the expression of cell adhesion related proteins, such as Laminin, Collagen-IV, Fibronectin, P-Cadherin and focal adhesion kinase. Finally, a biological mechanism that explains why smaller particles (e.g. SWCNT) have more influence is presented.

In chapter 4, the influence of SWCNT on human HEK293 cells is investigated with the aim of exploring SWCNTs biocompatibility. Results of dose and time dependent experiments show that SWCNTs can inhibit HEK293 cell proliferation and decrease the cell adhesive abilities. HEK293 cells exhibit active responses to SWCNT such as secretion of several 20–30 kD proteins to wrap SWCNTs, aggregation of cells attached by SWCNTs and formation of nodular structures. Cell cycle analysis showed that 25 $\mu\text{g/ml}$ SWCNTs induced G1 arrest and cell apoptosis in HEK293 cells. Biochip analysis showed that SWCNTs can induce up-regulation expression of cell cycle-associated genes such as *p16*, *bax*, *p57*, *hrk*, *cdc42* and *cdc37*, down-regulation expression of cell cycle genes such as *cdk2*, *cdk4*, *cdk6* and *cyclin D3*, and down-regulation expression of signal transduction associated genes such as *mad2*, *jak1*, *ttk*, *pcdha9* and *erk*. Western blot analysis showed that SWCNTs can induce down-regulation expression of adhesion-associated proteins such as laminin, fibronectin, cadherin, FAK and collagen IV. In conclusion, SWCNTs can inhibit HEK293 cell growth by inducing cell apoptosis and decreasing cellular adhesion abilities.

In chapter 5 a new lithographic method is developed, employing a thiol linker to transfer nanostructures to soft materials. The particles form extended hexagonal patterns of Au-nanoparticles on hydrogel showing the same arrangement as nanopatterns on the glass slide. Further improvement in the preparation of hydrogel allows the transfer of nanostructures without losing the hexagonal order. The structure and density of nanostructured hydrogels is controlled by Au nanoparticle patterning on solid substrates. This method provides a nanomask to control the position and connect the molecule (e.g. RGD) to the polymer surfaces. The nanostructured hydrogel is employed as cell adhesive templates, demonstrating the successful application of micellar nano- and soft lithography techniques to various research fields. For example, this method provides a way for study of interaction between cells and substrate deformation.

In chapter 6, the cell adhesion has been investigated on the nanostructured hydrogel, which can be controlled by diblock polymer micelle and polymer swelling. This approach has revealed that the distance between RGD strongly controls cell adhesion and that large distances between RGD hamper cell adhesion. Previous studies showed that cell attachment, growth and differentiation depends on the distance between gold nanodots. The same relationship between cell behaviour and dots distance was observed when cells were plated and grown on a soft nanostructured surfaces.

Chapter 1

General Introduction

A nanometer (nm) is one thousand millionth of a meter. For comparison, a single human hair is about 80,000 nm wide, a red blood cell is approximately 7,000 nm wide and a water molecule is almost 0.3 nm wide. Nanomaterials can be produced in one dimension (e.g. nanowires and nanotubes), in two dimensions (e.g. thin surface coatings) or in all three dimensions (e.g. nanoparticles). Nanomaterials are attractive, because their properties which are very different from those of materials at a large scale¹.

1.1 Nanoscale materials

Current applications of nanoscale materials include electronics and active surfaces. Flexible display screens as electronic devices are already being explored. Much interest is also focused on quantum dots and semiconductor nanoparticles in fluorescent biological labels² or solar energy cells³.

Applications of nanomaterials in medicine are especially promising. Areas such as disease diagnosis, drug delivery targeted at specific sites in the body and molecular imaging are being intensively investigated and some products are undergoing clinical trials. Materials and devices, such as scaffolds for cell and tissue engineering can be produced at nanoscale^{4,5}.

Recently, biological applications of novel nanomaterials have drawn great attention. The aim of the present work is to study the influence of nanomaterials on cell function, therefore, it is convenient to review the appropriate background. In the following section, the carbon nanotubes and nanostructures in biology will be discussed.

1.2 Carbon nanotubes

In short, the history of nanotube has three main events. Firstly, fullerene and carbon nanotube (CNT) as nanomaterials were discovered by Kroto and Iijima research teams respectively in 1985 and 1991^{6,7}. Secondly, Lee's research team invented a band gap modulation of carbon nanotubes by encapsulating metal fullerenes in 2001⁸. Thirdly, Iijima built logic gates and memory cells based on C60/nanotube electromechanical transistors in 2000⁹. The large length (up to several microns) and small diameter (a few nanometres) of CNT result in a large aspect ratio. They can nearly be seen as the one-dimensional form of fullerenes. Therefore, these materials are expected to possess additional interesting electronic, mechanic and molecular properties. Especially in the beginning of these research, all theoretical studies on

carbon nanotubes were focused on molecular and electronic properties of a nearly one-dimensional structure.

1.2.1 Carbon nanotube application in biology

Carbon nanotubes (CNTs) have been intensively investigated over the last years because of growing interests in their unique properties for molecular electronics and biological sensors¹⁰. CNTs, for example, have been used as AFM tips to obtain atomic-resolution imaging of biological molecules such as DNA and proteins^{11, 12, 13}. Moreover, DNA and protein molecules can be immobilized on the surface of carbon nanotubes^{14, 15, 16}. CNT can be filled with target DNA molecules or peptides, and can potentially deliver target DNA molecules or peptides into special tissue regions to treat diseases¹⁷. It is broad of interest to explore methods to enhance the efficiency of the PCR efficiency. Chapter 2 describes the parameters influencing the yield of polymerase chain reaction (PCR) and the new application of nanotube on PCR.

1.2.2 Influence of Carbon Nanotube on cells and tissues

Nowadays, nanotube-like materials are produced in hundreds of kilograms every day and thus raise health concerns^{18, 19}. Only a few reports exist so far on how carbon nanotubes interact with and affect living systems. Recently, two groups reported carbon nanotubes which can deliver drugs into cells^{20, 21}. Those studies on animals have however revealed a positive association between exposure to SWCNT and pulmonary diseases. Furthermore, other experiments have shown that unrefined SWCNT may lead to dermal toxicity^{22, 23}. Recently, the Royal Society and the Royal Academy of Engineering, commissioned by the UK Government, issued a report on nanotechnologies¹. The report admits the many uncertainties around health, safety and environmental impact of nanoparticles. Other authors have mentioned that further research has to be done into the toxicity, epidemiology, persistence and bioaccumulation of nanoparticles^{24, 25}. Investigating the effects of carbon nanotubes on cells and their interaction mechanism is therefore very important. The Chapter 3 describes the influence of carbon nanotubes and associated carbon nanomaterials on human cells and environment. The influences of different geometries and sizes on the cell are investigated through five materials. Chapter 4 introduces the apoptosis and cell cycle. The interaction mechanism between carbon nanotubes and human cells is studied by morphological observation, Western blot, flow cytometry, immunofluorescent analysis and biochip analysis in Chapter 4.

1.3 Nanostructures

Nanostructures are used in several fields, such as physics, physical chemistry, materials science, chemical engineering and electrical engineering²⁶. The nanostructures with metal nanoparticles of different size and composition can be exploited to construct numerous sensing, electronic, optoelectronic and photo electronic devices. Recently, high efficiency multijunction photovoltaic cells have been developing on semiconductor nanostructured arrays³. Nano-scale control of photons could help us to create extremely low consumption optical device and quantum computer²⁷.

Nanostructures in biology

Several nanostructures have been subject of extensive research in biology. Recently, optical nanoparticles such as CdSe, InAs, ZnSe have been linked as nanopattern on semiconductor surface²⁸. Nanostructure encompasses elements of biochemistry, chemical biology, and molecular biology. These methods help to improve the technology of DNA biochip arrays and protein chips which are essential for effective drug discover or early detection of diseases³.

The responses of cells to topographical features have been known for decades²⁹. Many research groups succeeded to control the cell locations on surfaces by patterning a substrate on micrometer scale³⁰. However, the lack of a higher resolution patterning method prevented a direct examination of the range of sizes within focal adhesions³¹. Moreover, the nanometer scale allows a spatial control of a small number of chemical units and also for probing cell adhesion on a molecular scale. Recently, the photolithography and electron beam lithography have been widely used for biological questions and biotechnology industry. Cell growth and viability could be controlled by the ligand density, orientation and especially spacing at length scales from 10-200 nm³².

There are many kinds of soft tissues, such as skin, muscle, cardiovascular tissues and joints. The response of cells on soft materials has been intensively studied. The cell adhesion is affected by a number of material properties, such as elasticity, surface chemistry and topography³³. One of such properties, elastic modulus, has been increasingly recognized as a key factor in a number of cellular processes, ranging from motility to phagocytosis and differentiation^{34, 35, 36}. For example, a linear relationship between cell adhesion and elastic modulus of substrates is reported³⁷. Bell shaped cell spreading curves modelled by couple ligand density have appeared in the literature³⁸. They conclude that the ligand density also plays an important role in cell adhesion. The quantitation of ligand concentration actually on the substrate is quite difficult to control. How do we control ligand densities?

The Spatz group developed pattern surfaces with regularly spaced gold nano dots³⁹. This technique has been successfully employed to study cell adhesion⁴⁰. Thus, ligand densities can be controlled by nanostructured surface. We want to study the cell response on substrates due to two factors: substrate elasticity and nanostructured surface. Chapter 5 describes how material properties affect cells and the link between RGD and nanostructured hydrogel. The cell behavior on the soft nanostructures is shown in the chapter 6.

Chapter 2

Effects of single wall carbon nanotube on PCR

2.1 Introduction

Nanoscale materials have recently attracted much attention. In particular, single wall carbon nanotube (SWCNT), has been a subject of intense investigation due to their very interesting physical and chemical properties. For example, carbon nanotubes have been used as AFM tip to obtain atomic-resolution imaging of biological molecules such as DNA and proteins¹⁴. Carbon nanotubes can be used to fabricate nanomotors, which could enter inside cells to treat diseases^{41, 15}. For example, DNA and protein molecules can be immobilized on the surface of carbon nanotubes^{17, 42}. Carbon nanotubes can be filled with target DNA molecules or peptides, which could have a high potential in delivering target DNA molecules or peptides into special tissue region to treat the diseases^{43, 44}. There is a broad of interest to explore methods to enhance the efficiency of the PCR reaction. Here, we employ SWCNTs as a factor to investigate the influence of PCR efficiency. In this chapter, we describe the parameters influencing the yield of polymerase chain reaction (PCR), purification of SWCNTs and X-ray photoelectron spectroscopy (XPS). The potential mechanisms of interaction between SWCNT and PCR reaction components are discussed.

2.1.1 Parameters influencing the yield and specificity of PCR

The polymerase chain reaction was invented by Kary Mullis in 1985. This gene amplification technique can increase the number of copies of target genes by a magnification of several millions⁴⁵. Typically, the PCR reaction consists of a three-step recycling process: denaturation, annealing and extension. The reaction components include 10 × PCR buffer, deoxynucleotide triphosphate (dNTP) mixture, Mg^{2+} , DNA templates and Taq enzyme⁴⁶.

DNA polymerase

Many thermostable DNA polymerases are now commercially available, each are with different characteristics of thermal stability, exonuclease activity, processivity, fidelity, and reverse transcriptase activity. The Taq DNA polymerase, with its heat stability, high optimal temperature, and broad pH tolerance, is the most widely used thermostable DNA polymerase. The recommended concentration range for Taq DNA polymerase is between 1 and 2.5 units per 100 μl reactions.

PCR Buffer

Each thermostable polymerase has unique buffer requirements for optimal activity, most requiring Tris-Cl between 10 mM and 50 mM at pH 8.3–9.0. A stabilizing protein such as BSA or gelatin, and a non-ionic detergent such as Tween 20, NP-40, or Triton X-100, is also usually required. Concentrated reaction buffers are normally provided by the supplier of the enzyme, but for certain applications other additives such as formamide or glycerol may be essential for an efficient reaction.

Concentration of Magnesium

Magnesium concentration has a significant effect on the efficiency and specificity of the PCR reaction. In addition to its direct influence on enzyme activity and fidelity, magnesium also affects the T_m of the various hybrids that form during cycling, including primer-template, template-template, and primer-primer. For each new primer pair, it is generally worthwhile to titrate the magnesium concentration in 0.5-mM steps over the range of 0.5 mM to 5 mM (Fig. 2.1).

There are two common methods to optimize the PCR reaction conditions, selecting high-fidelity enzyme such as pfx DNA polymerase, and adding special chemical reagents such as glycerol. It is known that metal ions such as Mg^{2+} significantly increase the PCR efficiency by maintaining. A recommended $MgCl_2$ concentration in a standard PCR reaction is 1.5mM, at dNTP concentrations of around 200 μ M each.

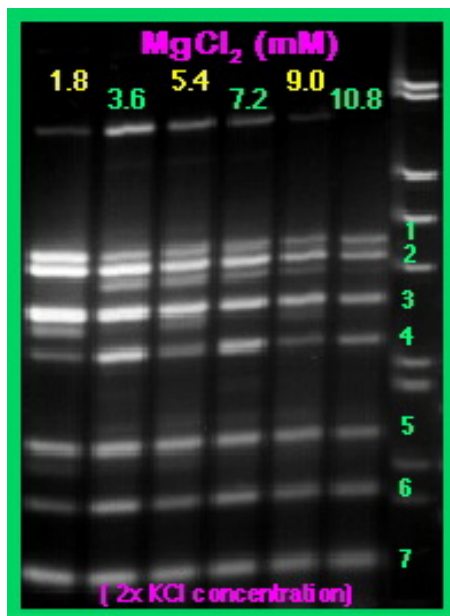


Figure 2.1: Multiplex PCR amplification with increasing magnesium concentrations. Overall reaction becomes more specific at 10.8 mM magnesium, but the products are reduced in intensity. The most optimal magnesium concentration is somewhere between 1.8 and 3.6 mM where the PCR product amount is higher. The unspecific product appears due to a lower than usual annealing temperature used for this reaction⁴⁷.

2.1.2 Purification of SWCNTs

Regarding CNT growth, catalyst particles play an important role in this process (Fig. 2.2). Metal catalyst is therefore considered as one of main impurities in the CNT products^{47,48}. We thought that it is necessary to use refined SWCNT. The following will describe the purification of CNT in literature.

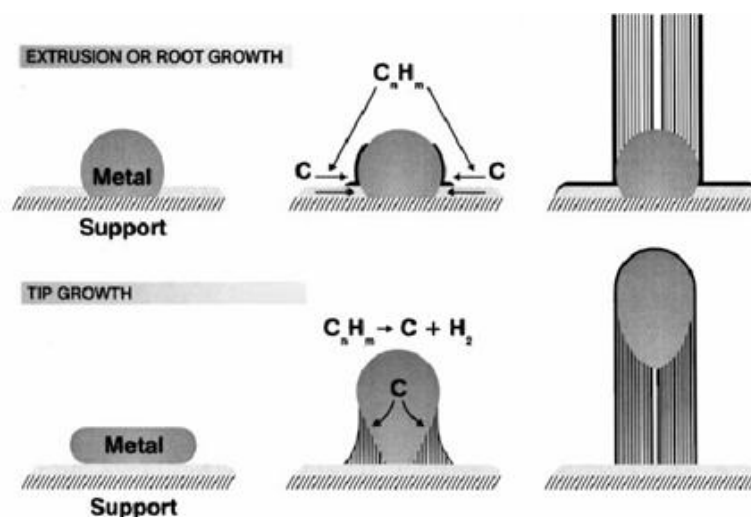


Figure 2.2: Visualisation of a possible carbon nanotube growth mechanism.

The as-produced SWNT soot contains a lot of impurities. The main impurities in the soot are graphite (wrapped up) sheets, amorphous carbon, metal catalyst and the smaller fullerenes. These impurities will interfere with most of the desired properties of the SWNTs. Also in the fundamental research, it is preferred to obtain SWNTs or the impurities, as pure as possible without changing them. The techniques such as oxidation, acid treatment, annealing, ultrasonication, micro filtration, ferromagnetic separation, cutting, functionalisation and chromatography have been studied.

Acid reflux

In general the acid treatment will remove the metal catalyst. First of all, the surface of the metal must be exposed by oxidation or sonication. The metal catalyst is then exposed to acid and solvated. The SWNTs remain in suspended form. When using a treatment in HNO_3 , the acid only has an effect on the metal catalyst. It has no effect on the SWNTs and other carbon particles¹². If a treatment in HCl is used, the acid has also a little effect on the SWNTs and other carbon particles. The mild acid treatment (4 M HCl reflux) is basically the same as the HNO_3 reflux.

Ultrasonication

In this technique particles are separated due to ultrasonic vibrations. Agglomerates of different nanoparticles will be forced to vibrate and will become more dispersed. The separation of the particles is highly dependable on the surfactant, solvent and reagent used. The solvent influences the stability of the dispersed tubes in the system. In poor solvents the SWNTs are more stable if they are still attached to the metal. But in some solvents, such as alcohols, mono-dispersed particles are relatively stable. When an acid is used, the purity of the SWNTs depends on the exposure time. When the tubes are exposed to the acid for a short time, only the metal solvates, but for a longer exposure time, the tubes will also be chemically cut^{49, 50}.

Micro filtration

Micro filtration is based on size or particle separation. SWNTs and a small amount of carbon nanoparticles are trapped in a filter. The other nanoparticles (catalyst metal, fullerenes and carbon nanoparticles) are passing through the filter. A special form of filtration is cross flow filtration. In cross flow filtration the membrane is a hollow fibre. The membrane is permeable to the solution. The filtrate is pumped down the bore of the fibre at some head pressure from a reservoir and the major fraction of the fast flowing solution which does not permeate out the sides of the fibre is fed back into the same reservoir to be cycled through the fibre repeatedly. A fast hydrodynamic flow down the fibre bore (cross flow) sweeps the membrane surface preventing the build-up of a filter cake^{51,52}.

2.1.3 XPS - X-ray photoelectron spectroscopy

X-ray photoelectron spectroscopy (XPS) was developed in the mid 1960s by K. Siegbahn and his research group. K. Siegbahn was awarded the Nobel Prize for Physics in 1981 for his work in XPS. The phenomenon is based on the photoelectric effect outlined by Einstein in 1905 where the concept of the photon was used to describe the ejection of electrons from a surface when photons impinge upon it. The energy of the photoelectrons leaving the sample is determined using a CHA and this gives a spectrum with a series of photoelectron peaks. The binding energy of the peaks is characteristic of each element. The peak areas can be used (with appropriate sensitivity factors) to determine the composition of the materials surface. The shape of each peak and the binding energy can be slightly altered by the chemical state of the emitting atom. Hence XPS can provide chemical bonding information as well XPS is a powerful technique widely used for the surface analysis of materials. At low energy resolution it provides

qualitative and quantitative information on the elements present. At high energy resolution it gives information on the chemical state and bonding of those elements. Further chemical information is available from the XPS valence band.

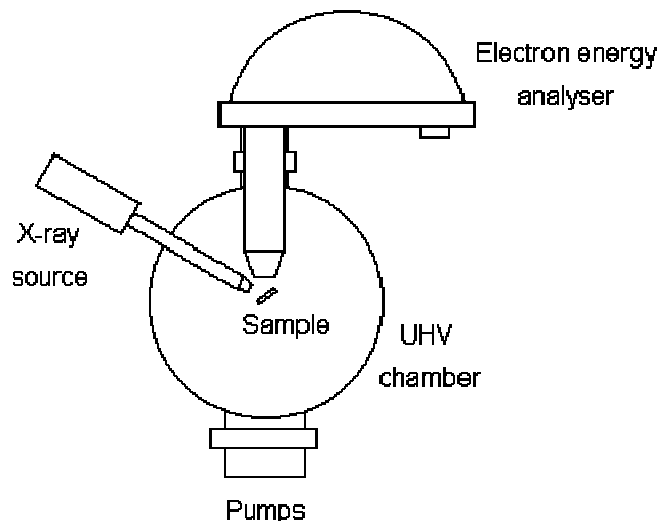


Figure 2.3: an X-ray photoelectron spectroscopy system is illustrated

2.2 Materials and methods

SWCNTs with a diameter of 2 nm were purchased from Carbon Nanotechnologies Inc. In order to move away metal catalyst, a mild acid treatment was carried out by refluxing materials in 4M HCl for 19h. The SWCNTs were then washed with ion-free water, filtered and dried at room temperature.

2.2.1 XPS analysis

In order to test purification of SWCNTs, SWCNTs and refined SWCNTs were analysed under XPS. SWCNTs in PCR reaction products were collected, dried and analysed by x-ray photoelectron spectroscopy (XPS). The XPS spectra were recorded with a VG ThetaProb instrument. Monochromatic Al $K\alpha$ ($h\nu = 1486.6$ eV) radiation is used to generate photoelectrons. The x-ray beam was focused to give a 400 μm spot size on the samples.

2.2.2 PCR preparation

Agene vector with BRCAA1(breast cancer associated antigen 1 gene, AF208045) was dissolved in ion-free water with a final concentration of 0.1 $\mu\text{g}/\mu\text{l}$. PCR primers synthesized by MWG Inc. were diluted to 10 pmol/ μl . The primer quality is at least 90%. Primers are stored in

a stock solution of 150 μM and used in a working dilution of 1:10 in RNase free water. The annealing temperature of the primer is calculated according to the formula:

$$[69.3 + 0.41 \times (\% \text{ GC-portion}) - 600 / \text{length of the primer}] - 5$$

The PCR primers are as follows:

The upstream primer sequence is 5-CGC TTA ATT AAA CAT ATG ACC AGA GTG AAA GAT GCT CAG-3 and the downstream primer sequence 5-TTA GTTAGT TAC CGGATC CCT TAA CTCCATTTGTAACCTTTGG-3. The target gene fragment is 410 bp. The PCR reaction buffer and Taq enzyme were purchased from Eppendorf Inc. Other chemical reagents were purchased from Sigma Inc.

In order to ensure the repeatability and specificity of the PCR reaction, we performed a series of reactions to establish the optimum reaction conditions. The PCR product in each reaction tube was quantified with SmartSpec™ 3000 spectroscopy (Bio-Rad Inc.). Seventeen tubes with gradually increasing amounts of SWCNTs underwent PCR reaction in an Icyler™ thermal cycler (Bio-Rad Inc.) containing 3 μl 10 \times PCR buffer, 3 μl 2.5 mM dNTPs, 3 μl 1.5 mM MgCl_2 , vector template 2 μl , 1 μl Taq enzyme (1.5 U) and 16 μl of a mixture of ion-free water and SWCNTs. Tube 1 with 16 μl ion-free water was used as control. 1 μl 10mg/ml SWCNTs corresponding to the SWCNT concentration of 0.33 μg μl in the reaction liquid, was added to tube 2. From tubes 3 to 17, different amounts of SWCNTs were added as follows: 0.66, 0.99, 1.32, 1.65, 1.98, 2.31, 2.64, 2.97, 3.3, 3.63, 3.96, 4.29, 4.62, 4.95, and 5.28 $\mu\text{g}/\mu\text{l}$. The experiments were repeated four times.

The same experiments were conducted in the absence of Mg^{2+} . Seventeen tubes with gradually increasing amounts of SWCNTs underwent PCR reaction in an Icyler™ thermal cycler (Bio-Rad Inc.) containing 3 μl 10 \times PCR buffer, 3 μl 2.5 mM dNTPs, 2 μl vector template, 1 μl Taq (1.5 U), and 21 μl of a mixture of ion-free water and SWCNTs. Tube 1 with 21 μl ion-free water was used as a control. 1 μl SWCNTs (10mg/ml) was added to tube 2. From tubes 3 to 17, SWCNTs were added into the reaction liquids with gradually increasing amounts as listed above. After the reactions were finished, for each PCR amplified transcript, 10 μl PCR products are mixed with 5 μl of loading dye and inserted into slots of a 1.2% agarose gel. The running buffer is 5 ml 50xeicosapentaenoic acid (TAE) diluted with 245 ml ultra pure water. The gel is initially run at 90 volts for 5 min until the samples have left the wells, then it is increased to 125 volts and run until the bromothiol blue band are 10 mm shorter of the gel end. The gel is then examined and photographed on an UV light box. The results were analysed with BioRad Gel Doc 2000 system.

2.2.3 Pt-labelled DNA fragment preparation and observation

In order to investigate interaction between SWCNTs and PCR, the PCR reaction products containing SWCNTs, DNA templates and Taq enzyme were analysed by SEM and HRTEM. The gel containing the SWCNTs and the DNA fragments were characterized under UV and white light condition. The gel sample was then excised with a clean sharp scalpel. The gel slices were weighed in colorless tubes and purified based on the process according to the MinEluteTM Handbook. Finally, the SWCNTs adhered to the membrane were extracted in an acetone solution. 400bp DNA fragments labelled with Pt nanoparticles were prepared as follows: 1 μ l 100 μ g/ml DNA products was added to 65 μ l of 1mM solution of K₂PtCl₄, mixed and then incubated at room temperature for 20h. Next, 1 μ l solution of 10mM DMAB (Borane Dimethylamine Complex) was added to the mixture which was kept at 27 ° C for 18h. The DNA-SWCNT hybrids were coated over holey carbon sample grids and dried at room temperature for 24 hours. The samples were then characterized using a Philips CM 200 TEM at 200 KeV.

2.3 Results

Purification of SWCNTs

There is no iron content in the SWCNTs after purification (Figure 2.4).

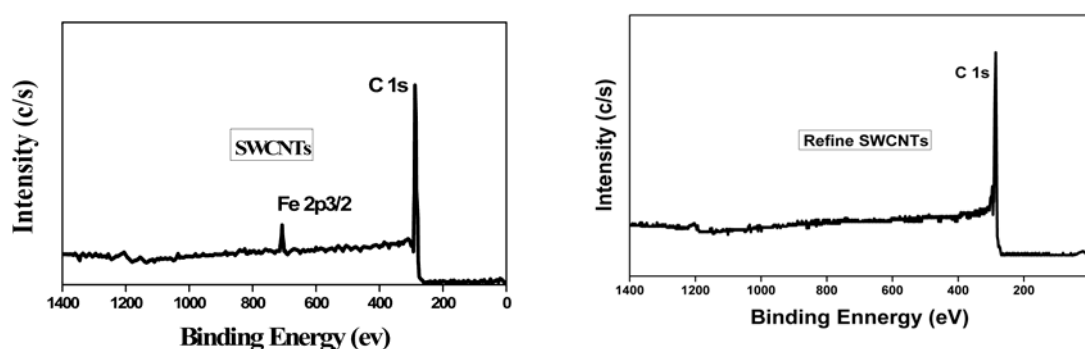


Figure 2.4: The result of binding energy intensity of samples and after purification reaction. The peaks C 1s and Fe 2p_{3/2} represent the binding energy intensity of SWCNTs before purification. The peak C1s represents the binding energy intensity of SWCNTs after purification.

The optimal PCR reaction condition is established in the absence of SWCNTs. The result in Figure 2.5 shows that the selected condition had good repeatability and specificity. The optimized PCR reaction conditions were as follows: 3 μ l 10 \times PCR buffer, 3 μ l 2.5 mM dNTPs, 3 μ l 1.5 mM MgCl₂, 1 μ l upstream and downstream primer each, 2 μ l DNA templates, 16 μ l ion free water, 1 μ l Taq enzyme. The reaction course consists of pre denaturation at 94 °C for 4

min, denaturation at 94 °C for 35 s, annealing at 55 °C for 42 s, extension at 72 °C for 55 s, 25 cycles, and final extension at 72 °C for 10 min.

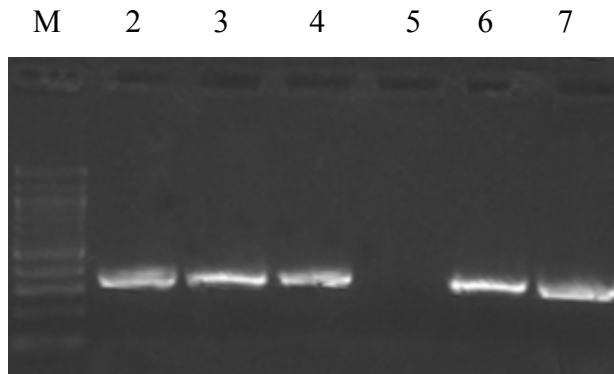


Figure 2.5: Electrophoresis results for PCR products under the optimal conditions. Lane 1 is the molecular marker; lanes 2–4 and lanes 6–7 are PCR products of repeated experiments; lane 5 is the negative control.

The electrophoresis result for PCR experiments with Magnesium ions under optimal reaction conditions is shown in Figure 2.6 and the quantitative product analysis in Figure 2.7. These results demonstrated that adding SWCNTs into the reaction liquid changes the efficiency of the PCR reaction. The amount of PCR products increases with the concentration of SWCNTs up to 3.0 $\mu\text{g}/\mu\text{l}$, and decreases at higher concentrations of SWCNTs.

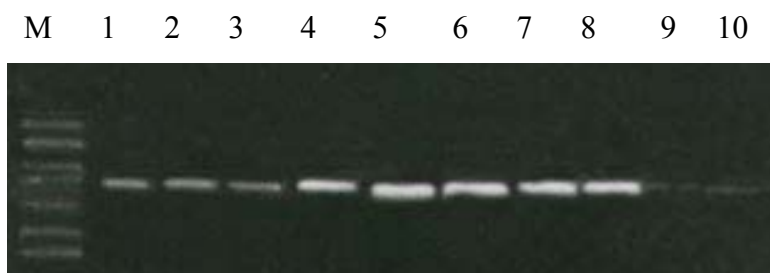


Figure 2.6: Electrophoresis of PCR products of 410 bp in the presence of Mg^{2+} and increasing amounts of SWCNTs. M is the molecular marker. Lanes 1 to 10 are PCR products with 0.33, 0.66, 0.99, 1.32, 1.65, 1.98, 2.31, 2.64, 2.97 and 3.3 $\mu\text{g}/\mu\text{l}$ SWCNTs in reaction liquid, respectively.

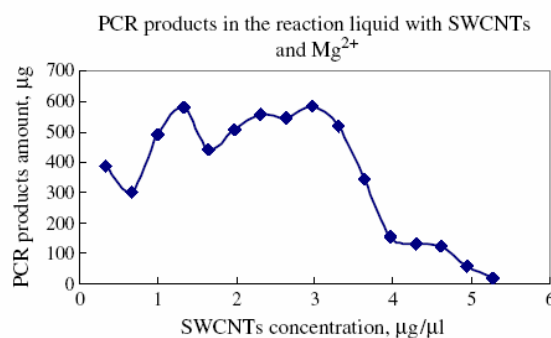


Figure 2.7: The productivity of the PCR reaction in the presence of Mg^{2+} as a function of additive SWCNT concentration. Each data point in the plot was the mean value of four experimental measurements. The PCR productivity exhibits a maximum at an SWCNT concentration of 3.0 $\mu\text{g}/\mu\text{l}$.

The Magnesium ion plays an important role in maintaining the activity of Taq enzyme. There is classic method to test the influence of $MgCl_2$. A multiplex PCR with mixture C was performed, keeping dNTP concentration at $200\mu M$ each and gradually increasing $MgCl_2$ from 1.8 to 10.8 mM. The overall amplification became gradually more "specific" and the products acquired comparable intensities (at 10.8mM). Higher concentrations of $MgCl_2$ appeared to inhibit the polymerase activity, decreasing the amount of all products. Taking into consideration the amount of PCR products, the best magnesium concentration should be between 1.8 and 3.6 mM. In our experiment, adding SWCNTs into the reaction liquid was observed to produce similar effects on the PCR reaction as addition of Mg^{2+} . The PCR productivity increases up to the critical SWCNT concentration of $3\mu g/\mu l$ (Fig. 2.8 and Fig. 2.9). After that, the amount of PCR product starts to decrease, as shown in figure 2.7. It is known that Magnesium ions act as receptors of electrons in the course of the Taq-directed DNA synthesis reaction^{8,9}. This observation suggested that SWCNTs could play a similar role to Magnesium ions in the PCR reaction, to help maintain the activity of Taq enzyme.



Figure 2.8: Electrophoresis of PCR products of 410 bp in the absence of Magnesium ions with increasing amounts of SWCNTs. Lanes 1–10 are the PCR products with 0.33, 0.66, 0.99, 1.32, 1.65, 1.98, 2.31, 2.64, 2.97 and $3.3\mu g/\mu l$ SWCNTs in the reaction liquid, respectively. M is the molecular marker.

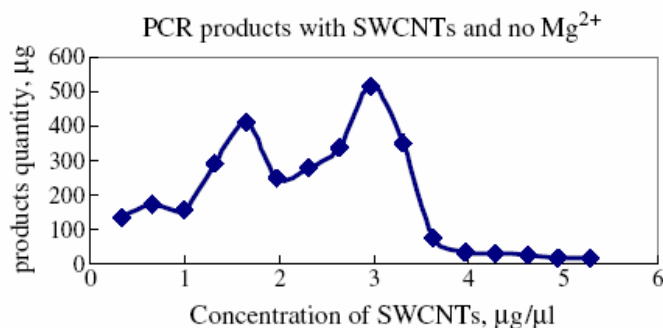


Figure 2.9: The productivity of the PCR reaction in the absence of Magnesium ions as a function of SWCNT concentration. Each data point in the plot was the mean value of four experimental measurements. The PCR productivity exhibits a maximum at an SWCNT concentration of $3.0\mu g/\mu l$.

In order to explore the potential mechanisms of interaction between SWCNTs and PCR reaction products, we examined samples including SWCNTs, and PCR reaction products with SWCNTs by SEM and HRTEM. A is an HRTEM picture showing SWCNTs. B is showing that PCR products cluster attached to a SWNT in HRTEM image. Under the presence of the reductant DMAB (Borane Dimethylamine Complex), Pt nanoparticles around 2nm in diameter can bind with the G (Guanine) and C (Cytosine) bases of DNA molecules via covalent bonding⁵³, resulting in the formation of Pt-labelled double stranded DNA fragments that are 4-6 nm in diameter (Fig. 2.10). Figure 2.11 is an SEM picture showing that DNA templates are attached to and wrapped around the surface of SWCNTs.

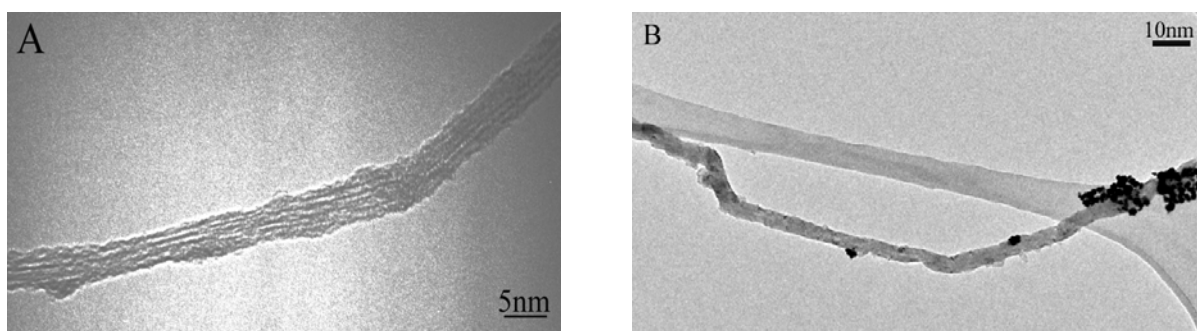


Figure 2.10: The HRTEM images of SWCNTs interacting with PCR reaction components. A is an HRTEM picture showing SWCNTs. B is an HRTEM picture showing that PCR products cluster attached to a SWNT bundle.

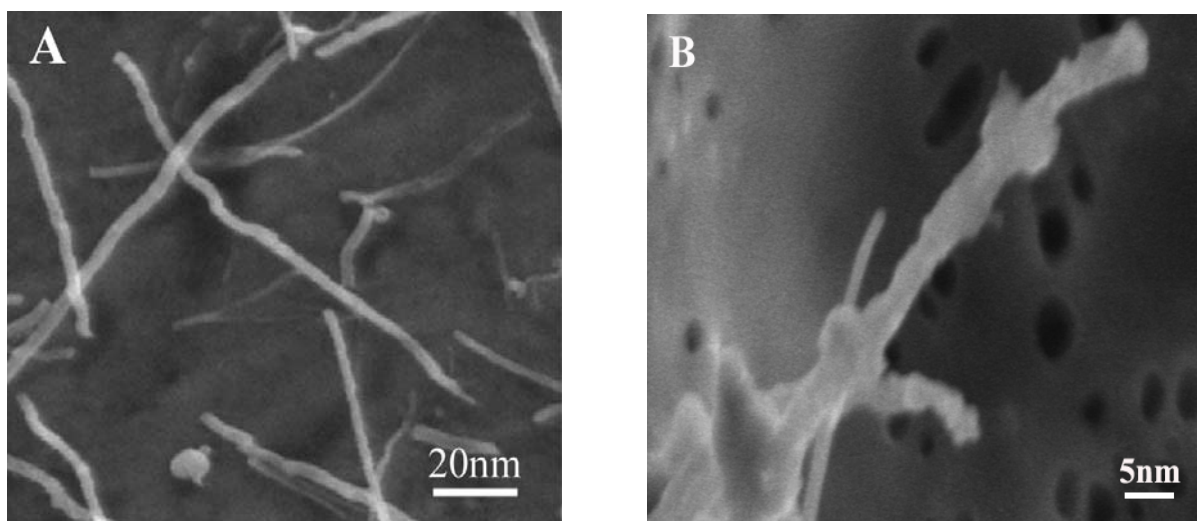


Figure 2.11: The SEM images of SWCNTs interacting with PCR reaction components. A is an SEM picture showing SWCNTs. B is an SEM picture showing that PCR products cluster attached to a SWNT bundle.

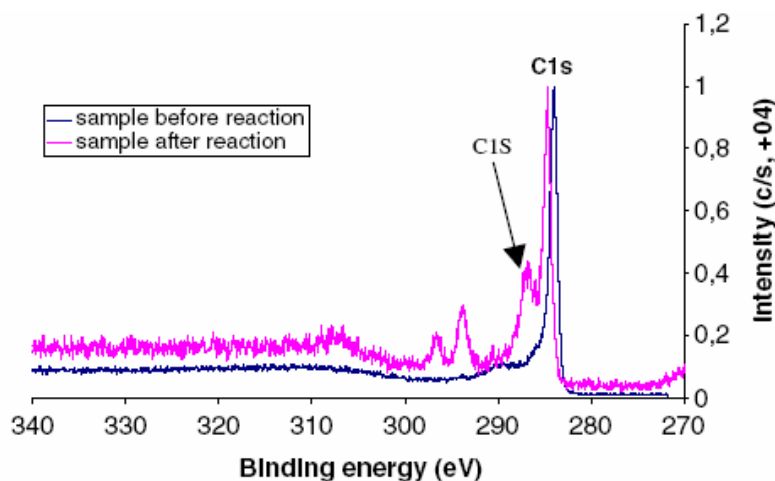


Figure 2.12: The result of C 1s binding energy intensity of samples before (lower curve) and after (upper curve) PCR reaction. The left peaks represent the binding energy intensity of C 1s of SWCNTs after PCR reaction; the right-most peak represents the binding energy intensity of C 1s of SWCNTs before reaction. The graph shows that the C 1s peak of SWCNTs moves towards the left with the emergence of two C 1s peaks, indicating enhanced binding energy after PCR reaction.

We also examined the change of binding energy before and after PCR reaction by XPS. The result is shown in figure 2.12. The XPS result showed that the C 1s binding energy intensity of PCR products increased after the reaction. A new C 1s peak appeared to the left of the main peak. The peak width increased and the binding energy spectrum moved towards the left compared with the corresponding results before reaction. These observations confirmed that strong interactions among SWCNTs, DNA templates and Taq enzyme took place during the course of the PCR reaction. These interactions affect the PCR reaction efficiency and the amount of PCR products.

To understand the mechanism of how SWCNTs may affect the PCR reaction, we examined some details of chemical reaction at three temperature levels. During the first stage of reaction, the reaction liquid is kept at 94 °C, the thermodynamic entropy in the reaction liquid increases, the hydrogen bonds between two strands are broken, and double stranded DNAs are denatured into two DNA single strands. As entropy increases, the Brownian motion of DNA molecules, primers and Taq enzymes speeds up with increasing kinetic energy, distributing them more evenly in the reaction liquids. When the reaction liquid is cooled to 55 °C, PCR primers bind to single-strand DNA templates, Taq enzyme takes effect, and complementary DNA strands begin to be synthesized. The reaction liquid is raised to 72 °C to complete the synthesis of new DNA double strands.

Addition of SWCNTs into the PCR reaction liquid could significantly change the distribution of reaction components. Due to the van der Waals interaction, the reaction components (DNA templates, PCR primers and Taq enzymes) are attracted towards SWCNTs.

The aggregation of reaction components around SWCNTs raises the probability of dynamical contact among these components^{54,55}, hence enhancing the efficiency of the PCR reaction and increasing the amount of PCR products. However, this kind of dose–product effect has an optimum SWCNT concentration. Higher SWCNT concentrations ($>3 \mu\text{g}/\mu\text{l}$) in the reaction liquid may damage the reaction environment of the DNA template, PCR primers and Taq enzyme via excessive binding of these components, decrease the probability of dynamical contact among the reactants, and reduce the reaction efficiency. As shown in figures 2.6 and 2.8, the PCR products rapidly decrease and become more difficult to observe with agarose gel electrophoresis when the concentration of SWCNTs in the reaction liquid is larger than $3 \mu\text{g}/\mu\text{l}$. The XPS result of figure 2.12 suggests that electronic transfer may have occurred between SWCNTs and PCR reaction components. In the PCR reaction, Taq enzyme directed the DNA polymerization reaction and resulted in synthesis of new DNA strands. In this reaction, Mg^{2+} acts as an electronic receptor and assisting factor for Taq enzyme. Our experiment showed that SWCNTs in the special concentration range may improve PCR reaction without Magnesium ions. The XPS result showed that the C 1s binding energy intensity of SWCNTs increased after reaction, suggesting that SWCNTs may act in a similar way to Magnesium ions in maintaining the high activity of Taq enzyme. SWCNTs appear to have potential as special catalysts in biochemical reactions.

Conclusion

SWCNTs added into PCR reaction liquids could significantly affect PCR reaction efficiency. A small amount ($<3 \mu\text{g} / \mu\text{l}$) of carbon nanotubes improves the efficiency of the PCR reaction, whereas a larger dose of carbon nanotubes tends to suppress the reaction. The possible mechanism for such behaviour could be the aggregation of reaction components caused by the van der Waals attraction. Similar effects of carbon nanotubes have been observed with or without Magnesium ions. Carbon nanotubes may play a similar role to Magnesium ions in serving as electron donors/receptors and could be explored as catalysts in biochemical reactions.

Chapter 3

Cytotoxicity of Single wall carbon nanotubes on human fibroblasts

3.1 Introduction

Along this development, the toxicity of single wall carbon nanotube (SWCNT) has become a public concern. As for other studies on animal experiments, we expected a strong relationship between cytotoxicity and carbon particle's size on cells. We therefore performed a systematic study on human fibroblasts in which different size of refined CNT were considered, and results were compared to other carbon materials. We have studied cell survival on five kinds of carbon materials; in increasing order are i) SWCNT, ii) active carbon, iii) carbon black, iv) multiwall carbon nanotubes (MWCNT), and finally, v) carbon graphite. Interestingly, we found a strong size, time, and dose effect of carbon materials upon the cell survival.

The following sections of this chapter are introducing the association information between carbon nanotubes and human cells and environment. Finally, a biological mechanism that explains why smaller particles (e.g. SWCNT) are more toxic is presented.

3.1.1 Influence of carbon nanotubes and associated nanomaterials on human cells and environment.

Nanotubes are widely seen as having huge potential to bring benefits to many areas of research and application, and are attracting rapidly increasing investments from governments and from businesses in many parts of the world⁵⁶. At the same time, it is recognised that their application may raise new challenges in the safety, regulatory or ethical domains that will require social debate. Moreover, it has become a focus to investigate the influence of carbon nanotubes and associated nanomaterials or nanodevices on human cells and environment.

There exist only a few preliminary toxicology studies investigating the effects of fullerenes or nanotubes on pulmonary cells and/or tissues.

Animal experiments with carbon nanotubes

Carbon nanotubes and skin irritation

Huczko *et al.* tested fullerene soot containing carbon nanotubes on skin irritation and allergen risks. There are two methods to test skin irritation in this paper¹⁹. First, the patch tests were used for 40 volunteers over a period of 96 hours. In the second study, the modified Raise rabbit eye test was conducted, wherein one eye of a tested rabbit was instilled with a suspension of soot while the other eye was used as a control. The authors reported that the patch test showed negative results after testing for 96 hours, *i. e.* no eye irritation was observed for carbon nanotube-containing soot.

Effect of CNT on pulmonary

Three groups have studied in fields of effects of CNT on pulmones. At the end of the last century, Huczko *et al.* tested the influence of carbon nanotube solution on pulmonary function in guinea pigs. A group of 5 guinea pigs was intratracheally instilled with 25 mg of carbon nanotube-containing soot. A control group of 5 guinea pigs was instilled with saline solution. After 4 weeks following instillation exposure, the animals were tested noninvasively for pulmonary function parameters and sacrificed for bronchoalveolar lavage examination. (Note that this is not a standard protocol for evaluation and no justification for the experimental protocol was provided in the paper). The results of the lung function measurements and bronchoalveolar lavage studies showed no differences between the experimental and control groups. The authors concluded that the fullerene soot with a high content of carbon nanotubes did not induce measurable inflammation in the respiratory tract of guinea pigs²⁰.

Recently, Warheit and Lam published that CNT induce formation of granulomas^{22, 21}. These results are consistent with the earlier speculation that tiny and stable nanotubes could accumulate in the body and damage tissue through the respiratory tract. Lam *et al.* investigated the pulmonary toxicity of three nanotube (NT) products in mice, using intratracheal instillation as the method of exposure. The three nanotube materials were manufactured by different methods and contained different metal catalysts. Metal analysis showed that the HIPCO-prepared nanotubes contained 27% (w/w) iron in the raw form, and 2% iron after purification

Carbolex electric-arc product contained 26% nickel and 5% yttrium. Groups of male B6C3F1 mice each were intratracheally instilled once with 0, 0.1, or 0.5 mg of NT suspended and ultrasonicated in 50 µl of mouse serum. Mice were also exposed to carbon black and quartz particles, two standard reference dusts. Carbon black exposure produced minimal effects, and high-dose quartz produced moderate inflammation in the lung. The investigators reported that all of the NT products, regardless of the type or amount of metal, induced a dose-dependent formation of epithelioid granulomas in the centrilobular alveolar septa and, in some cases, interstitial inflammation in the animals of the 7-day per groups. Lam *et al.* concluded that, if single-wall nanotubes reach the lung, they can be more toxic than quartz. Warheit *et al.* also investigated following particle types: (1) SWCNT, (2) quartz particles (positive control), (3) carbonyl iron particles (negative control), (4) phosphate-buffered saline (PBS) + 1% Tween 80, or (5) graphite particles (lung tissue studies only). However, there is not dose dependent series of multifocal granulomas. However, the mechanism(s) of granuloma formation under SWCNT are unclear.

Carbon nanotube and cells

Mattson and his coworkers have investigated the growth pattern of neurons on multiwalled nanotubes²³. Recently, Pantarotto *et al.* reported the internalization of fluorescently labelled nanotubes into cells with no apparent toxicity effects observed, although without identifying the uptake mechanism¹⁵. Moreover, Dai and his co-workers found SWCNT and SWCNT-streptavidin conjugates into human promyelocytic leukaemia (HL60) cells and human T cells (Jurkat) via the endocytosis pathway¹⁸. However, some studies have revealed a positive association between exposure to SWCNT and cell death. Carbon nanotubes can inhibit the growth of embryonic rat-brain neuron cells. Shvedova *et al.* investigated the effect of SWCNT on basic cellular processes involved in the induction of adverse responses in targeted human keratinocytes²⁴. After 18 h of SWCNT exposure, oxidant generation and cellular toxicity (as indicated by the formation of free radicals, accumulation of peroxidative products, antioxidant depletion, and loss of cell viability) were detected. Exposure to SWCNT also resulted in ultrastructural and morphological changes in cultured human cells. These investigators concluded that dermal exposure to SWCNT can result in accelerated oxidative stress and toxicity in the skin of exposed workers.

Adelmann *et al.* studied the effects of fullerenes on alveolar macrophages *in vitro*²⁵. The fullerene material was incubated in cell culture for 4 and/or 20 h with either a human

macrophage cell line preparation or with bovine alveolar macrophages. After 4 and 20 h of incubation, the C₆₀ fullerenes produced decreases in viability of both macrophage cell types to about 60% of control values. In addition, three inflammatory cytokines, used as biomarkers of lung injury, were measured in the supernatant of the cell cultures following incubation with fullerenes. There were increased levels of tumor necrosis factor (TNF), interleukin-6 (IL-6), and interleukin-8 (IL-8) in the supernatant of macrophage cell cultures exposed to fullerenes when compared to control macrophage cell cultures. The investigators concluded that the fullerene preparation used in their experiments was toxic to alveolar macrophages. They claimed that the reactions were similar to those they had experienced with quartz (crystalline silica) particles. Regarding CNT growth, catalyst particles play important role in this process. Metal catalyst is therefore considered as one of the main impurities in the CNT products. In Shvedova's experiments, unrefined CNT were used for test cytotoxicity. It is known, for instance, that nickel and its compounds may influence cells⁵⁶. We thought that a necessary step to confirm Shvedova's results is to use refined SWCNT. Since different geometries and particle surfaces may influence toxicity, three kind of nanotubes (NT), graphite, and quartz were studied by Lam et al. To make this study more complete, we explored the relationship between materials size and cell survival within five materials, which in increasing order are as follows i) SWCNT, ii) active carbon (AC), iii) carbon black(CB), iv) multiwall carbon nanotubes (MWCNT), and finally, v) carbon graphite(CG). TEM and SEM were used to observe the morphology of cells treated with the SWCNT. Following proteins were used in experiments: P-Cadherin, Fibronectin, focal adhesion kinase (FAK), Laminin, Cyclin D₃, and Collagen-IV.

3.1.2 Extracellular Signals

Cell adhesion to a substrate controls the behaviour of cells such as cell morphology, migration, growth, apoptosis and differentiation. Extracellular matrix (ECM) is the substrate for cell adhesion, growth, and differentiation, and it provides mechanical support to tissues⁵⁷. Local disruption of ECM results in selective programmed cell death within adjacent cells. Collagens are the most abundant protein found in animal, being the major protein comprising the ECM. There are at least 12 types of collagen. Type IV collagen is a major component of basal lamina. The collagen and FN, secreted by the fibroblasts, recruit and stimulate additional fibroblasts in wounds. The fibroblasts align themselves across the radial axis of the wound and link to each other as well as to the matrix through integrins and cell-cell junction⁵⁸.

Laminin, first isolated from the matrix of a mouse tumor, is a complex composed out of three distinct but related subunits present in basement membranes. The three subunits assemble

into a cruciform composed out of each other via disulphide bonds. The long arm of laminin molecule is formed by a coiled structure between the three subunits. At the end of this arm a globular domain is present, which is formed by the C-terminus of the A chain. Laminin has a variety of functions including the promotion of differentiation, neuritis extension and cell adhesion.

Cadherins play an important role in cell-cell junctions, transmitting signals to cells and inducing protein expression and cytoskeleton change⁵⁹. Cadherin usually link cells by homophilic mechanism, in which binding, molecular on one cell bind to the same kind of other molecular on other adjacent cells. For example, the cells neither express cadherins nor adhere to one another. Most cadherins function as transmembrane adhesion proteins that indirectly link the actin cytoskeleton of the cells. The highly conserved cytoplasm tail of these cadherins interacts indirectly with actin filaments by intracellular anchor protein named catenins (Fig. 3.1).

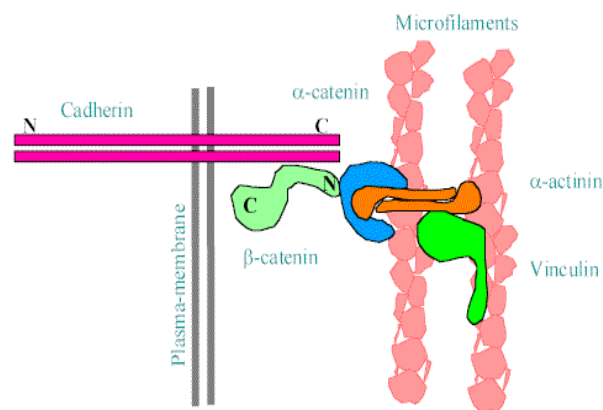


Figure 3.1: α -catenin in relation to the other major components of the cell-cell adherent junction. This is a simplified diagram showing the major interconnections.

An important element in the regulation of matrix adhesion reorganization is the fine tuning of local tyrosine phosphorylation. Phosphorylation or dephosphorylation events can regulate conformational states of molecules by modulating SH2-phosphotyrosine interactions. Focal adhesions contain protein tyrosine kinase of the src-family. Focal adhesions kinase (FAK) is known to localize to sites of cellular attachment at focal adhesions and has been associated with both cell motility and survival⁶⁰. FAK becomes activated upon cadherin and integrin on the cell membrane leads to autophosphorylation of focal adhesion kinase (FAK), creating binding sites at FAK for additional molecules in the signaling pathway⁶¹.

3.2 Materials and Methods

3.2.1 Type of particles

HR-TEM images of carbon materials (Figure 2.2): A) carbon graphite(CG), B) multiwall carbon nanotubes(MWCNT), C) carbon black(CB), D) active carbon (AC) and E) SWCNT.

Table 3.1 summarizes the five different carbon materials used in this research, along with their size and providers. The iron was removed from the particles by 4M hydrochloric acid. Materials were dispersed in water by sonication. Counting these particles is not an easy task, because of their size and material properties. Due to this fact, we opt to count them in an indirect way. The concentration of particles, that is solid weight over liquid volume, is easily calculated and can be used as a comparative index.

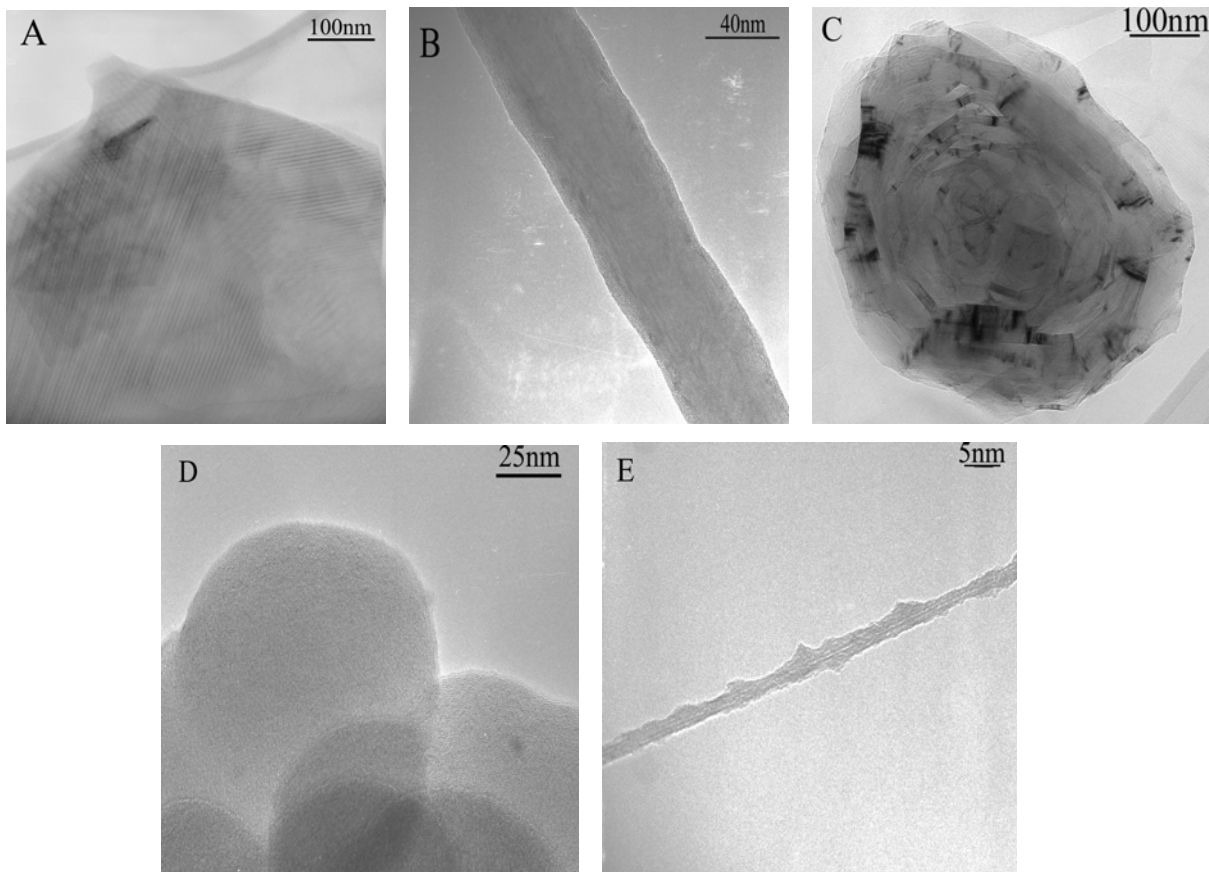


Figure 2.2: HR-TEM images of carbon materials: A) carbon graphite (CG), B) multiwall carbon nanotubes(MWCNT), C) carbon black(CB), D) active carbon (AC) and E) SWCNT.

Table 3.1: The five carbon materials that were used in our experiments.

Material	Size, and provider
CG	Diameters of up to 1 μ m plate. Kern group at the MPI-FKF, Stuttgart, Germany.
MWCNT	Diameter around 50nm, length more than 5 μ m. IIJIN CNT, Korea.
CB	Diameter more than 0.4 μ m. CarbonTech Aktivkohle GmbH, Essen, Germany.
AC	Up to 50nm in size. Silcarbon Aktivkohle GmbH, Kirchhundem, Germany
SWCNT	2nm wide, around 500nm length. Carbon Nanotechnologies Inc. USA.

3.2.2 Cell Culture

Human dermis fibroblasts were cultured in human fibroblasts medium (Cell-ling, Germany). Then, the cultured cells were incubated at 37 °C in a humidified 5% CO₂/95% air atmosphere.

3.2.3 Cell Survival Assay

The cells were seeded on 96-well plates (5x10³ cells/well); then cultured for 5 h and treated with SWCNT concentrations of 0.8, 1.61, 3.125, 6.25, 12.5, 25, 50, and 100 μ g/ml, for 1 to 5 days. The results from a SWCNT concentration of 25 μ g/ml were compared to those cells treated with CG, MWCNT, BC and AC, for 1 to 5 days, using the same concentration. The cells treated with SWCNT were washed in phosphate-buffered saline (PBS), and stained with 3-(4, 5-Dimethylthiazol-z-yl)-2, 5-dipheny-tetrazotium bromide (MTT). The survival rates of cells treated with different forms of carbon were normalised to be comparable with the control.

3.2.4 Transmission Electron Microscopy

Specimen preparation for TEM and observation

After an incubation of 48h, human fibroblasts with SWCNT, and normal control cells were harvested and washed with phosphate buffer (pH 7.4). Afterwards, the cells were washed by 0.01 M phosphate buffer (PBS), and fixed for 2h in 2.5% glutaraldehyde, which was previously dissolved in PBS (pH 7.4). The cells were incubated at 37 °C for 5 min. They were embedded into 0.1% agar. This agar was fixed by 2.5% glutaraldehyde in PBS at 4 °C for at least 2h. The samples were washed with PBS, and then fixed in 1% osmium tetroxide at 4 °C for 2h. Cells were dehydrated in graded series of ethanol and later embedded in epoxy resin, according to Pucillo ⁶².

Since the material must be exposed to a very high vacuum (10^{-5} to 10^{-8} Torr) when being examined, it must be dried at some stage in its preparation. The biological specimen must be stabilized (or fixed) so that its ultrastructure is as close as possible to that in the living material when exposed to the vacuum. The limited penetrating power of electrons requests that the specimens must be very thin or must be sliced into thin sections (50 - 100 nm) to allow electrons to pass through. Contrast in the TEM depends on the atomic number of the atoms in the specimen; the higher the atomic number, the more electrons are scattered and the greater the contrast. Biological molecules are composed of atoms of very low atomic number (carbon, hydrogen, nitrogen, phosphorus and sulphur). Thin sections of biological material are made visible by selective staining. The ultra thin vertical cross sections (50 nm) of cells were observed under a transmission electron microscope, Philips CM10. In addition, SWCNT were observed under HRTEM (Philips CM200).

3.2.5 Scanning Electron Microscopy

Cells were cultured and treated as described above. They were fixed with 2.5% glutaraldehyde in PBS at 4 °C for at least 2h. Subsequently, these samples were washed with PBS, fixed in 1% osmium tetroxide in phosphate buffer at 4 °C for 2h; and, dehydrated in graded series of ethanol. The cultures were analyzed with a Hitachi S-800 field emission scanning electron microscope.

3.2.6 Immunocytochemical Analysis

Samples were previously fixed with methanol for 20 min. They were washed with PBS, and permeated with 0.2% Triton X-100 for 5 min at room temperature; were then incubated with 1% normal bovine serum (Sigma) in PBS, for 1h. And, later, hybridized with the primary antibody: Rabbit IgG anti P-Cadherin (1:2000 dilution, Sigma), rabbit IgG anti FAK (1:2000 dilution, Sigma), mouse IgG anti F-actin (1:2000 dilution, Sigma). Further, samples were washed in PBS, incubated with sheep anti-rabbit-FITC antibody (1:160), and anti-mouse-Cy3 antibody (1:200); DNA was counterstained with 4', 6-diamidino-phenylindole [DAPI] (0.4 µg/ml). The cultures were mounted on N-propyl/gallate/glycerol, and examined under a fluorescent microscope (Leica, Germany). All reagents and antibodies were purchased from Sigma Chemical Co. (St. Louis, MO).

3.2.7 Western Blot Analysis

The cells were treated with a different nanotube concentration of 0.8, 1.61, 3.125, 6.25, 12.5, 25, 50 $\mu\text{g/ml}$, for 2 days. Cells were washed with PBS, and SWCNT were removed. Cells were scraped from the culture dish in PBS, pH 7.4, with 100 mM 6-aminohexanoic acid, 1 mM benzamidine-HCl, and 1% Triton X-100 at 4 °C. The total protein from each sample was analyzed by 7.5% sodium dodecyl sulfate-polyacrylamide gel electrophoresis (SDS-PAGE), accordingly to the procedure reported by Miyakoshi⁶³. In this study, 50 μg protein/sample was loaded in each lane. After PAGE, the polypeptides were transferred during 2h to nitrocellulose sheets (0.45 μm pore size; from Gibco-Invitrogen) by electrophoresis (140 mA) in a Tris-glycine buffer (25 mM Tris-HCl, pH 7.0; 19.2 mM glycine) containing 20% methanol. After an incubation time of 30 min in PBS containing 5% skimmed milk, the nitrocellulose sheets were washed five times in PBS containing 0.1% Tween-20 (PBS-T). Each one of the seven different sheets was incubated overnight with different antibodies at 4 °C: mouse anti-human Fibronectin antibody (1:20,000 dilution), mouse anti-human Laminin antibody (1:20,000 dilution), mouse anti-Cyclin D₃ antibody (1:5000 dilution), mouse anti-Collagen-IV antibody (1:5000 dilution), mouse anti- β -actin antibody (1:5000 dilution), rabbit anti-human P-Cadherin antibody (1:2000, dilution), and rabbit anti-human FAK antibody (1:4000 dilution). After extensively washing them in PBS-T, the nitrocellulose sheets were incubated for 1h with sheep anti-mouse IgG, and sheep anti-rabbit IgG (1:10,000 dilution). Immunodetection was performed using an epiluminescence (ECL) Western blotting protocol kit (Amersham Life Science, UK). The immuno-detected protein bands in ECL films were analyzed by means of densitometry.

3.2.8 Cell death Assay

Cells were treated with 25 $\mu\text{g/ml}$ of unrefined SWCNT, and refined SWCNT, for 18h. Dead cells were quantified by a Bio-rad Model 680 using Cellular DNA Fragmentation ELISA kit (Roche Diagnostics, Mannheim, Germany). Three replicate plates were used for each data point, and every experiment was performed at least three times.

3.2.9 Statistical Analysis

Differences between samples and the control were evaluated using the statistical analysis package SPSS 11, by means of one-way analysis of variance (ANOVA). Statistically significance was set to $p < 0.05$.

3.3 Results

3.3.1 Influences of the different materials on cell survival

As depicted in figure 3.2 A, the data shows that the survival rate of human fibroblasts was significantly reduced by SWCNT. The cell survival rates show to 79%, 50%, and 31% after a treatment with 100 $\mu\text{g/ml}$ SWCNT for 1, 3, and 5 days, respectively. Survival rates, shown in figure 3.2 B, correspond to the first 5 days of human fibroblasts treated with CG, MWCNT, CB, AC and SWCNT at a constant concentration of 25 $\mu\text{g/ml}$. Similarly, decreasing trends were observed in all carbon materials. As can be seen, the survival rate of cells treated with CG, MWCNT, CB, AC and SWCNT dropped to 84%, 78%, 71%, 65% and 58% at the end of the 5th day, respectively. These results strongly suggest a relationship between the size of carbon materials and the cell survival rate. The most pronounced effect is associated with SWCNT, which are the smallest particles tested.

There is strong size effect of carbon materials on cell survival. The effect of CG is relatively small in comparison with that of SWCNTs which are the smallest particles selected in the present study and show the most pronounced effect.

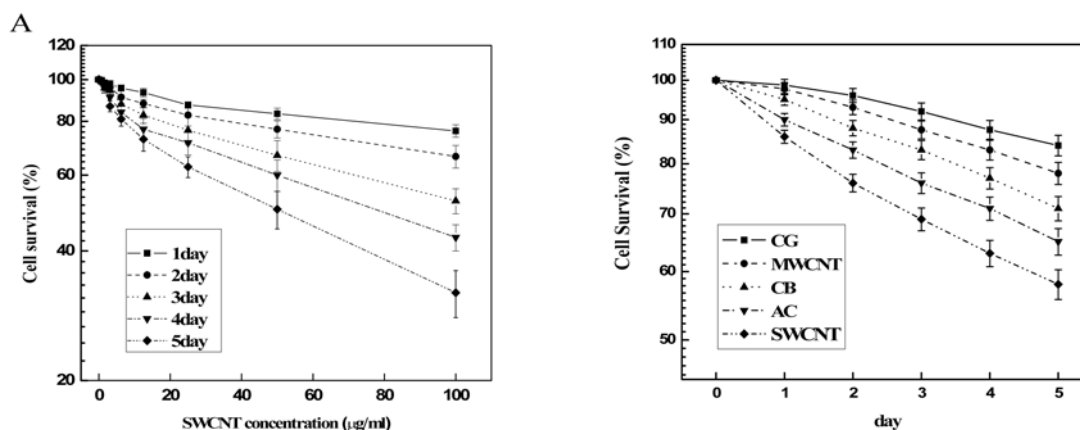


Figure 3.2: Effect of SWCNTs on survival rate of human fibroblast cells. (A) Cells treated with SWCNTs in concentrations of 0.8, 1.61, 3.125, 6.25, 12.5, 25, 50, 100 $\mu\text{g/ml}$ for 1 to 5 days. (B) Cells treated with 25 $\mu\text{g/ml}$ of carbon graphite (CG), multiwall carbon nanotubes (MWCNTs), carbon black (CB), active carbon (AC) and SWCNTs for 1 to 5 days. Three replicate plates were used for each data point and the experiments were performed at least three times. Error bars show the standard deviation.

3.3.2 Cell Death Assays

Three groups are shown: normal cells, cells treated with 25 $\mu\text{g/ml}$ of unrefined SWCNT, and refined SWCNT for 18h in figure 3.3. Cell that were treated with 25 $\mu\text{g/ml}$ of unrefined SWCNT, showed a slightly increase in the cell death rate, compared with normal cells. Nonetheless, there was a significant increase in the death rate when cells were treated with 25 $\mu\text{g/ml}$ of refined SWCNT (* $p < 0.05$).

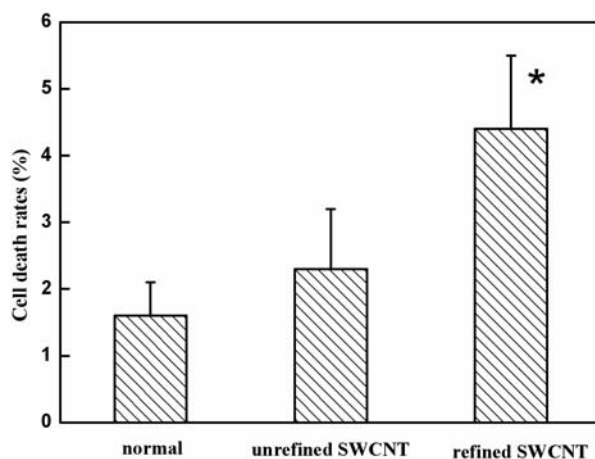


Figure 3.3: The effect of SWCNT on the cell death rate. Three groups are shown: normal cells, cells treated with 25 $\mu\text{g/ml}$ of unrefined SWCNT, and refined SWCNT for 18h. Three replicate plates were used for each data point, and every experiment was performed at least three times.

3.3.3 Effects of SWCNT on cell morphology

A scanning microscopy image (Fig. 3.4 A) shows a typical refined SWCNT used in our experiments. Dimensions are several nanometers in diameter and hundred nanometers in length, and have a rigid cylinder and needle-like shape. Cells treated with SWCNT were observed to attach a bundle of SWCNT on the right side (Fig. 3.4 B), while detaching from the substrate on the left side. Notice that some protuberances from the cell were not in contact with the substrate.

This figure shows that the membranes from normal cells did exhibit (Fig. 3.5 A) regular contours, and a distinct contrast against a moderately stained cytoplasm. In contrast, cells treated with SWCNT display ruffles on the cell membrane, and the cell shape appears to be somehow rounded in comparison with the normal cell. A bundle of SWCNT is seen to attach the cell at the upper left corner of figure 3.5 B.

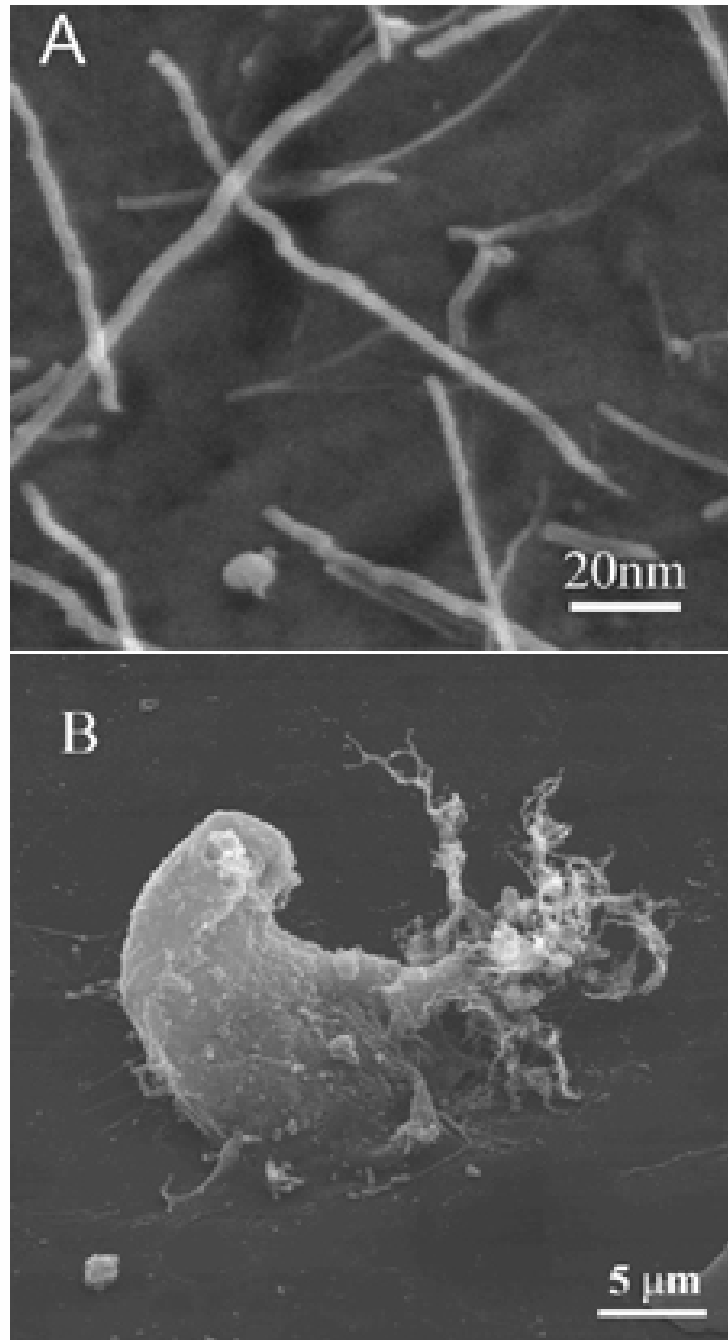


Figure 3.4: Effect of SWCNTs on spreading of human fibroblasts.

Scanning electron microscopy images of (A) SWCNTs, (B) a cell treated with SWCNTs.

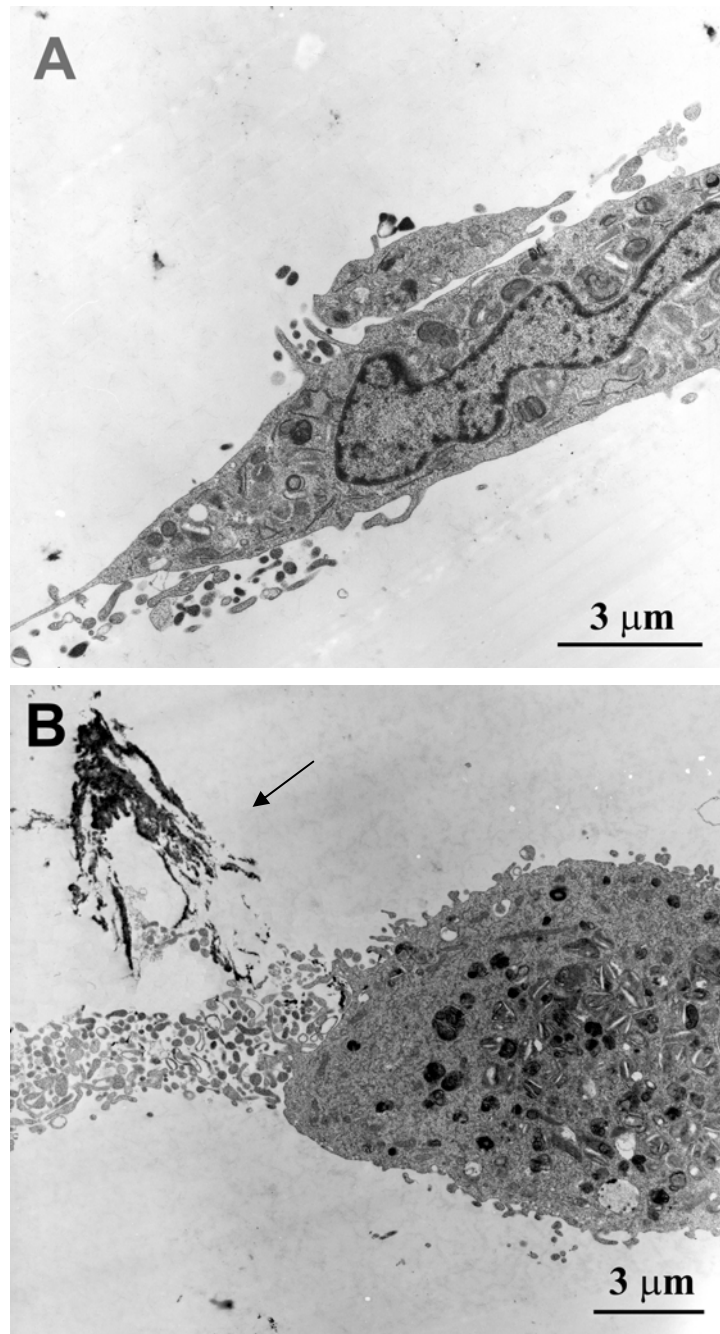


Figure 3.5: Effect of SWCNTs on morphology of human fibroblasts. Transmission electron microscopy images of (A) a normal cell, (B) a cell treated with SWCNTs. The arrow shows SWCNTs.

3.3.4 SWCNT effect on cell adhesion

3.3.4.1 Immunostaining assays

Normal cells appeared flat and spread out, and were visualised in a phase contrast microscope (Fig. 3.6A, Fig. 3.7A). P-Cadherin and FAK showed a rather homogeneous distribution (Fig. 3.6B, Fig. 3.7B). In SWCNT-treated cells (Fig. 3.6C and Fig. 3.7C), the nuclei were observed to move towards the regions where SWCNT were attached. As the membranes were reshaped, they approached the nuclei. In these cells, the adhesion-related proteins were seen to exhibit a

punctual distribution along the cell periphery (Fig. 3.6D, Fig. 3.7D). Normal fibroblasts did show an organized radial distribution of actin networks, which became random and irregular when treated with SWCNT.

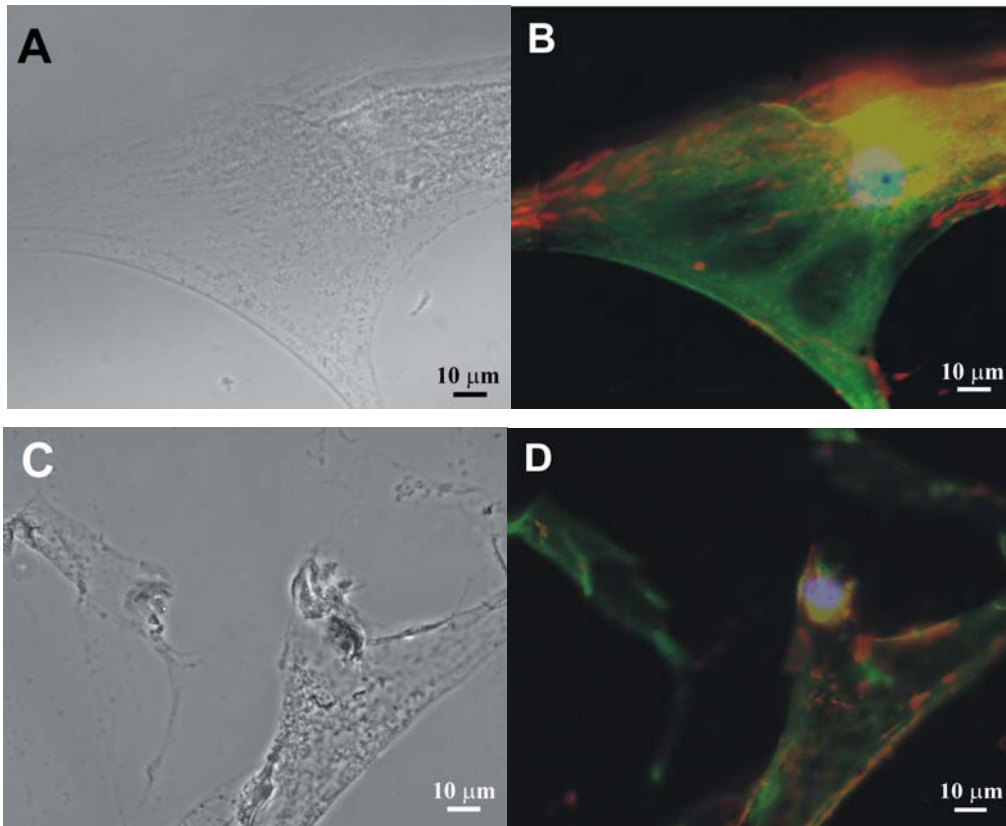


Figure 3.6: Effect of SWCNTs on distribution of fibronectin and P-cadherin protein. (A) Phase contrast microscopy of a normal cell; (B) Distributions of fibronectin (red), P-cadherin (green) and cell nucleus (blue) in a normal cell; (C) Phase contrast microscopy of a SWCNT-treated cell; (D) Distributions of fibronectin (red), P-cadherin (green) and cell nucleus (blue) in a SWCNT-treated cell.

Normal fibroblasts show an organized radial distribution of actin network (Fig. 3.7A) which becomes random and irregular when treated with SWCNTs (Fig. 3.7B).

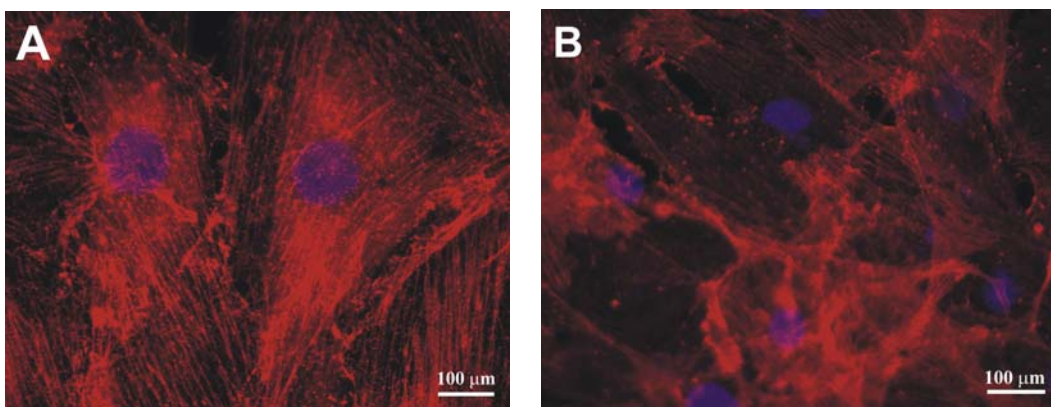


Figure 3.8: Effect of SWCNTs on F-actin distribution. (A) Distribution of F-actin (red) and cell nucleus (blue) in a normal cell; (B) Distribution of F-actin (red) and cell nucleus (blue) in a SWCNT-treated cell.

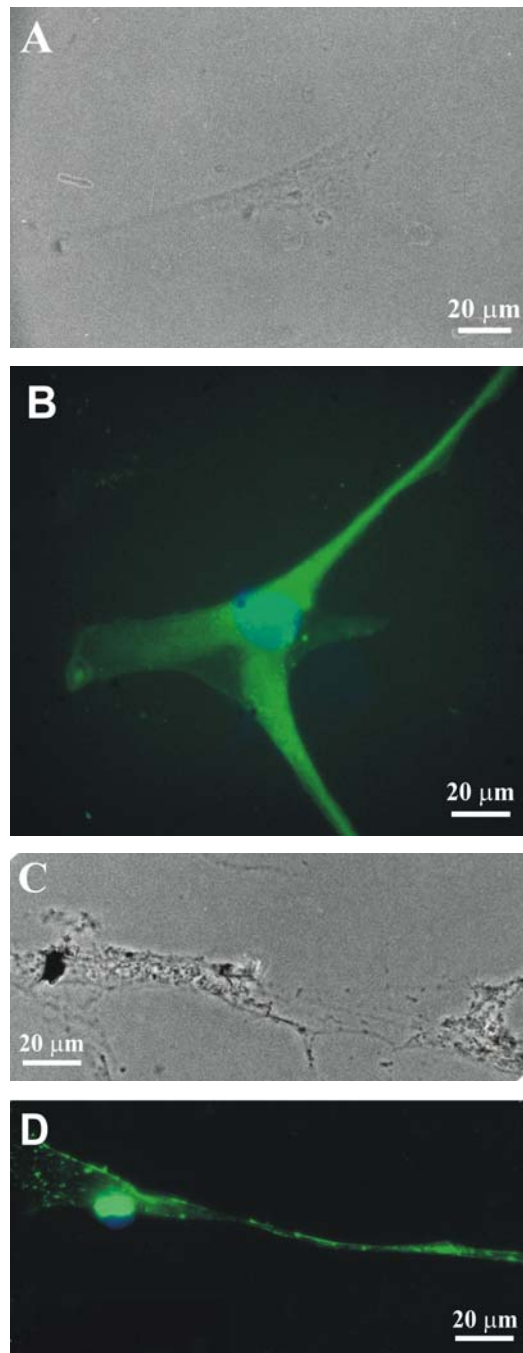


Figure 3.7: Effect of SWCNTs on distribution of FAK protein. (A) Phase contrast microscopy of a normal cell; (B) Distributions of FAK (green) and cell nucleus (blue) in a normal cell; (C) Phase contrast microscopy of a SWCNT-treated cell; (D) Distributions of FAK (green) and cell nucleus (blue) in a SWCNT-treated cell.

3.3.4.2 Western blot assays

There is a representative Western blot analysis of the effect of SWCNT upon different protein expression on the top of Figure 3.9. Western blot results of Fibronectin, Laminin, P-Cadherin, FAK, Collagen IV, and Cyclin D₃, exhibit down-regulated expression levels, while the concentration of SWCNT increases. The β -actin protein expression remained unchanged in each test.

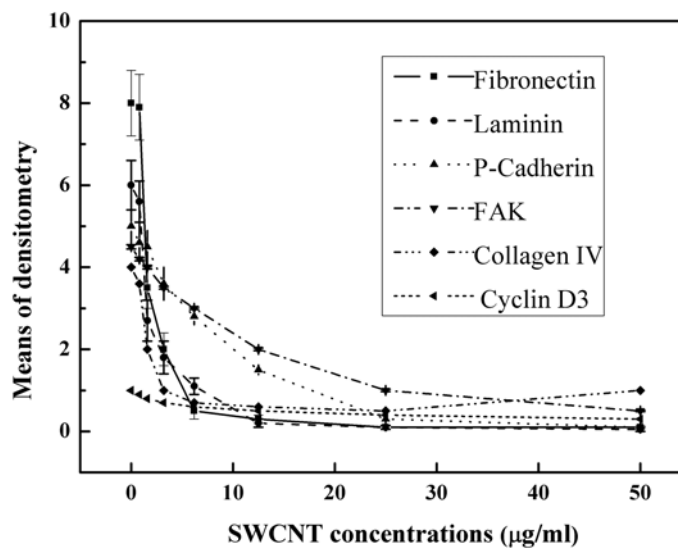
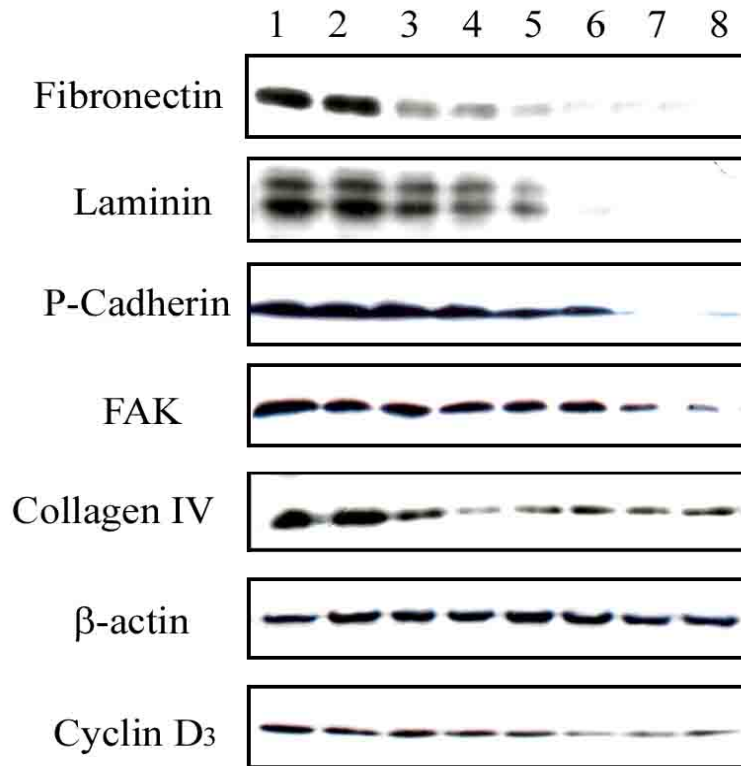


Figure 3.9: Western blot analysis of the effect of SWCNTs on the expressions of fibronectin, laminin, P-cadherin, FAK, collagen IV and cyclin D3. Lane1 to lane 8 are the protein expressions at SWCNT concentrations of 0, 0.8, 1.61, 3.125, 6.25, 12.5, 25, 50 $\mu\text{g/ml}$, respectively.

3.4 Discussion

The study done by Shvedova highlighted the cytotoxicity of SWCNT; and to the best of our knowledge, it is the first peer-reviewed comparative toxicological assessment of SWCNT. Nevertheless, the nanotube material was mentioned to contain 30% iron. It is known, for instance, that nickel and its compounds are also toxic. Thus, we avoid problem arising from catalytic by acid reflux removing metals in SWCNT.

In contrast to Shvedova *et al.*, we found that a substantially lower concentration of SWCNT, 25 $\mu\text{g/ml}$ instead of 0.06 mg/ml , does increase the cell death rate. This fact may be easily interpreted as follows. Unrefined SWCNT tend to create bundles; therefore, SWCNT bundle together, creating larger and less harmful particles. Some experimental results have shown that the toxicity is inversely proportional to particle sizes and surface areas²⁶. Recently, other author had predicted a strong relationship between toxicity and carbon particle's size on animal experiments⁶⁴. In this work, we have therefore investigated the cytotoxicity of nanotubes and compared it with the effects of carbon graphite, multiwall carbon nanotubes, carbon black and active carbon.

Our results show that, in comparison with other carbon materials under investigation, SWCNT is the most effective in inhibiting cell survival (Fig. 3.2 B). Since MWCNT is larger (thus not so harmful) than SWCNT, the effect of the former is relatively small. Our hypothesis may explain why solution of MWCNT did not induce corneal irritation or pulmonary damage rodents in Huczko's experiments¹⁹.

The underlying mechanism behind the cytotoxicity of SWCNT has been studied under different approaches. For instance, the cytotoxicity mechanism of the functional carbon materials was investigated²¹. The cytotoxicity of unrefined SWCNT has been studied by using ultra-structural alteration, cell detachment and F-actin distribution²³. Despite these works, some questions remain unclear. For example, why do SWCNT change the cytoskeleton and cell morphology? We studied cell adhesion to explore these phenomena. It is well know that certain proteins like FAK, Cadherin, Collagen, and Fibronectin play an important role in cell adhesion^{62, 63}. Because of their tiny size, hydrophobic SWCNT might insert ruffles in cell membranes. This response may disturb cell surface protein receptors.

In this work, we observed an accumulation of FAK around the cell nuclei after the cell was exposed to SWCNT, as depicted in figure 3.7D. There is, however, evidence that FAK is associated with a reduced cell survival and adhesion⁶⁵. We noticed that SWCNT can disturb the FAK distribution, and consequently, decrease cell adhesion. On the other hand, Cadherin is another important transmembrane protein that links the actin network to outside cells, the

extracellular matrix, and other cell⁶⁶. This protein rapidly responds to different cellular signals, and it is likely mediated through the cytoplasmic tail⁶⁷. As a feedback, the cytoskeleton mediates intracellular signals to deform intracellular organelles⁶¹. A decrease of Cadherin expression level does result in a dramatic reduction of Cadherin-mediated cell adhesion⁶⁸. Further, our results show that SWCNT can disturb the distribution of both P-Cadherin and F-actin (Fig. 3.6 D, Fig. 3.7 D), the last one in full agreement to Shvedova result. Thus, it influences the cell spreading and survival, ultimately leading to a change in cell structure. Interestingly, western blot results showed lower than normal cell expression of Laminin, Fibronectin, P-Cadherin, FAK, Collagen IV, and Cyclin D₃ in the cells treated with SWCNT (Fig. 3.9). Further evidence shows that the interactions between ECM proteins and Cyclin D₃ can regulate cell proliferation and adhesion⁶⁹. This result supports the above mentioned phenomenon.

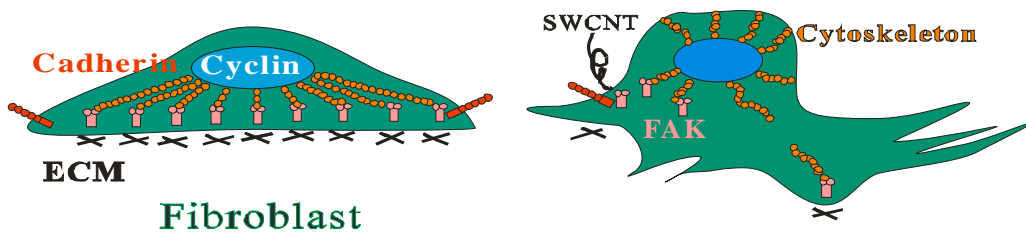


Figure 3.10: a possible mechanism of SWCNT on fibroblasts

In summary, a possible mechanism that describes the effect of SWCNT on fibroblasts is suggested in figure 3.10. Whilst the left side of figure 3.10 shows a normal symmetric cell, the right side of figure 3.10 shows how a membrane is deformed by a SWCNT. That is, the SWCNT might activate the ECM protein signal, and thus change the cytoskeleton. Afterwards, a displacement of internal organelles, and a deformation of the cell membrane takes place. Then, by a decrease of Fibronectin, Laminin, P-Cadherin, FAK, Cyclin-D₃, and Collagen IV expression levels, a notorious change in shape and adhesion is found. In short, SWCNT is seen to induce uneven distribution of Fibronectin, P-Cadherin, FAK, and actin in cells (Fig. 3.6 D, Fig. 3.7 D), and to decrease cell adhesion (Table 2) and spreading (Fig. 3.4 B, Fig. 3.5 B). Finally, this phenomenon does result in cell detachment, and thereupon induces cell death, as shown in figure 3.3. This reason can also explain why hippocampus cells did not form branches on the nanotube substrate²².

We should emphasize that our results may provide useful information on risk assessment. For example, cell survival is seen to decrease to about 79%, 50% and 31% after a treatment of 1 day, 3 days, and 5 days with SWCNT, respectively. Qualitatively, we may say that 25 $\mu\text{g}/\text{ml}$ of SWCNT does induce cell death. SouthWest NanoTechnologies Inc. does consider potential side effects of SWCNT when the concentration is greater than 15 mg/m^3 in total dust, or 5 mg/m in respirable fraction on mucus membranes, eyes, skin, inhalation, and respiratory tract. On the other hand, different concentration of SWCNT can induce granulomas²¹. A dosage of 4 mg/kg CNT in Warheit's rat work, and 0.5 $\text{mg}/30\text{g}$ HiPco nanotubes per mouse, shown in Lam's work, proved to induce granulomas. In the present study, the concentrations of SWCNT are far higher than the standard concentrations used for studies *in vivo*. It is worthwhile to remark here that 1 $\mu\text{g}/\text{ml}$ is the point where we started to observe cell changes, see figure 2 A.

In conclusion, after studying the toxicity of a range of carbon materials upon fibroblast cells, we found that SWCNT without iron can induce cytotoxicity. Among all five carbon materials, SWCNT are ranked as the most effective in inhibiting cell survival. Moreover, we notice that a lower concentration of SWCNT than reported in the literature does lead to cell death. Our findings may therefore provide guidance for future research and risk assessment of SWCNT exposure. We thus confirm that size in CNTs is a very important factor. Since nanotechnology is entering in a large-scale use, health and safety issues of SWCNT should be promptly addressed. We think that further cytotoxicity studies should be focused on finding dose thresholds on SWCNT of different size.

Chapter 4

Effect of single wall carbon nanotubes on human HEK293 cells

4.1 Introduction

Carbon nanotube, as a class of stiff, stable and hollow nanomaterials with many unique properties such as mechanical, physical and chemical properties, have been explored for application in biomedical engineering and medical chemistry⁷⁰. So far, it has become a focus to investigate the influence of carbon nanotubes and associated nanomaterials or nanodevices on human cells and environment. Carbon nanotubes can be functionalized to achieve improved properties and functions such as biocompatibility and biomolecular recognition capabilities.¹⁵ The potential with which carbon nanotubes can be applied in biomedical engineering and medicinal chemistry is highly dependent upon their biocompatibility. Carbon nanotubes exhibit cytotoxicity to human keratinocyte cells²⁴, can inhibit the growth of embryonic rat-brain neuron cells and induce the formation of mouse-lung granulomas^{21, 22}. However, so far few reports are closely associated with mechanism of nanotubes on human normal or tumour or embryonic tissue cells. Therefore, investigating effect of carbon nanotubes on human cells and their interaction mechanism is necessary. Cell adhesion, proliferation and apoptosis are important phenomena in the response of environment and activate intracellular functions. The following section of this chapter is providing background information on the apoptosis and Cell cycle progression. A description of the materials and methods will follow. Finally the interaction mechanisms between SWCNT and HEK293 cells are elucidated.

4.1.1 Apoptosis and Cell cycle progression



Figure 4.1: Apoptosis and Cell cycle progression

Apoptosis and Cell cycle progression play fundamental roles in normal tissue homeostasis during embryogenesis and through the entire lifetime of multicellular organisms (Fig. 4.1)^{71, 72}. There are many apoptosis related genes. Some genes such as p16, bax, hrk, bak1, p57, FGFR2, TGF beta receptor 1 and TNFAIP2 genes up-regulate in apoptosis. The cycle-associated genes such as cyclin D1, cdk2, cdk4 and cdk6 down-regulate in apoptosis. ECM proteins control cell adhesion and spreading which up-regulate the level of cyclin D protein⁷³.⁷⁴ The p16 is known to regulate the activity of cyclin-dependent kinases (cdks), the heart of the eukaryotic cell cycle engine. The up-regulation expression of p16 protein may bind to and inhibit the kinase activity of cdk2, cdk4 and cdk6, hence prevent the cells from entering into the S phase and subsequently arrest the cell cycle in the G1 phase. It has been documented that cdk4 and cdk6 are activated in association with D-type cyclin in the mid G1 phase. Cyclin D, a G1/S cyclin, promotes S phase by inhibiting Rb. A second G1/S cyclin, cyclin E, is a principal regulator of the S phase during cell development. Although cyclin E is an inhibitor of Rb, it has additional Rb/E2F-independent cell-cycle roles⁷⁵. Cdk2 is associated with cyclin E in the late G1 phase and its activity is rate-limiting for progression from the G1 to the S phase, regulating both the passage from G1 into S and the S phase progression. Cdk2 down-regulation expression may result in cell arrest in the G1 phase. Thus, reduced levels of these G1-associated cdks and cyclins may also facilitate blockade of the cell cycle in mid G1 and G1/S. The cells are unable to progress through G1 to S: instead of becoming quiescent and entering

G₀, they enter cell apoptosis. It is important to study these phenomena in the response of mammalian cells to physical and chemical factors.

The morphological observation, Western blot, flow cytometry, immunofluorescent analysis and biochip analysis are used to investigate cell adhesion, apoptosis and cell cycle under SWCNTs.

4.2 Materials and methods

4.2.1 Antibodies

Monoclonal anti-human fibronectin antibody (product no. F7387), anti-focal adhesion kinase (pp125FAK) antibody (product no. F2918), anti-pan cadherin antibody (product no. C3678), monoclonal anti-collagen type IV clone COL-94 (product no. 1926), monoclonal anti-laminin clone lam-89 (product no. L8271), anti-cyclin D3 antibody (product no. C7214), monoclonal anti-actin clone AC-15 (product no. A5441), anti-rabbit IgG FITC (product no. F9037) and anti-mouse IgG Cy3 conjugate antibody (product no. C2181) were purchased from Sigma Inc.

4.2.2 Cell viability and proliferation assay

HEK293 cells (human embryo kidney cells) were obtained from American ATCC Cell Line Center. The cells were cultured in essential medium with Eagle's salt supplemented with 10% fetal calf serum, 1% kanamycin and 2 mM glutamine (GIBCO-BRL Life Technologies, Gaithersburg, MD), at 37 °C in 5% CO₂ humidified incubator. The medium was exchanged every two days. MTT (tetrazolium salt) assay was applied to evaluate the effect of SWCNTs on HEK293 cells viability by measuring the uptake and reduction of tetrazolium salt to an insoluble formazan dye by cellular microsomal enzym⁷⁶. SWCNTs with different concentrations of 0.8 µg/ml, 1.6 µg/ml, 3.1 µg/ml, 6.25 µg/ml, 12.5 µg/ml, 25 µg/ml, 50 µg/ml, 100 µg/ml, 150 µg/ml and 200 µg/ml were added inside the 24-well plates. HEK293 cells without SWCNTs were used as the control. The cell viability was calculated by the follow formula: cell viability (%) = optical density (OD) of the treated cells/OD of the non-treated cells. The cell number was counted daily by using the Trypan blue dye exclusion method and the percentage of cell growth was calculated as a ratio of numbers of SWCNTs-treated cells and control cells treated with 0.5% DMSO vehicle.

4.2.3 Detection of adhesion ability

The cell attachment assay was performed as previously described in the literature⁷⁷. Essentially, 6-well plates were coated with fibrinogen (5 µg/ml) and vitronectin (1.5 µg/ml) in DPBS. Cells

were harvested, washed three times with serum-free minimal essential medium with Eagle's salt and resuspended in attachment solution (calcium- and magnesium free Hanks' balanced salt solution, 20mM HEPES, 1 mg/ml heat-inactivated BSA, 1 mM CaCl₂ and 1 mM MgCl₂). Cells (1×10^4) were added to each well and allowed to culture for 1–5 days at 37°C in a humidified 5% CO₂ incubator. These plates of respective 25 µg/ml, 50 µg/ml, 100 µg/ml, 150 µg/ml and 200 µg/ml SWCNTs-treated cells were cultured for 1–5 days and 1 control plate (1×10^4 cells were added to each well-treated with 0.5% DMSO vehicle and allowed to culture for 1–5 days at 37 °C in a humidified 5% CO₂ incubator) was centrifuged for 10 min at the speed of 4000 rpm. Unattached cells were washed with Hanks' balanced salt solution. The number of remaining attached cells after centrifugation was quantified spectrophotometrically at 405 nm in triplicate⁷⁸. Cell adhesion ability (%) = the number of SWCNTs-treated adhesive cells/the number of control adhesive cells.

4.2.4 Observation under Scanning Electron Microscopy

Cells were cultured and treated as described above. They were fixed with 2.5% glutaraldehyde in PBS at 4 °C for at least 2h. Subsequently, these samples were washed with PBS, fixed in 1% osmium tetroxide in phosphate buffer at 4 °C for 2h; and, dehydrated in graded series of ethanol. The cultures were analyzed with a Hitachi S-800 field emission scanning electron microscope.

4.2.5 DNA fragmentation

HEK293 cells were cultured with 25 µg/ml of or without SWCNT for 1–5 days, and resuspended in lysis buffer (50 mM Tris, pH 7.5, 10mM EDTA and 0.3% Triton X-100) for 30 min on ice. Cell lysates were treated with RNase (100 µg/ml) for 30 min at 55 °C and then with proteinase K (400 µg/ml) for another 1 h at 55 °C. The supernatant was extracted with phenol/chloroform. The DNA was precipitated and electrophoresed on 2% agarose gels.

4.2.6 Flow cytometry analysis

HEK293 cells were treated without or with 25 µg/ml of SWCNT for 1–5 days, and harvested at respective days. After washing with PBS, the cells were fixed in 70% ethanol/PBS for 30 min on ice. Approximately 4×10^5 cells were centrifuged. The cell pellets were resuspended with PBS, and further treated with RNase (DNase free, 100 µg/ml, and final concentration in PBS) and propidium iodide (40 µg/ml, final concentration in PBS) for 30 min at 37 °C. The treated cells were centrifuged. The cell pellets were resuspended with PBS. The cell suspension was

passed through a 19-gauge needle and kept on ice until analysis. The number of cells in different phases of the cell cycle was analyzed using a FACScan Flow cytometer with Cell-FIT software (Becton Dickinson Instruments).

4.2.7 SDS-PAGE analysis and Western blot analysis

HEK293 cells were treated with 25 $\mu\text{g}/\text{ml}$ of SWCNT for 1–5 days. After incubation, cells were lysed in protein lysis buffer (50mM Tris pH 7.4, 150mM NaCl, 1mM EDTA, 1mM EGTA, 5% 2-mercaptoethanol, 1% NP-40, 0.25% sodium deoxycholate, 5 $\mu\text{g}/\text{ml}$ leupeptin, 5 $\mu\text{g}/\text{ml}$ aprotinin, 10 $\mu\text{g}/\text{ml}$ soybean trypsin inhibitor and 0.2mM phenylmethyl sulfonylfluoride); protein concentrations were determined using the Bradford method. Equal amounts of sample lysate were separated by sodium dodecylsulfate polyacrylamide gel electrophoresis (SDS-PAGE) and electrophoretically transferred onto polyvinylidene di-fluoride (PVDF) membranes (Millipore). The membrane was blocked with 0.1% BSA in TBST buffer (20mM Tris, pH 7.4, 150 mM NaCl and 0.1% Tween-20), and incubated overnight at 4 °C with specific primary antibodies. Subsequently, the membrane was washed with TBST buffer and incubated with horseradish peroxidase-conjugated secondary antibodies. Enhanced chemiluminescence kits were used (Amersham, ECL kits).

In order to confirm whether SWCNT can stimulate HEK293 cells secrete small molecular proteins, HEK293 cells were cultured for 1–5 days in essential medium without 10% fetal calf serum with the aim of excluding mistaking fetal calf serum proteins as secreted small molecular proteins.

4.2.8 Immunofluorescent staining analysis

HEK293 cells with 25 $\mu\text{g}/\text{ml}$ of SWCNT were cultured on sterile coverslips at 37 °C in a humidified atmosphere of 5% CO₂ in air and cultured for 1–5 days. The cells were then washed briefly in PBS, fixed with –20 °C methanol for 10 min and with –20 °C acetone for 1 min. The coverslips were washed twice in PBS, and blocked with PBS containing 0.1% BSA for 10 min at room temperature followed by draining. The cell-side-up of coverslips was incubated with antibody (1:2000) in PBS containing 1% BSA for 60 min, and was washed for three times in PBS. The coverslips cell side-up was incubated with anti-mouse FITC conjugate as the secondary antibody, at the recommended dilution, in PBS containing 1% BSA, for 30 min, and then was washed for three times in PBS. One drop of aqueous mounting medium was added on the coverslip and inverted carefully on a glass slide. The cells were observed by a fluorescence microscope with appropriate filters and taken photography.

4.2.9 Microarray analysis

4.2.9.1 Fabrication of microarrays

Hundred pairs of oligonucleotides probes associated with cell cycle, cell apoptosis and signal transduction were designed and synthesized (MWG, Germany), and were fabricated into microarrays according to standard method. As a quality control, Spot Report™ Oligo™ Array Validation System (Cat 252170-7) was purchased from Stratagene® company.

Extraction of total RNAs and probe preparation

HEK293 cells with 25 µg/ml of or without SWCNT were cultured in 200 ml culture bottles at 37 °C in a humidified atmosphere of 5% CO₂ in air for two days. Then the cells were collected and washed repeatedly with PBS (pH 7.4) until the SWCNTs were completely removed away. Total RNAs from 1 × 10⁶ HEK293 cells, cultured with 25 µg/ml of or without SWCNTs for two days, were extracted by using total RNA extraction kit from Promega Inc. Final total RNAs were dissolved in RNase-free H₂O and diluted into the concentration of 0.5 µg/l. Fluorescent-labeled cRNA probes were prepared through reverse transcription and purified. The probes from HEK293 cells with 25 µg/ml of SWCNT were labeled with Cy5-dUTP, and the probes from HEK293 cells without SWCNT were labeled with Cy3-dUTP. These probes were mixed and precipitated by ethanol, and finally dissolved in 20µl hybridization solution (5×SSC + 0.2% SDS)⁷⁹.

4.2.9.2 Hybridization and washing

After denaturing at 95 °C for 5 min, the probes were added onto slides, covered with a cover and incubated at 42 °C for 17 h. The slides were subsequently washed in solutions of 2×SSC + 0.2%SDS, 0.1×SSC + 0.2% SDS and 0.1×SSC, 10 min each time, and dried at room temperature.

4.2.9.3 Detection and analysis

Affymetrix®428™ Array Scanner was used to collect the image of post-hybridization chip. ImageGene 3.0 software (BioDiscovery Inc.) was used to quantify, correct for background noise and normalize signals from hybridization chip.

4.2.10 Data analysis

All data are presented as mean results \pm S.D. Statistical differences were evaluated using the t-test and considered significance at $P < 0.01$ level. All figures shown were obtained from three independent experiments with similar results.

4.3 Results

4.3.1 Effects of SWCNTs on the viability and proliferation of HEK293 cells

Since cell viability is positively correlated with the degree of MTT reduction, the cell viability of SWCNTs-treated HEK293 cells were evaluated by using MTT reduction assays. As indicated in Fig. 4.2, treatment of HEK293 cells with various concentrations (0.8 μ g/ml, 1.6 μ g/ml, 3.1 μ g/ml, 6.25 μ g/ml, 12.5 μ g/ml, 25 μ g/ml, 50 μ g/ml, 100 μ g/ml, 150 μ g/ml and 200 μ g/ml of SWCNTs caused a time- and dose-dependent decrease in cell viability relative to the control culture.

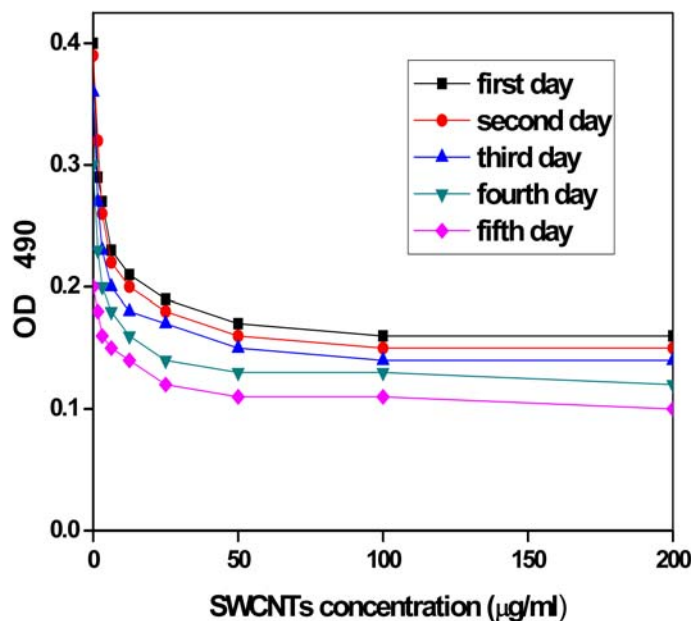


Figure 4.2: HEK293 cells viability curve measured by MTT assay. The percentage of cell viability was calculated as a ratio of OD of SWCNTs-treated cells and control cells. Cell number was measured by Trypan blue dye exclusion method and the percentage of cell growth was calculated as a ratio of numbers of SWCNTs-treated cells and control cells (treated with 0.5% DMSO vehicle).

As indicated in Figure 4.2, treatment of HEK293 cells with various concentrations of SWCNTs caused a time and dose-dependent decrease in cell number relative to control cultures. This result showed that SWCNTs can inhibit the proliferation of HEK293 cells.

4.3.2 Effect of SWCNTs on cell adhesion

The adhesive ability of SWCNT-treated HEK293 cells can be evaluated with the ratio of SWCNTs treated adhesive cell number to the control adhesive cell number after centrifuge. As shown in Figure 4.3, the cell adhesive ability decreased markedly with the increase in SWCNT concentration and culture time.

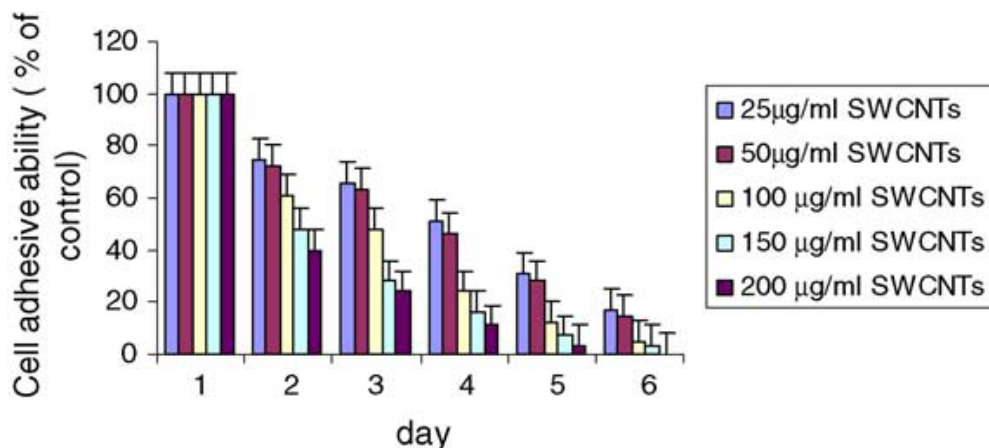


Figure 4.3: SWCNT-treated HEK293 cell adhesion ability measured by centrifugation method. The percentage of adhesive cells decreased markedly with the increase in SWCNT concentration and culture time.

4.3.3 Induction of apoptosis of HEK293 cells by SWCNTs

Microscopic observation of SWCNTs-treated HEK293 cells showed that some HEK293 cells rounded up and detached from the culture plates after 24 h of incubation. As the dose of SWCNTs in the medium reached 25 µg/ml and cultured for over 24 h, the cultured cells displayed morphological changes characteristic of apoptosis. As shown in Figure 4.4 A, HEK293 cells cultured with 25 µg/ml SWCNTs for 72 h exhibited features characteristic of apoptosis. Cells became round, small and floated as shown in A0 compared with control cells; apoptotic cells formed nodular structure encapsulating SWCNTs as shown in A1; black SWCNTs attached to apoptotic cells as shown in A2. These apoptotic cells were further observed to exhibit typical apoptosis features such as membrane vesicles, nucleus condensation, fragmentation and apoptotic bodies. DNA ladder electrophoresis in Figure 5B showed that HEK293 cells cultured with 25 µg/ml of SWCNTs for 24 h exhibited typical apoptosis ladder, which became more and more marked as the cell culture days increased, however, the control cells exhibited no DNA ladder. Cell cycle analysis of HEK293 cells with 25 µg/ml, 50 µg/ml, 100 µg/ml and 150 µg/ml SWCNTs is shown in Table 1. When the concentration of SWCNTs reach 25 µg/ml and cultured for 24 h, the cell cycle was arrested in G1, 5.3% cells exhibited apoptotic feature.

Similar results were also observed respectively at 50 µg/ml, 100 µg/ml, 150 µg/ml SWCNTs cultured for 24 h. As cell culture days increased, the number of cells following the

normal cell cycle of G1, G2 and M phases continued to drop, while that of apoptotic and dead cells continued to rise. Figure 5c depicts the cell cycle distribution of HEK293 cells with 25 $\mu\text{g/ml}$ SWCNTs cultured for four days, indicating that the percentage of apoptotic cells reach 43.5%, a high sub-G1 peak (apoptosis peak) appeared before the G1 phase peak. These results confirmed that SWCNTs could cause cell cycle arrest in G1 and induce HEK293 cells apoptosis in a dose and time-dependent manner.

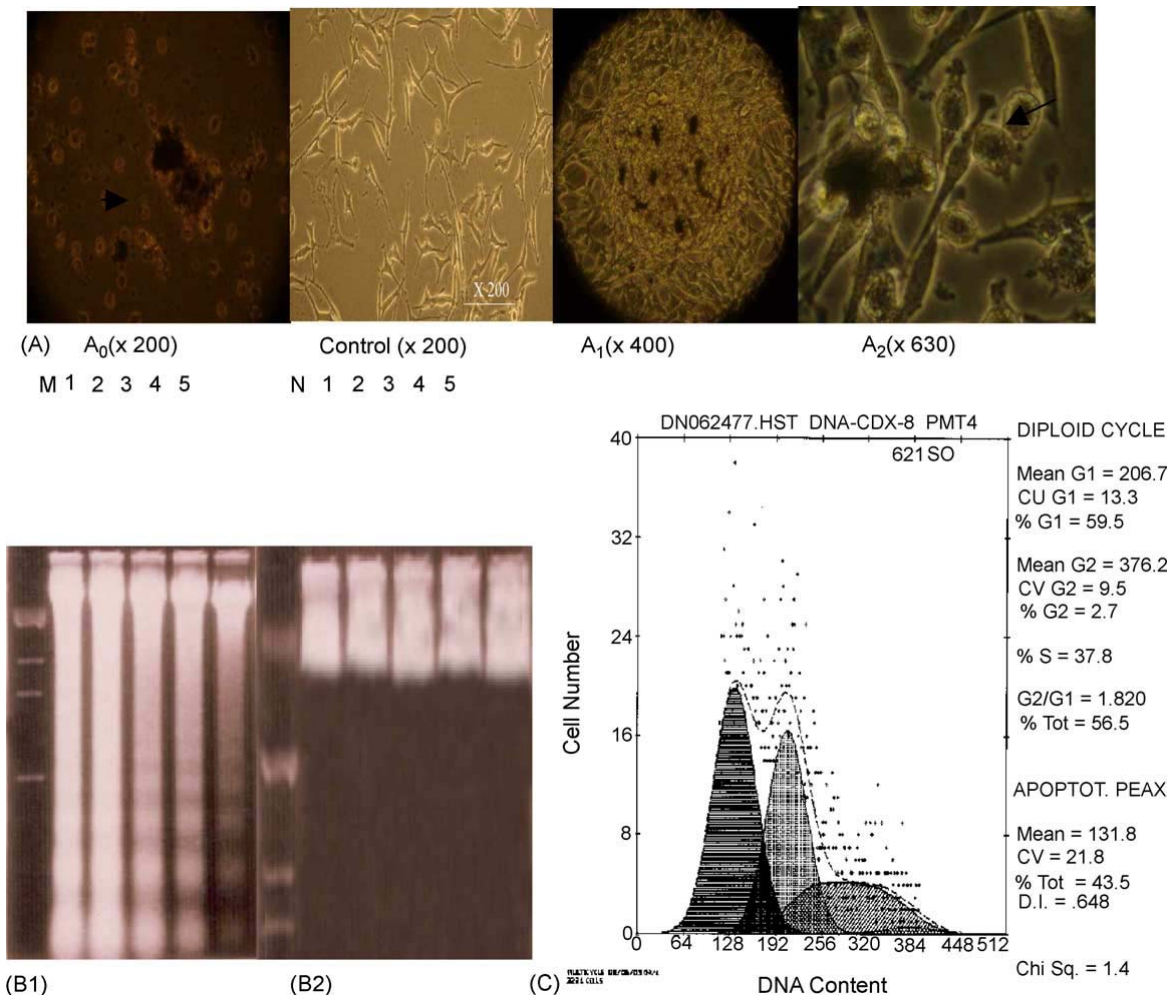


Figure 4.4: Apoptosis of HEK293 cells to SWCNTs.

A: morphological changes of HEK293 cells cultured with 25 $\mu\text{g/ml}$ SWCNTs for three days; A_0 : showing cells become round and floating with apoptotic characteristics; control: showing normal morphological cells; A_1 : showing nodular structure composed of SWCNTs and apoptotic cells; A_2 showing apoptotic cells attached by SWCNTs. B1: DNA electrophoresis of cells cultured with 25 $\mu\text{g/ml}$ SWCNTs for 1–5 days, M molecular marker, no. 1–5 denote the results of cells cultured for day 1–5, respectively; B2: DNA electrophoresis results of control cells cultured for day 1–5; C: the cell cycle distribution of HEK293 cells cultured with 25 $\mu\text{g/ml}$ SWCNTs for four days, the percentage of sub-G1 cells (apoptosis cells) was 43.5%.

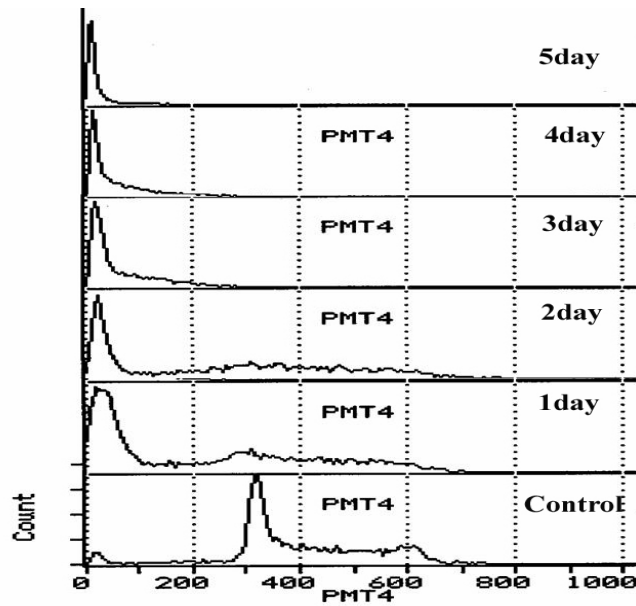


Table 4.1: Cell cycle analysis of control 293 cells and SWCNT-treated 293 cells

SWCNT concentration (g/ml)	Time (h)	Distribution ratio (%)			
		G1	S	G2/M	Apoptotic
0	24	35.0 ± 1.7	51.0 ± 2.6	11.0 ± 0.6	0.0
0	48	37.9 ± 1.8	50.0 ± 2.5	12.1 ± 0.7	0.0
0	72	37.1 ± 1.8	49.8 ± 2.4	13.1 ± 0.6	0.0
0	96	32.2 ± 1.9	50.9 ± 2.5	12.9 ± 0.5	0.0
25	24	70.0 ± 3.5	26.0 ± 1.3	4.0 ± 0.2	5.3 ± 0.3
25	48	64.5 ± 3.2	32.7 ± 1.6	2.7 ± 0.1	16.4 ± 0.8
25	72	61.0 ± 3.1	28.9 ± 1.4	10.1 ± 0.5	25.4 ± 1.3
25	96	59.5 ± 2.9	37.8 ± 1.8	2.7 ± 0.1	43.5 ± 2.2
50	24	45.8 ± 2.3	38.2 ± 1.9	16.0 ± 0.8	32.2 ± 1.6
50	48	62.4 ± 3.1	33.3 ± 1.7	4.3 ± 0.2	51.4 ± 2.6
50	72	38.2 ± 1.9	33.1 ± 1.6	29.7 ± 1.5	60.5 ± 3.0
100	24	88.2 ± 4.4	9.6 ± 0.4	2.2 ± 0.1	48.8 ± 2.4
100	48	12.7 ± 0.6	36.7 ± 1.8	50.6 ± 2.5	57.9 ± 2.8
100	72	0.0 ± 0.2	33.1 ± 1.6	66.9 ± 3.3	64.8 ± 3.2
150	24	80.1 ± 4.0	5.0 ± 0.2	9.0 ± 0.4	52.1 ± 2.6
150	48	58.0 ± 2.9	31.0 ± 1.6	4.0 ± 0.2	61.9 ± 3.1
150	72	32.4 ± 1.6	9.6 ± 0.4	1.9 ± 0.1	78.5 ± 3.9

4.3.4 Effect of SWCNTs on adhesive proteins and cyclin D3 in HEK293 cells

As shown in Figure 4.5, Western blot analysis showed that the expression of adhesive proteins such as laminin, fibronectin, FAK, cadherin and cell cycle protein cyclin D3 in HEK293 cells decreased gradually as the culture days and the amount of SWCNTs increased. The expression of these adhesive proteins in the control cells exhibited no significant difference ($P > 0.05$). Indirect immunofluorescent staining analysis demonstrated, the expression levels of cadherin and collagen IV in the control cells cultured for day 1–5 didn't exhibit significant difference ($P > 0.05$), however, their expression levels in HEK293 cells cultured with SWCNTs for day 1–5 decreased gradually as the culture days increased as shown in Figure 4.5 ($P < 0.01$).

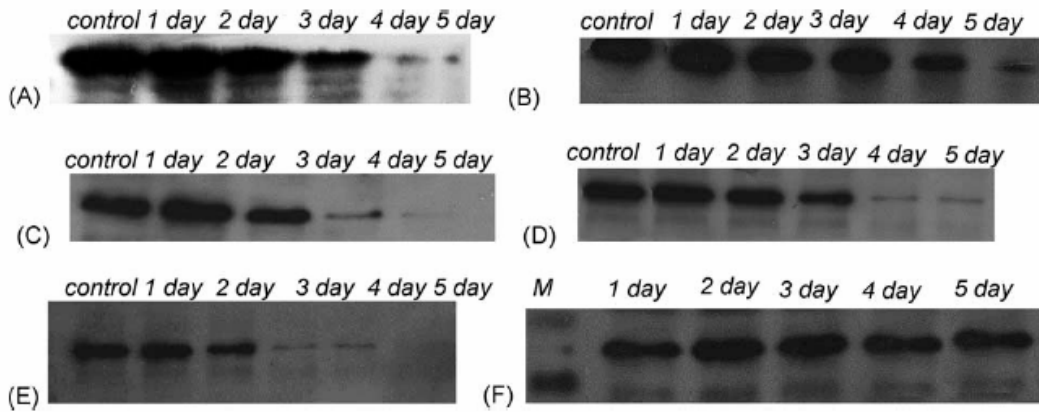


Figure 4.5: Western blot analysis of adhesion proteins in HEK293 cells cultured with 25 µg/ml of SWCNTs for 1–5 days. A–E: expression results of laminin, fibronectin, FAK, cadherin, cyclin D3, respectively; controls in A–E: expression results of matched adhesion proteins in normal cells culture; F: expression of actin in these samples to normalize each lane for protein content; *M*: protein marker, F1–F5: expression of actin in these samples cultured for day 1–5.

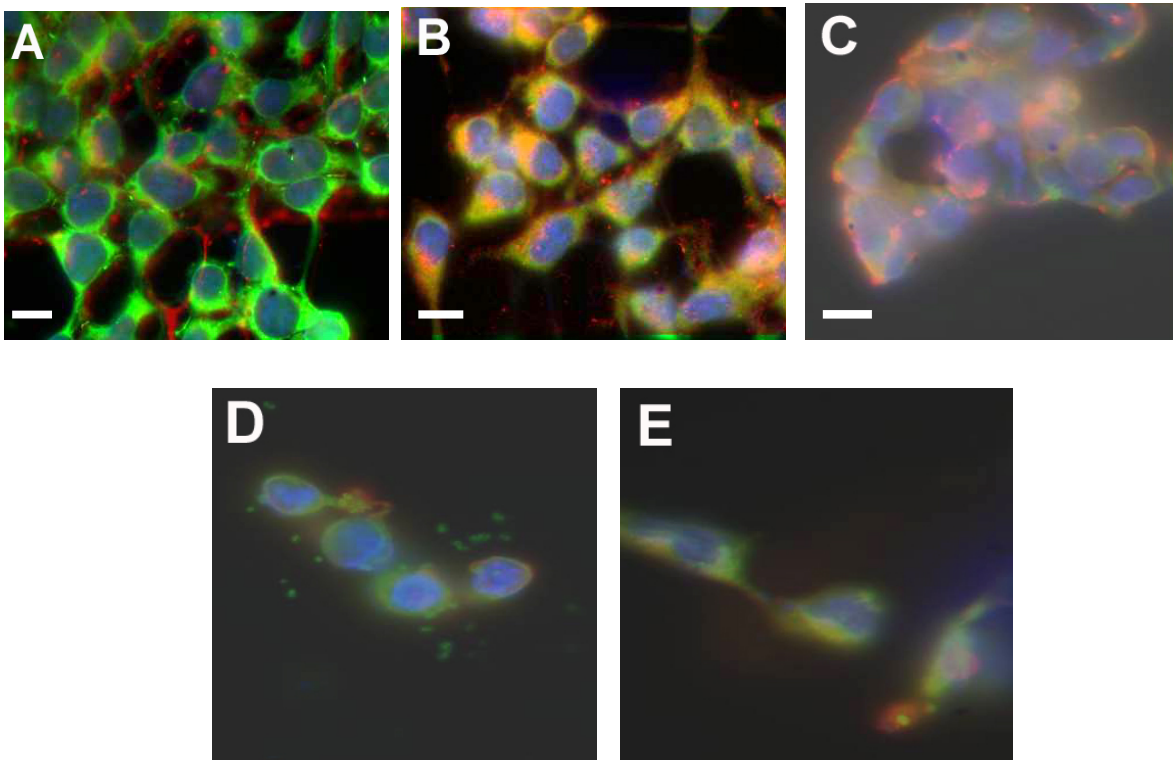


Figure 4.6: Indirect immunofluorescent staining of SWCNTs-treated HEK293 cells for 1–5 day by fluorescent microscopy. (A–D: 1 day to 5 day) Green: cadherin; red: collagen; blue: cellular nucleus staining with DAPI. The expression levels of cadherin and collagen IV in cells decreased gradually as the culture days increased; HEK293 cells gradually detached from the cell populations as the culture days increased. (Scale: 50µm)

4.3.5 Active responses of HEK293 cells to SWCNTs

When added in the culture bottle of HEK293 cells, SWCNTs were initially uniformly distributed but began to attach to cell surfaces within a few hours. When the concentration of SWCNTs reached 5 $\mu\text{g/ml}$, the HEK293 cells produced a series of interesting reactions.

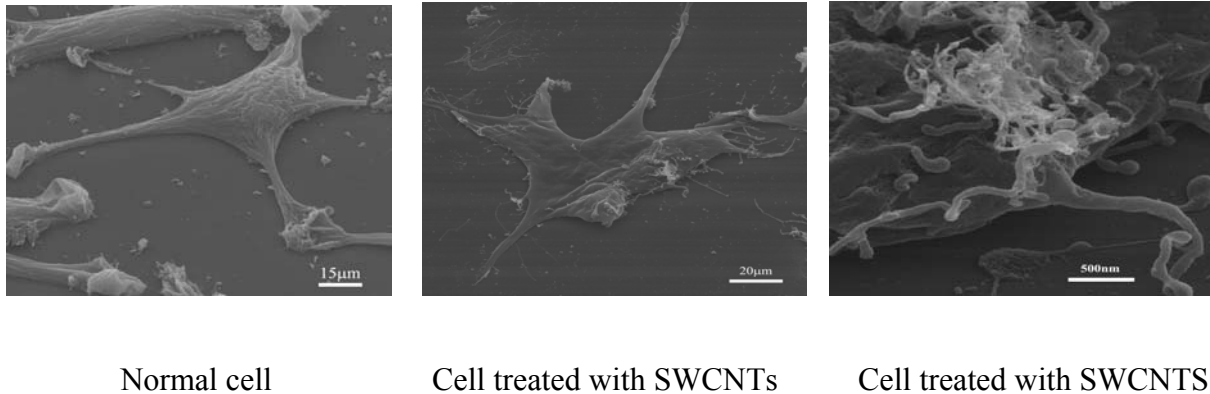


Figure 4.7: Active responses of HEK293 cells to SWCNTs

On the 2nd day, some SWCNTs were aggregated together and surrounded by HEK293 cells, as shown in Figure 4.7 and 4.8. The aggregated SWCNTs were wrapped by some proteins secreted by HEK293 cells (Fig. 4.8B). As indicated in Figure 4.8, the cells began to secrete several 20–30 kD proteins on the 2nd day after SWCNTs were added into the culture, these proteins were still secreted on the 3rd day, but can't be secreted on the 4th and 5th days. These proteins were also not detected in HEK293 cells cultured in the absence of SWCNTs. In order to further confirm that HEK293 cells secrete small molecular proteins, the free-serum culture reagents were respectively used to culture HEK293 cells with 25 $\mu\text{g/ml}$, 50 $\mu\text{g/ml}$ and 100 $\mu\text{g/ml}$ SWCNTs for day 1–5. In the collected cell supernatant fluids were confirmed to exist 20–30 kD proteins on the 2nd day after SWCNTs were added into the culture reagents by 15% SDS PAGE analysis. The structure and functions as well as secreted mechanism of secreted small proteins are still under investigation.

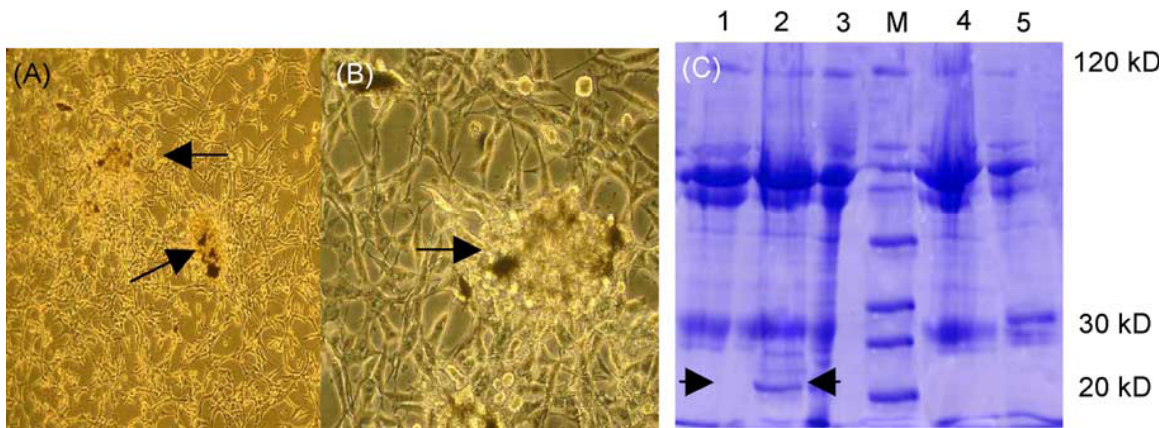


Figure 4.8: Responses of HEK293 to single wall carbon nanotube. (A) SWCNTs were aggregated together and surrounded by HEK293 cells ($\times 100$). (B) The aggregated SWCNTs were surrounded by secretion from HEK293 cells ($\times 200$). (C) SDS-PAGE result showed that some 20–30 kD proteins existed in the supernatants of HEK293 cells with 25 $\mu\text{g}/\text{ml}$ SWCNTs. *M* is protein marker; the n^o. 1–5 denote the results for HEK293 cells cultured with SWCNTs for 1–5 days, respectively, showing some small secreted proteins were only detected on the day 2 and day 3 after SWCNTs were added inside the cell culture.

4.3.6 Gene expression profile between HEK293 cells with or without SWCNTs by oligonucleotide microarrays

The expression levels of genes associated with cell cycle, cell apoptosis and signal transduction in HEK293 cells cultured with 25 $\mu\text{g}/\text{ml}$ of or without SWCNTs for two days were analyzed by oligonucleotide microarrays as shown in Figure 4.9 and Table 4.2.

The analysis showed that HEK293 cells were arrested in the G1 phase, with Rb/P53 as the main apoptosis pathway induced by SWCNTs as shown in Table 4.1.

Apoptosis-associated genes such as p16, bax, hrk, bak1, p53, p57, FGFR2, TGF beta receptor 1 (TGFbetaR1) and TNFAIP2 exhibited up-regulation expression, further supporting that SWCNTs may induce apoptosis of HEK293 cells.

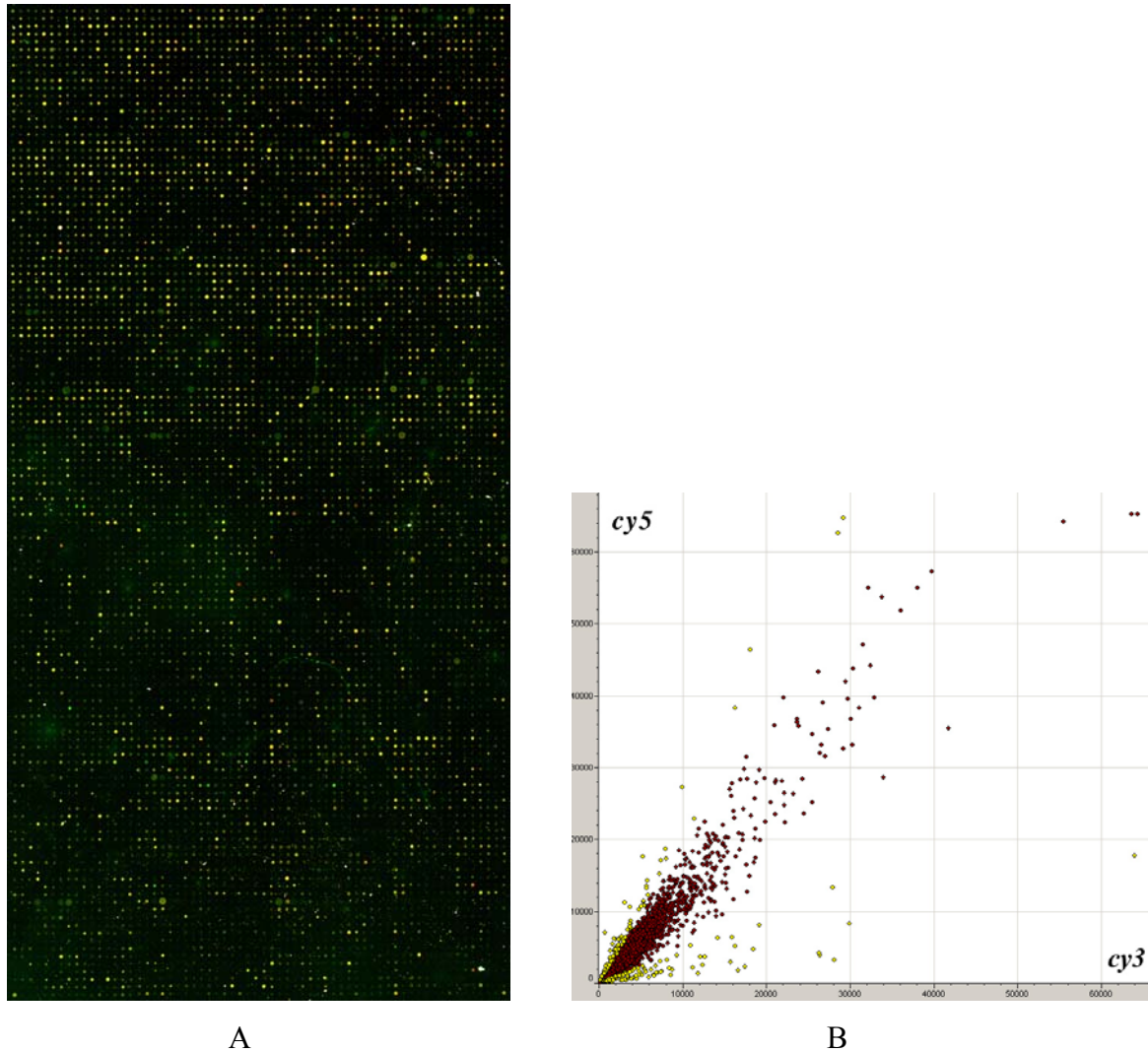


Figure 4.9: Result of oligonucleotide microarrays analysis. A: partial scanning image of hybridization of microarrays with samples, the red colour means higher expression of genes, blue colour means lower expression of genes; B: scatter plot of expression levels of genes in samples.

G1/S phase associated genes (cyclin D1, cdk4, cdk6, cyclin E2, cyclin-E binding protein 1, cdk2, cdk3 and cdc25), S phase associated genes (cyclin A1, cdc25a and cdk2), G2 phase associated genes (cyclin A2, cdk8, cdk9, cyclin C, cdc25c and cyclin D3), M phase associated genes (cyclin M3, cyclin b2, cdc14a and cyclin M2) all showed down-regulation expression, cell cycle genes such as PP2A, cyclin G1, cyclin G2, cyclin I, cdc37, cdc42 and cdc46 exhibited up-regulation expression, these results fully confirmed that the HEK293 cells were arrested in the G1/S phase, and SWCNTs prevented the cells from continuation into the S, G2 and M phases.

The biochip analysis also showed that genes associated with signal transduction such as mad2, jak1, tkk, tyk2, early growth response 1, Pa2g4, cadherin-5, CNGA1, PCDHA9 and

CACNA2D3 exhibited downregulation expression, those genes such as bmp2/bmp4, mmp9, GABA, FGFR2, TGF beta receptor 1 and TNFAIP2 exhibited up-regulation expression. We also observed that SWCNTs can decrease tyrosine kinase activities, induce down-regulation expression of mad2, cyclin D1, cyclin A, cyclin E and upregulation expression of TGF beta receptor 1, cdc37, cdc42 and down-regulation expression of special complexes such as cyclin–cdk, GTP–cdc42 complex.

Table 4.2. Differential genes between HEK293 cells with or without CNTs by biochip.

GenBank no.	Gene	Ratio	P value
L49240_1	<i>FGFR2</i>	3.9	1.92E-05
M13077_1	<i>PP2A</i>	3.5	3.63E-05
M22490_1	<i>Bmp2/bmp4</i>	3.7	1.37E-03
NM_000807_1	<i>GABA</i>	3.2	2.88E-05
NM_001237_1	<i>Cyclin A2</i>	-3.3	3.67E-05
NM_001258_1	<i>Cdk3</i>	-3.4	6.03E-03
NM_001259_1	<i>Cdk6</i>	-2.5	7.89E-07
NM_001260_1	<i>Cdk8</i>	-2.7	2.65E-05
NM_001758_1	<i>Cyclin D1</i>	-3.9	7.93E-07
NM_001760_1	<i>Cyclin d3</i>	-4.5	1.34E-05
NM_001789	<i>Cdc25a</i>	-3.3	3.67E-05
NM_001964_1	<i>Early growth response 1</i>	-4.6	2.64E-05
NM_002134_1	<i>Hmox2</i>	-2.7	1.34E-05
NM_002227_1	<i>Jak1</i>	-4.3	1.32E-05
NM_003331_1	<i>Tyk2</i>	-2.9	9.35E-06
NM_003806_1	<i>Hrk</i>	3.3	7.13E-04
NM_004324_1	<i>Bax</i>	3.5	3.66E-05
NM_004612_1	<i>TGFbetaR1</i>	2.9	5.65E-06
NM_004701_1	<i>Cyclin b2</i>	-4.4	1.89E-05
NM_004702	<i>Cyclin E2</i>	-5.2	1.88E-05
NM_004748_1	<i>Cpr8</i>	-4.0	2.92E-06
NM_004994_1	<i>Mmp9</i>	4.3	4.56E-05
NM_005190_1	<i>Cyclin C</i>	-2.5	5.01E-05
NM_006191_1	<i>Pa2g4</i>	-2.9	2.92E-06
NM_006542_1	<i>SPHAR</i>	2.8	1.24E-06
NM_006835_1	<i>Cyclin I</i>	3.6	1.19E-05
NM_007065_1	<i>Cdc37</i>	3.3	7.13E-04
NM_018398_1	<i>CACNA2D3</i>	-3.6	7.92E-07
NM_021872	<i>Cdc25b</i>	-3.1	9.35E-06
NM_031857_1	<i>PCDHA9</i>	-2.5	1.59E-04
NM_033312_1	<i>Cdc14a</i>	-3.5	3.63E-05
NM_052987_1	<i>Cdk2</i>	-3.2	3.42E-05
NM-000546	<i>P53</i>	-3.1	4.89E-04
S42457_1	<i>CNGA1</i>	-4.1	9.45E-03
U064137_2	<i>P57 kip2</i>	3.4	3.66E-05
U12820-1	<i>P16</i>	4.4	2.92E-06
U46917_1	<i>BAG1</i>	2.9	3.65E-05
U65410	<i>Mad2</i>	-3.4	1.89E-05
U97680_1	<i>Cyclin A1</i>	-3.0	2.92E-06
X74795_1	<i>Cdc46</i>	3.7	1.36E-03
X74795_1	<i>Cdc46</i>	-4.4	1.89E-05
XM_003492_1	<i>Cyclin-E binding</i>	-3.0	2.92E-06
XM_003628_1	<i>Cyclin G2</i>	3.4	3.66E-05
XM_007258_1	<i>TNFAIP2</i>	2.6	6.41E-06
XM_008531_1	<i>Rabaptin-5</i>	4.5	1.34E-05
XM_041406_1	<i>Ttk</i>	-3.5	3.37E-05
XM_057942_1	<i>Bak1</i>	4.5	1.34E-05
Y13120_1	<i>Cdk4</i>	-3.1	4.37E-06
Z47993_1	<i>Fas soluble protein</i>	-3.3	5.66E-04

Specification: cut off value of ratio associated with differential expressed genes is set as >2.5, + denotes up-regulation expression, – denotes down-regulation expression.

4.4 Discussion

Carbon nanotubes, because of their unique properties, have great potential applications on biomedical engineering and medical chemistry. For example, carbon nanotubes own catalytic function, which possibly affect cellular metabolism⁸⁰. Carbon nanotubes can be filled with target DNA molecules or peptides, which has high potential in delivering target DNA molecules or peptides into special tissue region to treat the diseases⁸¹. Carbon nanotubes were previously shown to inhibit the growth of rat nerve cells and have cytotoxicity to human keratinocyte cells²³. Our present study mainly investigates the effect of SWCNTs on human embryo kidney cell line HEK293 and potential biochemistry mechanism with the aiming at exploring biocompatibility and potential therapy value.

Our observation shows that SWCNTs can inhibit the proliferation of HEK293 cells, induce cell apoptosis and decrease cellular adhesive ability in a time- and dose-dependent manner. While a high SWCNT concentration of 250 $\mu\text{g/ml}$ induces death of HEK293 cells within 24 h, less than 1 $\mu\text{g/ml}$ SWCNTs in the medium appear to have only slight influence (Fig. 3). HEK293 cells are attached by SWCNTs and secrete some 20–30 kD proteins to wrap and aggregate SWCNTs to form nodular structures. These appear to be a series of cell active responses aimed at isolating SWCNTs from the remaining cell mass.

In order to explore the molecular mechanism of effect of SWCNTs on HEK293 cells, we analyzed changes in cell cycle induced by SWCNTs. The analysis revealed G1 arrest of HEK293 cells after exposure to 25 $\mu\text{g/ml}$ of SWCNTs in the medium, and this arrest was accompanied by a dramatic decrease in the number of cells in the S phase. We also observed a significant up-regulation expression of p16, which is known to regulate the activity of cyclin-dependent kinases (cdks), the heart of the eukaryotic cell cycle engine⁸². In SWCNTs-treated HEK293 cells, accumulated p16 protein may bind to and inhibit the kinase activity of cdk2, cdk4 and cdk6, hence prevent the cells from entering into the S phase and subsequently arrest the cell cycle in the G1 phase. The SWCNTs treated HEK293 cells showed marked down-regulation expression of cdk2, cdk4, cyclin A, cyclin D3 and cyclin E genes. Western blot indicated that the expression of cyclin D3 in SWCNTs-treated HEK293 cells decreased gradually as the culture time and dose of SWCNTs increased. It has been documented that cdk4 and cdk6 are activated in association with D-type cyclin in the mid G1 phase⁸³. Cyclin D, a G1/S cyclin, promotes S phase by inhibiting Rb. A second G1/S cyclin, cyclin E, is a principal regulator of the S phase during cell development. Although cyclin E is an inhibitor of Rb, it also has additional Rb/E2F-independent cell-cycle roles⁸⁴. Cdk2 is associated with cyclin E in the late G1 phase and its activity is rate-limiting for progression from the G1 to the S phase,

regulating both the passage from G1 into S and the S phase progression. Cdk2 down-regulation expression may result in cell arrest in the G1 phase⁸⁵. Thus, reduced levels of these G1-associated cdks and cyclins may also facilitate blockade of the cell cycle in mid G1 and G1/S in SWCNTs-treated cells. These results provided solid evidences that SWCNTs suppress the proliferation of HEK293 cells by the p16–cyclin D–Rb pathway. Our observations show that SWCNTs can induce HEK293 cell apoptosis, which were characterized by morphological changes, chromatin condensation and internucleosomal DNA fragmentation, accompanied by up-regulation expression of apoptosis-associated genes such as p16, bax, hrk, bak1, p57, FGFR2, TGF beta receptor 1 and TNFAIP2 genes and downregulation expression of cell cycle-associated genes such as cyclin D1, cdk2, cdk4 and cdk6 compared to normal HEK293 cells. The family of bcl-2 related proteins regulates susceptibility to apoptosis. Antiapoptotic members of the bcl-2 family, including bcl-2 and bcl-XL, which act to prevent or delay cell death, while pro-apoptotic members, including bax and bcl-Xs, which promote apoptosis⁹⁰. Our data showed that the expression of bax and bcl-Xs were up-regulated in SWCNTs-treated HEK293 cells. It has been reported that Bax is up-regulated by p53 protein. Therefore we consider that the bcl-2 family is involved in the cell apoptosis induced by SWCNTs. Our data showed that the adhesion ability of HEK293 cells decreased gradually as the amount of SWCNTs and number of culture days increased. Cell adhesion to a substrate controls the behavior of cells such as cell morphology, migration, growth, apoptosis and differentiation.⁶¹ ECM is the substrate for cell adhesion, growth, and differentiation, and it provides mechanical support to tissues. Local disruption of ECM results in selective programmed cell death within adjacent cells⁸⁶. Laminin, FAK, cadherin, fibronectin and collagen IV are important components of ECM. Biochip analyses showed that adhesion-associated genes such as laminin, fibronectin, FAK, cadherin, collagen IV and padh9 exhibited down-regulation expression. Western blot analysis showed that the adhesive proteins such as laminin, fibronectin, FAK, cadherin and collagen IV exhibited gradual down-regulation expression as cell culture days increased. Our data also showed that cdc42 and cdc37 exhibited up-regulation expression, which can lead to cytoskeleton reorganization and cell shape alteration. These results showed that SWCNTs can induce adhesion-associated genes and proteins exhibit down-regulation expression, leading to thinning of cell basement membrane and decrease of the adhesion ability, finally resulting in cellular apoptosis or death.

However, we also observed HEK293 cells actively respond to SWCNTs such as secreting proteins to aggregate and wrap SWCNTs. SDS-PAGE analysis confirmed the existence and size (20–30 kD) of these secreted proteins in the medium. Our observation

showed that HEK293 cells cultured with SWCNTs began to secrete some small proteins on the 2nd day.

The structure, function and secretion mechanism of these small proteins remain to be clarified. We also observed, no matter how uniformly distributed the SWCNTs were at the initial stage, after the cells with SWCNTs were cultured for several hours, some SWCNTs aggregated together and formed bundles in the medium, while some SWCNTs attached to HEK293 cells and resulted in cell aggregation. These cells attached by SWCNTs gradually appeared apoptosis.

The cells far from SWCNTs still grew very well. These observations demonstrate that HEK293 cells can make active responses of self-protection to SWCNTs. The detailed mechanism of active response is under study.

According to the above-mentioned results, we suggest a possible model of interaction between SWCNTs and HEK293 cells. The SWCNTs attach to the surface of HEK293 cells, providing a stimuli signal to the cells. The signal is transduced inside the cells and the nucleus, leading to down regulation of adhesion-associated genes and corresponding adhesive proteins, resulting in decrease of cell adhesion and causing cells to detach, float and shrink in size. At the same time, SWCNTs induce up-regulation of apoptosis-associated genes such as p16, Rb, p53 and causes HEK293 cells arrest in the G1 phase, finally resulting in apoptosis. During this period, HEK293 cells make active responses of self-protection to SWCNTs, secrete some small proteins into the medium to wrap SWCNTs into nodular structures, which isolate the cells attached by SWCNTs from the remaining cell mass.

In conclusion, SWCNTs can inhibit the proliferation of HEK293 cells by inducing cell apoptosis and decreasing cellular adhesive ability. In return, HEK293 cells can also mobilize active responses including secretion of small “isolation” proteins to isolate SWCNT-attached cells from the remaining cell mass. This phenomenon has potential application in medical chemistry and disease therapy. The secreted proteins possibly are valuable target molecules. The detailed network pathways responsible for the transduction of these signals are complex and still need further clarification.

Chapter 5

Binding RGD to a nanostructured hydrogel

5.1 Introduction

Tissue-like materials, such as some polymeric materials, that are flexible, light and easy to handle, can be used as scaffold for tissue engineering and substrate for the production of neural networks⁸⁷. How best to obtain nanostructured surfaces on tissue-like materials is still an open question. Fortunately, chemical structuring of solid-state interfaces down to the nanometer range has been intensively studied in material sciences. Some research groups have demonstrated that the size of topographic nanoscale features (e.g. grooves or holes) of surfaces represents a fundamental cell stimulus⁸⁸. Nanogrooves (50 – 60 nm) influence the adhesion, spreading, growth, morphology, orientation, and alignment of CHO cells⁸⁹. Nano-pillars of TiO₂ (50-80 nm in diameter, ~25 nm in height) surrounded by a matrix of SiO₂ are useful as model systems for cell-biological studies, scaffold for tissue engineering and substrate for the production of neural networks. Our group has developed a patterning strategy based on self-organization of diblock copolymer micelles that regulate the ligand distance at the nanoscale level⁹⁰. This strategy allows an uniform distribution of molecules.

This chapter introduces polymeric materials, the extracellular matrix, and the RGD peptide that we will use to obtain a stable attachment to the soft nano structure substrate. Finally, it explains how to bind RGD on a nanostructured hydrogel.

5.1.1 Polymers

More than two century ago, people started to study rubbers. For example, in 1770, Joseph Priestley found that rubber was better for erasing out unwanted pencil marks. A century later, Staudinger studied polystyrenes and the polyacetals. Bayer's work on polyurethane began in 1937 in Germany. A year later Castan commenced his studies of epoxies in Switzerland. Polytetrafluoroethylene was discovered in 1938, while Roy Plunkett and Jack Rebok were studying gaseous refrigerants⁹¹. In 1977, MacDairmid, Heeger and Shirakwa discovered that

organic polymer could conduct electricity. Soft materials, which are cheap to manufacture and relatively easy to process, can have better environmental profiles than hard materials. Research on conductive polymers has fuelled the rapid development of molecular electronic, such as conducting biomaterials and plastic solar cells during the last 30 years^{92, 93}.

Tissue engineering is also a rapidly evolving interdisciplinary research area aiming at the replacement or restoration of damaged tissue. At present, the main research themes are: cell and tissue damage due to sustained loading (e.g. decubitus), the use of biomaterials in artificial prosthesis design (e.g. intervertebral discs, small diameter blood vessels), and the engineering of living tissues and organs (e.g. heart valves and intervertebral discs)^{94, 95}. Polymers are flexible, robust, light and easy to handle and can thus be suitable for use as materials in medicine⁹⁶.

In addition, polymers are able to transform from one state to another. Phase transformations have a great deal of potential use in surgery, for example, as adhesives, sealants, and barriers to cell-tissue contact. The polyethylene glycol (PEG) solution can be rapidly transformed into an elastic hydrogel by exposing it to light in the presence of a suitable photo initiator, such as eosin yellowish. The PEG solution that can also be converted from liquids into gel by reaction of N-hydroxysuccinimide activated esters located at the end of a difunctional PEG with amines at the end of a tetrafunctional PEG^{97, 98}.

PA gels, Poly (dimethylsiloxane) (PDMS) and PEG have emerged as important tools for testing the chemical ligand and compliance dependence of activities of cells. The following text will review the recent use of polymers in this research field.

It is well known, that Polyacrylamide (PA) gels are used to separate proteins and nucleic acids in electrophoresis due to their chemical stability and nonadherence to other macromolecules. PA gels as substrates were reported in 1978 and it was shown that chicken hepatocytes bind specifically to such gels. Another early study examined the conjugation of 3T3 fibroblasts to PA gels whose surface had been functional with carboxylic acids and hydroxyl groups. Recently, PA gels have been used as substrate for cell growth in studies to determine the effect of substrate stiffness on cell morphogenesis. However, the disadvantage of PA is that its chemical inertness makes covalent attachments of fragile proteins sometimes difficult⁹⁹.

Poly (dimethylsiloxane) (PDMS) is the most elastomer that is most commonly used to control biomolecular and cell culture environments. PDMS can be patterned with feature sizes ranging from 10 μm to 1 μm . Features of surface topology such as microgrooves and microlines can influence the adhesion, spreading, growth, morphology, orientation, and alignment of cells. For instance, BCE cells align and elongate on fluorescent lectin, erythrocytes and fibronectin

PDMS topographical features which are etched with tetrabutylammonium fluoride solution. Human fibroblasts exhibit more proliferation on PDMS surfaces that have been patterned with 2, 5 μm wide grooves than on surface with 10 μm wide grooves. Cardiac myocytes plated onto stretchable membranes display greater attachment to the laminin PDMS grooves¹⁰⁰.

PEG is a nondegradable, hydrophilic polymer that can be crosslinked into a hydrogel using various chemistries, such as dicarboxylic acids, lactic acids, and amino acids¹⁰¹. Interestingly, aromatic poly(ether ether)s prepared from PEG and either ethylene terephthalate (PEG-PET copolymer) or butylenes terephthalate (PEG-PBT copolymer) were investigated as blood compatible and bonebonding biodegradable materials¹⁰². Due to its high biocompatibility and its low toxicity PEGs are widely used such as biocompatible surface materials in medicinal areas. For example, cell adhesion can be controlled by varying the amounts and conformations of fibronectin adsorbed to the low polymer surface¹⁰³.

5.1.2 Cell adhesion and the extracellular matrix

Cells in tissues are usually in contact with extracellular matrix (ECM). The ECM helps to hold cells and tissues together and provides an organized lattice of sites for cell growth. In vitro, the adhesion of cells to substrates can be promoted by coating the substrate with extracellular matrix molecules, such as fibronectin, collagen and laminin.

Cell-matrix interactions

The ability of cells to contact tightly and to interact specifically with other cells is a key step in the evolution of multicellularity. Various integral membrane proteins, collectively called cell-adhesion molecules (CAMs), are involved in Cadherins, Immunoglobulin superfamily (Ig), Selectins, Mucins and Integrins. Integrins are of the greatest interest because they are generally the only CAM class that is responsible for cell-matrix interactions; all other classes of CAM molecules are principally responsible for cell-cell adhesion¹⁰⁴.

Integrins

Integrins are noncovalent heterodimers made up of α and β subunits¹⁰⁵. The ligand binding site is composed of parts of both chains. In mammals, at least 22 integrin heterodimers, composed of 17 types of α subunits and 8 types of β subunits, are known.

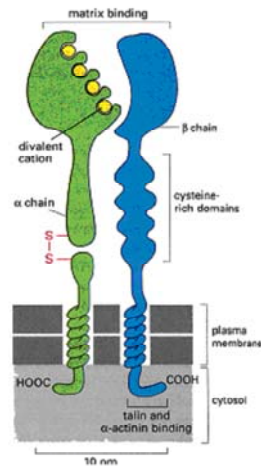


Figure 5.1: Basic structure of integrins, the α chain is made initially as a single polypeptide chain with 1100 amino acids that is cleaved into one small transmembrane chain and one large extracellular chain, which are held together by a disulfide bond. The β chain consists of about 800 subunits; the extracellular part contains a repeating cysteine -rich region, where intrachain disulfide binding occurs¹⁰⁶.

Different chains combine with different β chains to the resulting integrins, which can bind different extracellular matrix molecules such as fibronectin, collagen or laminin.

Fibronectin

The fibronectin binding domain binds specifically to distinct molecules: collagens, heparin or integrins (cell binding site). This domain consists of several smaller modules, the most important one is the so-called type III fibronectin repeat (Fig. 5.2).

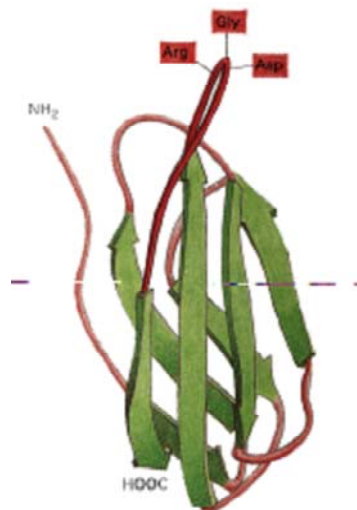


Figure 5.2: Three-dimensional structure of type III fibronectin¹⁰⁸.

Assembly of fibronectin into polymerized fibers present in the ECM is a cell-dependent process which occurs on the surface of many adherent cell types¹⁰⁷. Integrins and integrin-dependent signals regulate the deposition of fibronectin in the extracellular matrix¹⁰⁸.

However, the use of proteins as ligands had several disadvantages. First, it was difficult to obtain a stable attachment to the material. Second, the number of accessible proteins could not be controlled. It is necessary to find out method to bind short adhesion peptides on the soft material.

5.1.3 RGD Peptides on the surface

20 years ago, Arg-Gly-Asp (RGD) was developed as an adhesive recognition sequence for fibronectin by Pierschbacher and Yamada^{109, 110}. Many of the ECM proteins contain the RGD sequence, e.g. vitronectin, fibrinogen, von Willebrand factor, actin, laminin and collagen. Synthetic peptides based on the RGD motifs can mimic the activity of intact proteins, such as, albumin and IgG¹¹¹. They can be used to test the roles of these sites (and of the protein as a whole) in living animals. RGD-dependent processes cell adhesion have been identified in the context of gastrulation and neural crest migration, and in experiments on metastasis¹¹².

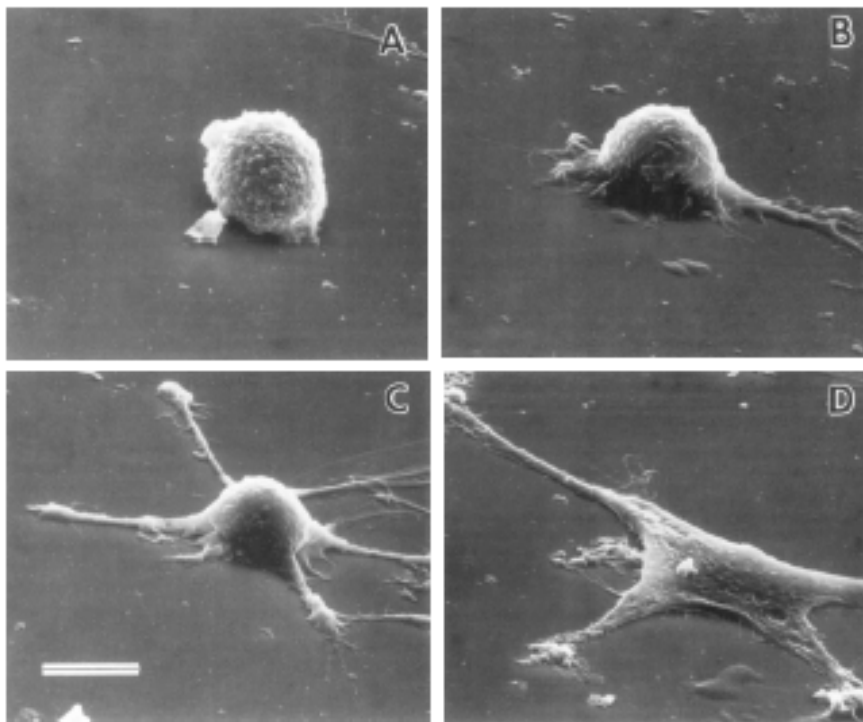


Figure 5.3: Scanning electron micrographs of adherent cells on substrates with covalently grafted GRGDY at increasing concentrations on the surface (0.1, 1, 10, and 100 fmol/cm² from A to D) Scale bar 10 μ m¹¹⁶.

Early work demonstrated an important possible advantage of working with RGD *in vitro* to test its impact on cell behaviour and to prove its applicability for biological use, such as cell attachment, cell spreading, cytoskeletal reorganization and formation of focal adhesions as well as proliferation and cell motility (Fig. 5.3). The RGD sequence is recognised by cellular transmembrane adhesion proteins, the integrin receptors, and this led to intense investigation of

RGD throughout the 1990s. In particular, the sequences flanking the RGD have been selected to give the best possible interaction. The osteoblasts functions were investigated on glass modified with RGDs¹¹³. RGD peptides have sound to control several cell functionalities by controlling the rate of cell spreading, e.g. calcium content, mineralization status and collagen I production of bone cells¹¹⁴ and osteoprogenitor¹¹⁵. Moreover, RGD was founded as an initiate to influence down stream maturation events in osteoblast attachment¹¹⁶. Also, an increase in size and number of mineral deposits is observed in cultures on the RGDS–treated surfaces. These events conformed that surface RGD-grafted surfaces play important roles in cell adhesion, proliferation and apoptosis¹¹⁷.

5.1.4 Immobilization of RGD and proteins on the surface

Linking of RGD peptides and ECM proteins to a surface is essential to promote cell adhesion (Figure 5.4). There are many strategies to immobilize proteins and peptides on the surface. High density covalent and electrostatic bonds can be used to immobilize on proteins and peptides on membranes, hydrogel, and inorganic surface (silica, gold, etc)¹¹⁸. For example, protein can adsorb Poly-L-lysine (PLL)-coated the glass surface via non-specific interactions¹¹⁹. However, due to the washing process, it is difficult to control protein coverage or activity quantitative. Amine-reactive groups, such as aldehyde, epoxy, and activated amides have been created on glass or gold-coated surfaces enabling proteins to be covalently immobilized. These approaches lead to surface-grafted proteins of random orientation and conformation. Another approach involves using affinity-based interactions such as streptavidin-biotin to attach working proteins on the surface. This method is limited because only a small number of such affinity pairs are available¹²⁰.

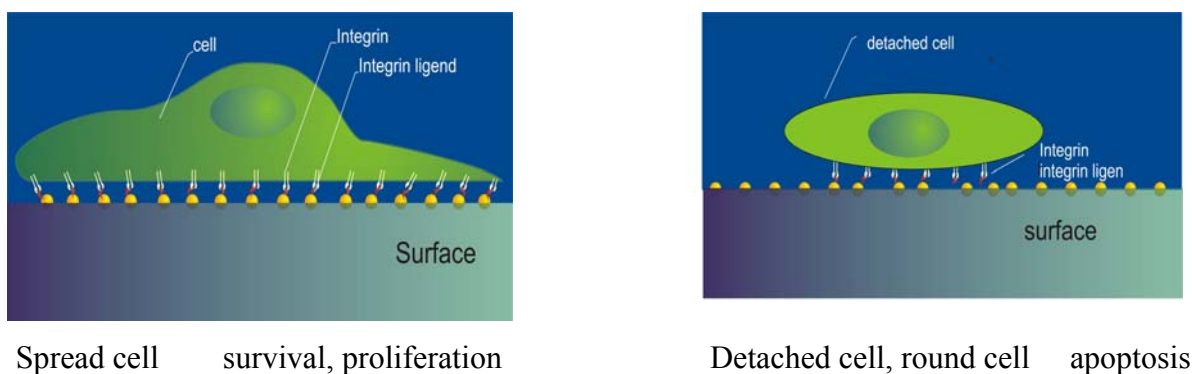


Figure 5.4: Immobilized ligands act as agonists of ECM, leading to cell adhesion and cell survival, while non-immobilized ligands acts as antagonists, leading to cell detachment, a round cell shape, and apoptosis.

In order to provide a stable linking of RGD peptides, to a polymer substrate, RGD should be covalently linked to the polymer, for example via hydroxyl-, amino-, or carboxyl group. For instance, the free amino groups of poly-L-lysine (PLL) can be used to produce amine-functionalized poly (tetrafluoroethylene) (PTFE) grafts, polystyrene (PS) and poly (lactic acid) (PPLA) surface. Moreover, polylysine^{121, 122} and PepTite 2000TM mediate stronger cell adsorption and provide an easy way to modify different materials using a simple coating procedure¹²³. However, the adhesive moieties have to be chosen carefully, because PLL is cytotoxic and PepTite 2000TM can lead to unwanted plasma protein deposition¹²⁴. Reaction of the peptide with an activated surface carboxylic acid group is another possibility to bind the peptide to the polymer. However, there are disadvantages: firstly there are further reactive functional groups in the RGD peptide and secondly the coupling reagent and the activated carboxyl groups can be deactivated quickly by hydrolysis. The first of these problems can be overcome by using protecting groups to block amino acid side chains, but this is a time-consuming process¹²⁵. Instead of using protecting groups in organic solvents, we employ water soluble *N*-hydroxysuccinimide (NHS). The half lifetime of NHS active esters is long¹²⁶, but RGD peptide coupling yields are usually lower under this condition. Also hexamethylene diisocyanate was employed to link surface hydroxyl or amino groups and the peptide¹²⁷. Surfaces which have been RGD functionalized via disulfide formation lack stability. RGD-mediated cell adhesion activity declines after some days, probably due to release of RGD peptide via disulfide exchange¹²⁸. More recent, a bromoacetyl containing RGD cyclopeptide was successfully linked to a thiol functionalized surface¹²⁹ and an aminoxy-terminated RGD cyclopeptide was reacted with aldehyde groups leading to a stable oxime bond¹³⁰.

During the last ten years, many of the studies involving the patterning of proteins and molecules have been carried out by self-assembled monolayer (SAMs) of alkanethiolates on gold¹³¹. Alkane thiols have been employed to link ribonuclease A, pyruvate kinase, fibrinogen, fibronectin, streptavidin, collagen, anti-integrin $\beta 1$ antibody, or anti-integrin $\alpha_v\beta_3$ antibody and immunogloblins on preexisting gold patterns over the end decade of the last century¹³². At beginning, most of all reported that cell cycle progression, proliferation, apoptosis and differentiation of BCE cells were controlled by cell shape and cytoskeletal tension¹³³. The patterning of the attachment of cells has been accomplished by patterning the deposition of metals and by patterning alkylsiloxane monolayers using optical, UV, and plasma lithography. These technical have limitations: in particular, limited special resolution. The lack of a higher resolution patterning method has prevented a direct examination of sizes of subobjects that

within focal adhesions^{134, 135}, and in general it has been difficult to answer question that involve sub-micrometer length scales.

Several methods have been described over the past 10 years for patterning the immobilization of ligands or proteins. A recent theme in patterning has been the development of methods that can control the positions of ligands at a sub-micron resolution. Cells can react to sub-micrometer features, ranging between 50 and 500 nm, by changing their adhesion properties, morphology and gene expression¹³⁶. A variety of nanoarrays of pits in the range of 100 nm, arranged in well ordered orthogonal and hexagonal patterns have also shown to affect cell responses¹³⁷. In this study, we use surface that have been patterned with regularly-spaced gold nanodots to study nanoscale mechanism of cell-environment recognition. At present, we employ a thiol linker method to transfer gold dot to PEG. We confirm that nano pattern can be transferred from a solid substrate to soft materials. Finally, we also link C (RGDfK)-thiols with Au dots to study cell adhesion on the hydrogel.

5.2 Procedure of immobilization of RGD on nanostructured hydrogel

Immobilization of RGD on nanostructured hydrogels involves two steps: The gold dot nanostructures are first prepared on solid substrates and transferred to the PEG hydrogels. RGD is immobilized on the nanostructures.

5.2.1 Gold dot nanostructures on glass

5.2.1.1 Diblock copolymer micelles

Diblock copolymers associate to uniform micelles in selective solvents, where the more soluble block forms a shell around the less soluble block to protect it from energetically unfavourable interactions with the solvent¹³⁸. In this case polystyrene-block-poly (2-vinylpyridine) is dissolved in the non-polar solvent toluene. A hydrophobic polystyrene shell and a hydrophilic poly-2-vinylpyridine core are formed. The P2VP carries thereupon a positive charge, which draws the accumulation of the Tetrachloroaurate. HAuCl_4 protonates the nitrogen atom of the pyridine which then incorporates the tetrachloroaurate (III) in the polar core (Fig. 5.5 and Fig. 5.6)¹³⁹. The formation of the complex is a Lewis or Brønsted acid base reaction.

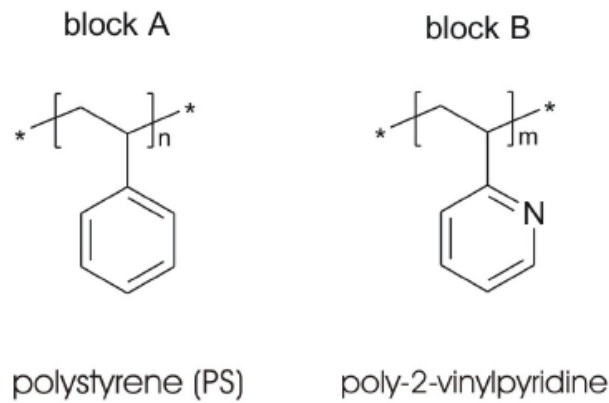


Figure 5.5: Chemical structure of diblock copolymer poly (styrene-b-2-vinyl pyridine)

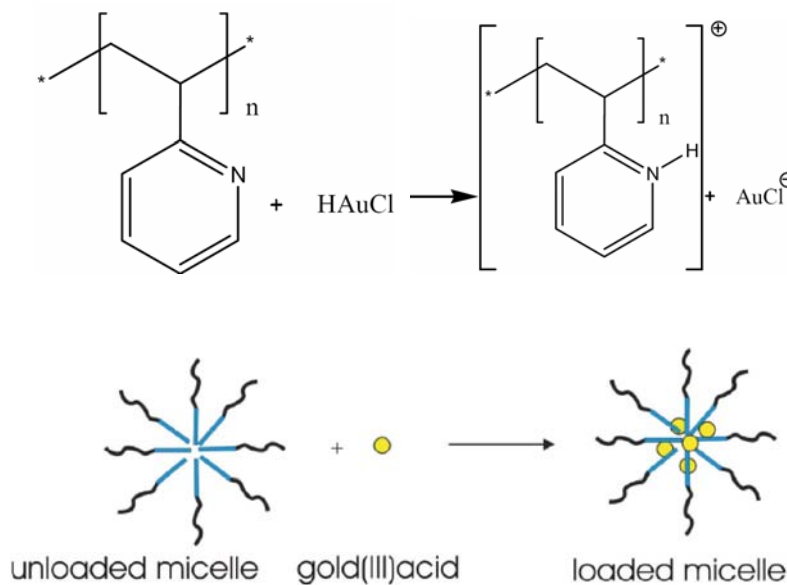


Figure 5.6: Assembly of PS-P2VP diblock copolymers in micelles in non-polar solvent and loading with gold salt.

5.2.1.2 Calculation of the quantity of gold acid [mg]:

$$\frac{m(\text{Polymer})[\text{mg}] \cdot M(\text{HAuCl}_4)[\text{g/mol}] \cdot \text{SU}(\text{P2VP}) \cdot L}{M(\text{Polymer})[\text{g/mol}]} = m(\text{HAuCl}_4)[\text{mg}]$$

$m(\text{Polymer})$: Mass of polymer

$M(\text{HAuCl}_4)$: 393,83 g/mol

$M(\text{Polymer})$: 1800: 245000 g/mol; 500: 83100 g/mol

$\text{SU}(\text{P2VP})$: Number of P2VP; 519 for Polymer(1800) and/or 292 for polymer (500)

L : Loading the molecule HAuCl_4 on P2VPs

5.2.1.3 Formation of thin polymer films

Substrates are dipped into the solutions held these for a certain time and taken out with constant velocity (Fig. 5.7). Due to capillary forces, and to unfavourable steric interactions between the micelles and the surfaces, a mono-layer of micelles is formed on the substrate¹⁴⁰. In a first step, hydrophilic poly-vinylpyridine blocks of the copolymer create a thin polymer film on the substrate by binding to the polar surface and the nonpolar polystyrene groups interact with the micelles in solution^{141, 142}.

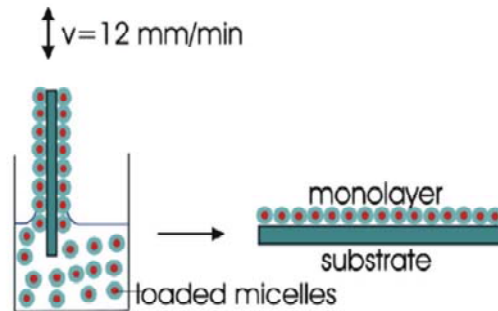


Figure 5.7: loading of micelles and core formation

5.2.1.4 Tessellations in micelles order

Shapes which tessellate cover the plane without gaps and without overlapping. There are only three regular Tessellations on the Euclidean plane (2D plane) that are made from copies of a single regular polygon meeting at each vertex. These are of equilateral triangles, squares or regular hexagons (Fig. 5.7). There are only three because the inside angles of the polygon must be a factor of 360° so that the polygons can line up at the points leaving no gaps.

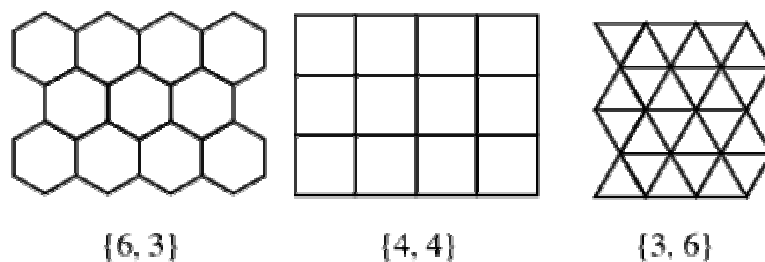


Figure 5.8: The Three Regular Tessellations on the Euclidean Plane

As show theoretically by Kralchevsky *et al.* the capillary forces between the micelle particles immersed in the thin liquid layer on the solid substrate give rise to strong interparticle attractions¹⁴³. This causes a flux directed toward the ordered regions, so that the particles in the ordered phase attract the nearest ones in the 2D plane. The pattern of micelles

that is deposited onto the polymer bush can be considered as an approximately hexagonal arrangement.

5.2.1.5 Reduction and deposition of metal clusters

The hydrogen or oxygen plasma is the most commonly used method for reduction of metal salts. This is a convenient approach for our purposes, as it not only reduce the metal core but also removes the polymer (Fig. 5.9). Due to the low temperature as which our plasma treatment is limited at 20-100 °C and low pressure (0,4 bar), the *quasi*-hexagonal arrangement does not change¹⁴⁴.

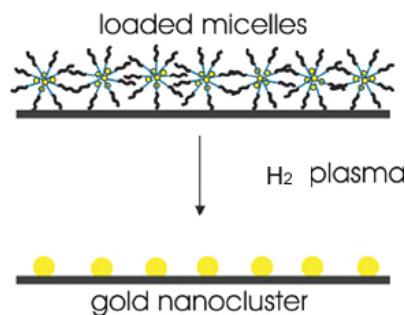


Figure 5.9: Deposition of micelle monolayers

5.2.2 Preparation of polymers

The synthesis of gold nanopatterned PEG requires two different steps: the first one is the addition of cysteamine to the gold nanopatterned glass surfaces (Fig. 5.10). The NH₂ groups are then available for further functionalization. The second step is the addition of Acryloylchloride to the amino functionalized surface (Fig. 5.11). The double bonds of the acrylate groups make it possible for the linkers to polymerize into the PEG. Free radicals are produced when the polymer is exposed to high-energy radiation or irradiated with ultraviolet light. The full procedure will now be described.

(A) There are two linkers for connecting structure. The nano-structured gold surfaces were modified over reaction with Cysteamine with an amino group.

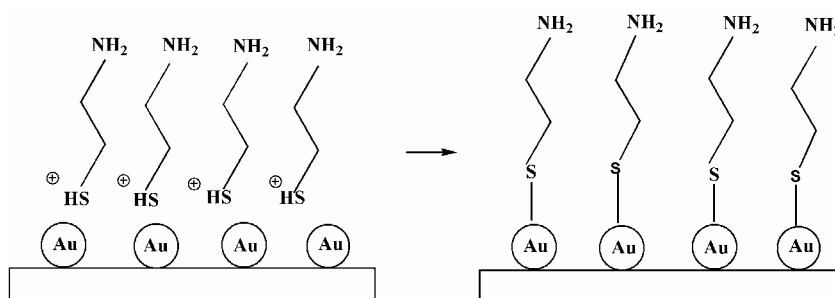


Figure 5.10: The first step: Addition of cysteamine

The added of acryloylchlorid reacts with the amine functionalized surface.

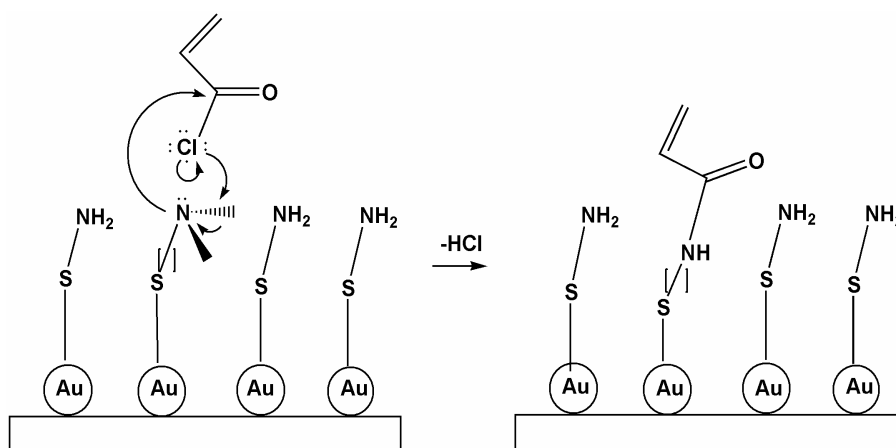


Figure 5.11: The reaction is a second order nucleophilic substitution (SN2).

(B) In order to avoid nonspecific reactions, PEG polymerization has to be carried out under an inert gas atmosphere (N_2). 4-(2-Hydroxyethoxy) phenyl-(2-propyl) ketone is used as initiator. Radicals ($R\bullet$) are formed by using a wavelength of 366 nm UV (Fig. 5.12). PEG diacrylate attacks with radical to the double bonds (Fig. 5.13). In order to avoid premature activation, the radical solutions are protected against light.

Decay of the initiator:

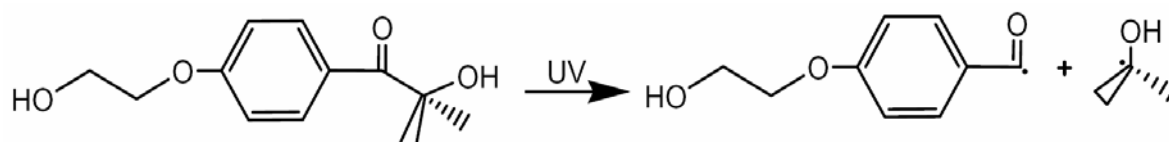


Figure 5.12: The UV light attacks the final double bond of the PEG Diacrylates (PEGDA) radicals.

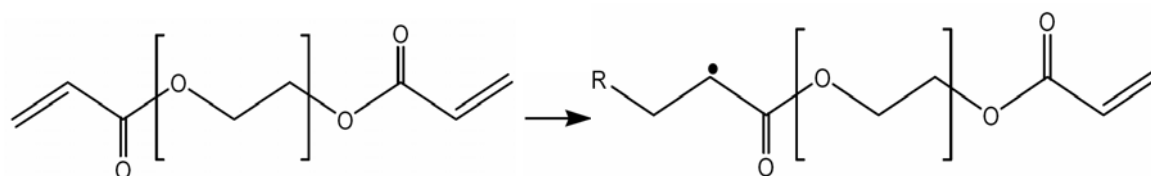


Figure 5.13: The radical attacks the PEGDA.

(C) Chain propagation: The radical attacks a further final double bond (Fig. 5.14). The single bond between the two PEGs is freely swiveling (Fig. 5.15).

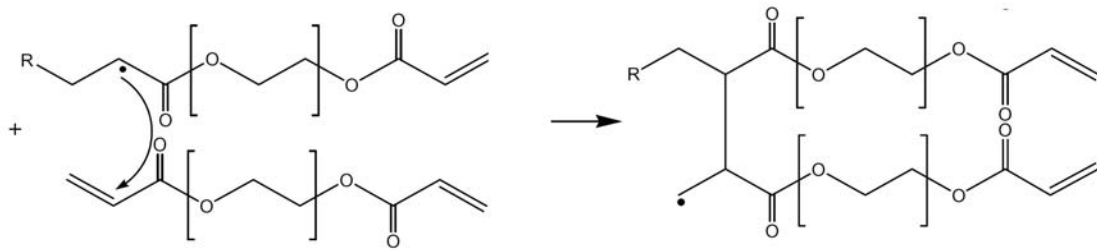


Figure 5.14: The PEG chains are extended by passing on of the radical and/or branch out.

(D) Terminal reaction: The chain reaction breaks off, if two radicals react with another.

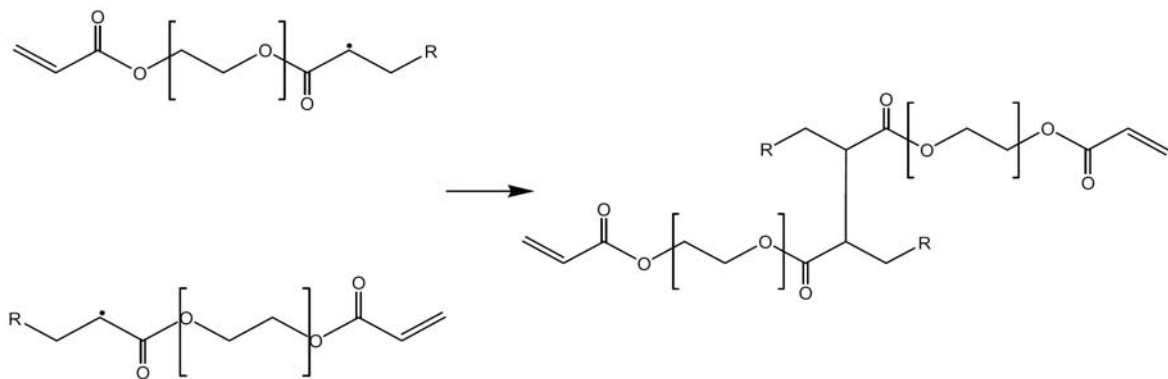


Figure 5.15: The double bond of the acrylic groups are attacked likewise by radicals at the gold dots: Those double bonds polymerize into the hydrogel. Afterwards, we peel off the glass, the gold dots were transferred into the hydrogel.

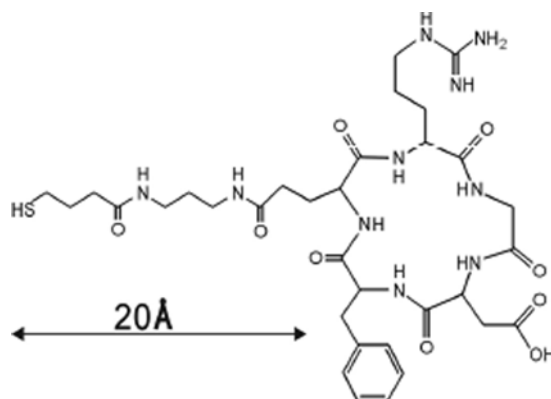


Figure 5.16: Cyclic RGD peptide (cRGDfK) presenting a thiol-group (SH) which binds to the gold nanoparticles and an alkane spacer to facilitate access to the peptide by integrin receptors.

Each gold particle is bio-functionalized by binding the cyclic peptide, using the affinity of the thiol group for gold (Fig. 5.16).

5.3 Analytics

Several different analytical techniques have been used i.e. scanning electron microscopy (SEM), atomic force microscopy (AFM), cryo scanning electron microscopy. In this section, these tools will be described in detail.

5.3.1 Detector nanopatterned surfaces

The Scanning Electron Microscope (SEM) is a microscope that uses electrons rather than light to form an image. It produces images of high resolution (10 nm) and only requires the sample to be electrically conductive. To visualize the gold nanoparticles on the surface, an acceleration voltage of 3kV is applied under a pressure of 5×10^{-6} mBar. The magnification is times 150000.

Measurements with a Nanoscope III Atomic Force Microscope (Digital Instruments) were performed at ambient conditions. Topographic images are acquired in a tapping mode using silicon tips on integral cantilevers with a nominal spring constant of 30-67 N/m. In tapping mode, the cantilever (Nanosensors) is excited near its resonance frequency with a piezoelectric driver, and the oscillation amplitude is used as a feedback signal to measure the topographic variations of the sample.

5.3.2 Cryo SEM observation of nanostructured surfaces

In life sciences, fluorescence microscopy and confocal microscopy are the main techniques used for imaging cell structure. Since the PEG gel is transparent, it is not possible to obtain a sensitive image of its structure using the low resolution microscopy. X-ray and high resolution microscopy which require high electron dose, can damage delicate specimens. Fortunately, Cryo-SEM has been successfully employed for observing biomaterials, proteins and cell membranes. Here we use Cryo-SEM to investigate PEG gel surface.

5.4 Materials and Methods

5.4.1 Nanopatterned glass substrate preparation

The modification of silicon wafers or borosilicate glass substrates was performed using standard protocols for surface modifications. In brief, substrates were cleaned in “piranha” solution consisting of a 3:1 ratio of 30% w/v aqueous solutions of H_2SO_4 and H_2O_2 (*caution:*

this mixture reacts violently with organic materials and must be handled with extreme care), washed with H₂O, and dried under nitrogen.

Glass nanopatterned surfaces were prepared according to a procedure reported by Arnold *et al.* The PS-P2VP diblock copolymers form in micelles in toluene in which the PVP forms the core, and the PS forms the shell, and after interaction of the P2VP with H₂AuCl₄, loaded micelles are formed. Glass coverslips were immersed into a toluene solution containing micelles of copolymers and loaded with gold (H₂AuCl₄, Sigma) nanoparticles. The velocity of dipping was approximately 12 mm/min. The polymer shell was removed by treating the coverslips with hydrogen gas plasma (Te-Pla 100-E, Feldkirchen, Germany) for 45 min at 180 Watt and 0.4 mBar, which furthermore caused the reduction of the metal core. An array of gold nanoparticles organized in hexagonal patterns on the dipped part of the coverslip was thus generated.

5.4.2 Polymer preparation

In the following section, three methods employed to transfer nanostructures from glass coverslips to polyethylene glycol (PEG) hydrogels will be described. PEGn moleculars of three different molecular weights were used: (M_w=575kDa, M_w= 700kDa, M_w=800kDa).

5.4.2.1 PEG (M_w=800kDa)

Functionalization of nanopatterned surface with thiol linker

Nanopatterned glass coverslips were placed in a dessicator. After evacuation, the dessicator was connected to a Schlenck flask containing cysteamin. The valve of the dessicator was opened and cysteamin vapor allowed into the dessicator for 1 h. The substrates were subsequently washed with dichloroethane. 171 μl (1 mmol) of diisopropylethyl-amine (DIEA) and 81 μl (1mmol) of acryloylchloride were dissolved in 30 ml of anhydrous dichloroethane. The samples were immersed in the solution for 2 h while shaking them and subsequently washed thoroughly with dichloroethane and dried.

Polymer preparation

460 of water were placed in a Schlenck flask and degassed by evacuating the flask for 1/2h and filling it with N₂. Afterwards 600 mg of PEG (M_w=800kDa) were added. In all the following steps exposure to light was prevented by covering the flasks with Aluminium foil.

A spatula tip of initiator, 4-(2-Hydroxyethoxy) phenyl-(2-propyl)ketone, were dissolved in degassed water (1ml) and stirred for 1/2h under N₂. The initiator solution (40μl) was then added to the polymer solution and left under stirring 5min.

Solubility of the initiator: 7.6g/L of initiator at 25°C

Required amount of initiator: 0.05% W/W

Transfer of nanostructures to the PEG hydrogels

A nanopatterned glass coverslip was placed face upon a sample holder and glued with a small amount of water. One drop of polymer solution was put in the middle of the sample and immediately covered by a coverslide. The hydrogel was exposed to 366 nm, 300 mW/cm² UV light for 30 min. The reaction was performed in a N₂ atmosphere.

Removal of the nano-structured cover slides by 10% hydrofluoric acid:

After transfer of the gold nanopattern from the glass coverslip to the PEG hydrogel, the glass was removed using hydrofluoric acid. The gel between the coverslide and the glass with nano-structured glass was set on a Petri dish covered with glass-sand-yielded. Drops of hydrofluoric acid (10% solution in water) were deposited at the bottom of the Petri dish in contact with the nanopatterned glass coverslide. The hydrofluoric acid was changed every hour until no glass residues were observed.

5.4.2.2 PEG (Mw=700kDa)

Functionalization of nanopatterns with thiol linker

Nanopatterned glass coverslips were placed in a dessicator. After evacuation, the dessicator was connected to a Schlenck flask containing propene thiol. The valve of the dessicator was opened and cysteamine vapor allowed into the dessicator for 1 h. The excess of unreacted thiol was removed by blowing the samples with N₂.

Contaminated equipment was washed with a solution of H₂O₂ (30% in water) to remove thiol residues..

Polymer preparation

2mL of PEG (Mw=700kDa) were placed in a Schlenck flask and degassed by evacuating the flask for 1/2h and filling it with N₂. In all the following steps exposure to light was prevented by covering the flasks with aluminium foil.

A spatula tip of initiators 4-(2-Hydroxyethoxy) phenyl-(2-propyl)ketone was dissolved in degassed water (1ml) and stirred for 1/2h under N₂. The initiator solution (130µl) was then added to the polymer solution and the mixture was left under stirring 5min.

5.4.2.3 PEG (Mw= 575kDa)

Functionalization nanopatterned surface with thiol linker

Nanopatterned glass coverslips were placed in a dessicator. After evacuating, the dessicator was connected to a Schlenck flask containing propene thiol. The valve of the dessicator was opened and Cysteamin vapors let in the dessicator for 1 h. The excess of unreacted thiol was removed by blowing the samples with N₂.

Contaminated equipment was washed with a solution of H₂O₂ (30% in water).

Polymers preparation

2mL of PEG (Mw=575kDa) were placed in a Schlenck flask and degassed by evacuating the flask for 1/2h and filling it with N₂. In all the following steps exposure to light was prevented by covering the flasks with aluminium foil.

20 mg of initiator, 2, 2-dimethoxy-2-phenyl acetophenone (DMPA) were dissolved in degassed water (1mL) and stir for 1/2h under N₂. The initiator solution mixed with the polymeric solution.

Transfer of the nanopattern from glass coverslip to PEG

The glass coverslips were placed in the holder and placed in a polymerization chamber under a N₂ stream as shown in figure 5.17. A few drops of polymer-initiator (PEG 700 or PEG 575) mixture were placed on the modified gold nano-structured glass slide and a glass coverslip was positioned on top of each sample. The samples were exposed to a 366 nm 300 mW/cm² for 1/2h. After peeling off, the PEG hydrogels were stored in water (Fig. 5.17). Hydrogels having the same pattern of the nano-structure glass coverslip were prepared by linking alkanethiol onto gold dots.

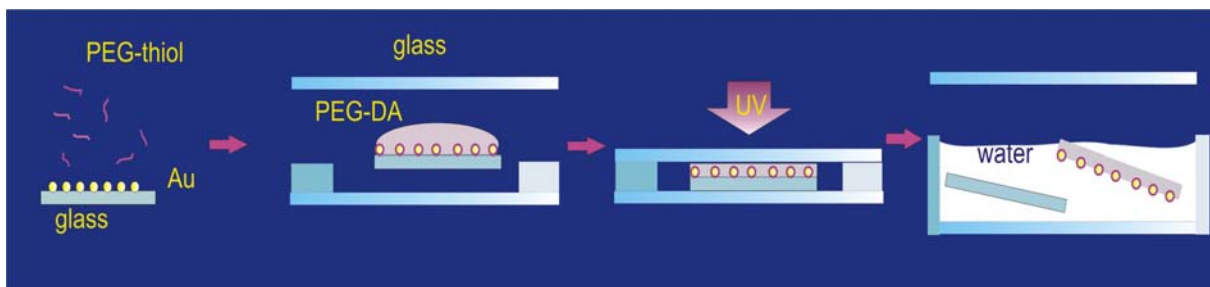


Figure 5.17: Preparation of nanostructured hydrogel

5.4.3 Sterilization of hydrogel

After exposure under UV light for 5 mins, hydrogels were transferred to Petri dishes (avoiding contact with the gold surface). The nanopatterned hydrogels were first sterilized with 2ml 70% ethanol for 10 min and then rinsed with MQ water 2 times 30 min each time. To determine the swelling rate the diameters of the hydrogels were determined and compared to the diameters measured before washing with water. After sterilization, 25 μ l aqueous of a cyclic-RGD peptide (c-RGDfK-thiol) were planed onto hydrogel, which was immediately wrapped on Parafilm in size of the hydrogel for 45min. The Parafilm was removed by rinsing with MQ water. The hydrogels were subsequently washed in 2ml MQ water (4 times 10 min each time), PBS (10 min), warm medium (37 °C, 10 min). The nanostructures biofunctionalized with cyclic-RGD peptides are ready for studying cell function.

5.5 Results and discussion

5.5.1 Nanostructures on the glass surface

In order to produce nanostructures, it is necessary to control the nano-object position and fabrication on the surfaces. Whipping and milling, called top-down approach are very thermodynamically unstable. An alternative route to effectively control and design structure formation is the bottom-up approach. The essence of bottom up structuring is to focus on the control of relevant interaction (hydrophobic, van der Waals, electrostatic interactions, Brownian forces etc.) on a molecular and colloidal level, leading to self-assembled structure¹⁴⁵. Thin diblock copolymer and polymer blend films have been proposed as a powerful approach for the formation of lithographic mask. Recently, some research groups have demonstrated that the size of topographic nanoscale features (e.g. grooves or holes) on a surface can affect the adhesion and phenotype of cells adhesion to that surface. Self-assembled monolayers of metallic nanocrystals self-assembled on a solid substrate have been used to produce single surface-anchored nanocrystals which can bind with molecules. However, such nanocrystals can be removed by washing. Some workers have tried to produce stable nanocrystals by annealing at 250°C for 24h under 30KV/cm¹⁴⁶ or using one-step lithography surface-bound ferrocenylsilane chemistry. However, in the later case, the important element iron may also influence the cell. The protocols of patterning approach used in the present work are based on self-assembly of diblock copolymer micelles. Due to nanocrystals can be removed during washing steps¹⁴⁷, the micelles films were exposed under isotropic hydrogen plasma to get stable surface and single nano cluster. The topography of the nanopatterned surfaces is examined by AFM and SEM (Fig. 5.18 and 5.19). After the assembly of micelles containing gold

nanoparticles, the polymer is entirely removed by a gas plasma treatment, which results in extended and highly regular arrays of gold nanodots, deposited into a nearly perfect hexagonal pattern on glass. Cores of micelles are annealed to single gold nanocrystal during this process^{148, 149}.

Figure 5.18 shows scanning electron microscopy (SEM) images of patterns of gold nanodots (bright spots). The micrograph of nanopatterns shows the hexagonal distribution. The distances between gold nanodots are varied by using diblock copolymers of different molecular weight. The average size of the gold nanodots is 8 nm.

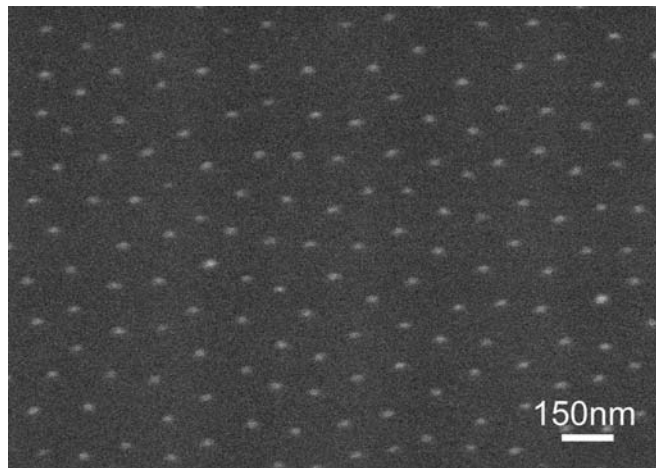


Figure 5.18: SEM images of nanopatterned surfaces showing hexagonal arrays of gold nanodots deposited at variable distances depending on the molecular weight of the diblock copolymer used.

The topography of the nanopatterned surfaces, can be examined using AFM. The peaks corresponding to the profile of gold nanodots deposited on the surface are on average 6 nm high.

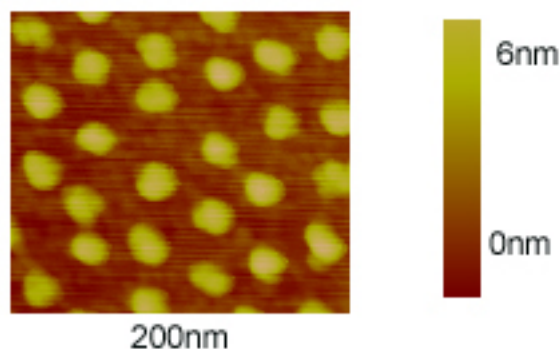


Figure 5.19: AFM image of nanostructures on glass.

5.5.2 Micro and nanostructures on the hydrogel

Observing nanostructure under Cryo-SEM is not easy. To confirm that the transfer process could work, we transfer gold microstructures that had been produced using method to hydrogel.

The microstructures are shown in figure 5.20.

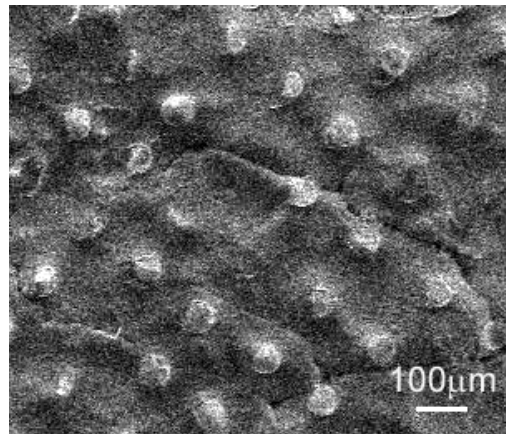


Figure 5.20: Cryo SEM image of microstructure hydrogel surface

To characterize the topography of the nanopatterned surfaces, surface roughness is examined by AFM. Figure 5.21 shows a nanopatterned hydrogel surface after being transferred from a glass. In fact, the peaks corresponding to the profile of gold nanodots deposited on the surface are on average 6 nm high.

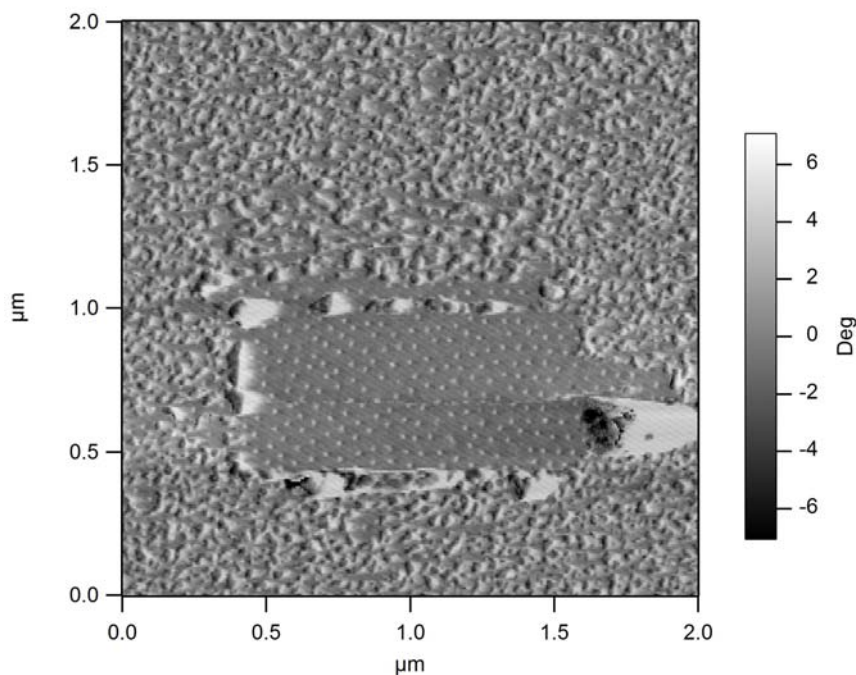


Figure 5.21: AFM image of hexagonally distributed gold nano dots on hydrogel surface. This figure is kindly provided by Stefan Gräter and Julia Schölermann (Group of Prof. J. Spatz, Max-Planck-Institut Für Metallforschung, Stuttgart).

We use a thiol linker transfer to the the gold dots to the PEG gel. The particles form an extended hexagonal pattern of Au-nanoparticles on hydrogel showing the same arrangement as the nanopatterns on the glass slide (Fig. 5.21). Further improvement in the preparation of hydrogel leads to the possibility of nanostructures transferring without losing the hexagonal

order. The gold nanoclusters are distributed in a hexagonal pattern which is coming from the micelles regular tessellation structure on glass substrate. During the polymer swelling, the swelling rate is 1.5 ± 0.2 . Figure 5.19 and Figure 5.21 show that nanopatterned hydrogel surfaces after transferring from glass. The peaks corresponding to the profile of gold nanodots (bright spots) deposited on the surface are the same on the glass and on the hydrogel. After polymerization, PEG can be easily peeled off from the glass without leaving residues.

5.6 Conclusion

There are two steps in this method: firstly, we produce nanostructures on a solid substrate. Secondly, we employ a thiol linker method to transfer gold dots to PEG.

In conclusion we have reported a successful method to transfer nano pattern from a solid support to a soft material. This method provides a nano mask to control position and connect molecular (e.g. RGD) on the polymer surfaces.

In summary, we have developed a new lithographic method, employing micellar monofilms containing a metal precursor, to transfer nanostructures to soft materials. These gold particles were located exclusively in areas that have been exposed to plasma. The size and spacing of pattern on the hydrogel is controlled by the patterning on the original solid substrates. We have employed the nanostructured hydrogel as a template for cell adhesion, demonstrating the applications of micellar nano- and soft lithography techniques in a biological contact. For example, this method provides a way to study the interaction of cells and substrate deformation.

Chapter 6

Cell adhesion on Nanostructured hydrogel

6.1 Introduction

How do cells grow on tissue-like substrates? In vivo, there are specific molecules, e.g. integrin ligands, that assist cell attachment. We aim to study cell behaviour on the quantitative biochemical factors and tissue-like substrate. It is necessary to find out an accurate system for controlling integrin-integrin lateral spacing essential for receptor cluster formation and cell adhesion on soft material.

Several methods have been described over the past 10 years for patterning surfaces with immobilized ligands or proteins. A recent theme in patterning has been the development of methods that can control the positions of ligands at a sub-micron resolution. Cells can react to sub-micrometer features, ranging between 50 and 500 nm, by changing their adhesion, morphology and gene expression¹⁵⁰. Nanoarray of pits of interal size in the range of 100 nm, arranged in well ordered orthogonal and hexagonal patterns, has been also shown to affect cell responses¹⁵¹. Since cell-environment interactions involve recognition of nanoscale features, our group has developed a patterning strategy based on the self-organization of diblock copolymer micelles and transferred the resulting gold nanostructures to a PEG hydrogel surface. This method provides a nano mask to enabling the PEG surface to be patterned with individual molecules in a controlled manner.

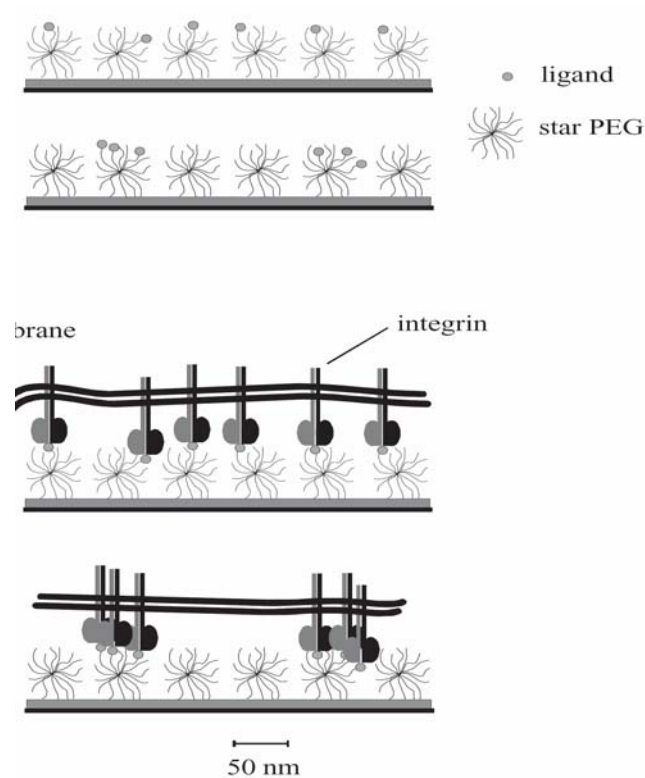


Figure 6.1: The distribution of RGD peptide was controlled by using YGRGD peptides linked to star PEO molecules to produce PEG hydrogel-modified coverslips¹⁵⁴.

Poly (ethylene glycol) (PEG) is a nondegradable, hydrophobic polymer. Due to its high biocompatibility and its low toxicity PEGs are widely used as biocompatible materials in medicinal areas. The question of how cells react to soft, RGD-functionalized surfaces has been investigated by several groups. For instance, peptides were linked to the activated N-6 via N-terminus with polyacrylamide¹⁵². Moreover, RGD peptides that are linked to the star PEO molecules have been used to control the distribution of RGD peptide on PEG hydrogel-modified coverslips¹⁵³. With all these previous methods, the distribution of RGD on the surface was difficult to control, and limited.

How to control accurate positioning of ligand molecules? In a previous work, the glass substrate with Au dots distances, such as 28 nm and 58 nm, have been successfully used for cell adhesion observation (Fig. 6.2). In literature, the methods which were studied on the polymer surface provided rather high densities of RGD substrates for cell adhesion.

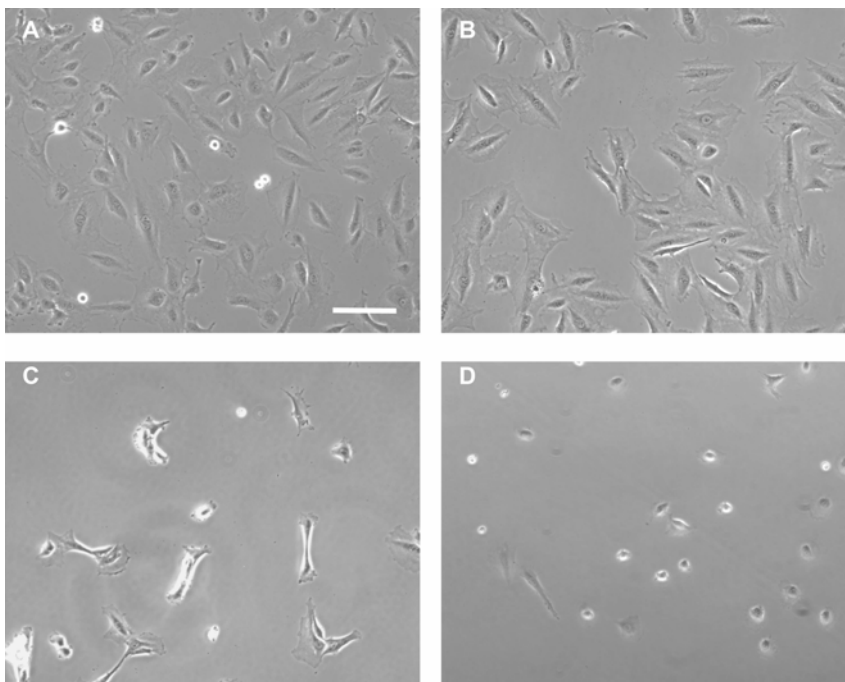


Figure 6.2: Cell adhesion on nanopatterned surfaces with different spacing of adhesive nanodots. A, the spacing between dots is 58nm; B and C, the spacing between dots is 73nm; D, the spacing between dots is 109nm. Scale bar 100 μm ¹⁵⁴

Currently, we employ a thiol linker to transfer gold dots to the PEG gel. We found out that ordered solid nanopatterns can thus be transferred from a solid to a soft material surface. Functionalization of the Au dots with C(RDGfK)-thiols allows cell adhesion and behaviour on hydrogels to be studied. We study cell adhesion on Au dots with spacings of e.g. 39 nm, 79 nm and 100 nm. We investigate whether there is a different behavior between cell behaviour on glass nanostructured surface and soft nanostructured surfaces.

6.2 Materials and Methods

6.2.1 General methods for cell culture

To avoid contamination, all the steps involving cells are performed in a sterile hood, using sterile techniques and materials. Cells are cultured at 37 °C and 5% CO₂ atmosphere in an incubator. The medium is changed every 2 days.

After the cells have reached confluence, they are first rinsed with sterile PBS and then released with a trypsin-EDTA 2.5% (Gibco) solution for 3-5 min. After diluting in 5-10 ml of complete medium and centrifugation at 1200 rpm for 5 min, the cell pellet is suspended in medium and cells are then replated in cell culture flasks or in wells containing the substrates prepared for the adhesion studies.

6.2.2 Cell counting

To determine the number of cells and the number of vital cells in culture, cell suspension in DMEM is diluted 1:10 in a 0.05% Trypan blue (Sigma) solution in MQ-water. This colored substance can enter and stain only dead cells. The cell suspension in Trypan blue is then transferred into two hemocytometer chambers. By using a 10x objective and light microscopy, it is possible to visualize the grid lines in the chamber, having each field an area of 1 mm². Then the cells are counted in 8 fields and the average number of cells per volume (ml) is calculated (excluding cells stained in blue which are dead).

6.2.3 Observation under Phase contrast microscopy

Phase contrast microscopy is used to produce high-contrast images of transparent specimens such as living cells. Its optical mechanism is based on the translation of small variations in phase into corresponding changes in amplitude, which can then be visualized. The variations in phase are produced by the slight difference of the refractive index between the cell culture medium and the cell or in the cell between the cytoplasm and the nucleus. Phase contrast images were acquired with a Axiovert 40 CFL microscope (Zeiss, Göttingen, Germany) with an A-Plan 10x/0.25 Ph1 or 20x/0.45 Ph2 objective (Zeiss). Images were acquired with an AxioCam MR camera and the software MrGrab (Zeiss).

6.3 Results

6.3.1 Cell attachment and spreading on PEG gel

Cells plated on modified PEG gel surfaces were evaluated daily for up to 3 days.

Figure 6.3 shows light microscope images of cells cultured for 3 days on PEG gel. Only half of the glass substrate area is patterned with gold nanodots with different spacing between the dots. The gold nanodots are functionalized by RGD peptides. Where as no cell were observed on the bare PEG gel. A homogeneous almost confluent lawn of cells covered the RGD bound membrane (Fig 6.3 A, left side and Fig 6.3 B). When membranes are coated with homogeneous gold (Fig. 6.3 B) good adhesion is observed. The right side of figure 6.3 A show that there is no cell growing on the PEG gel side having no nanostructure and RGD bound.

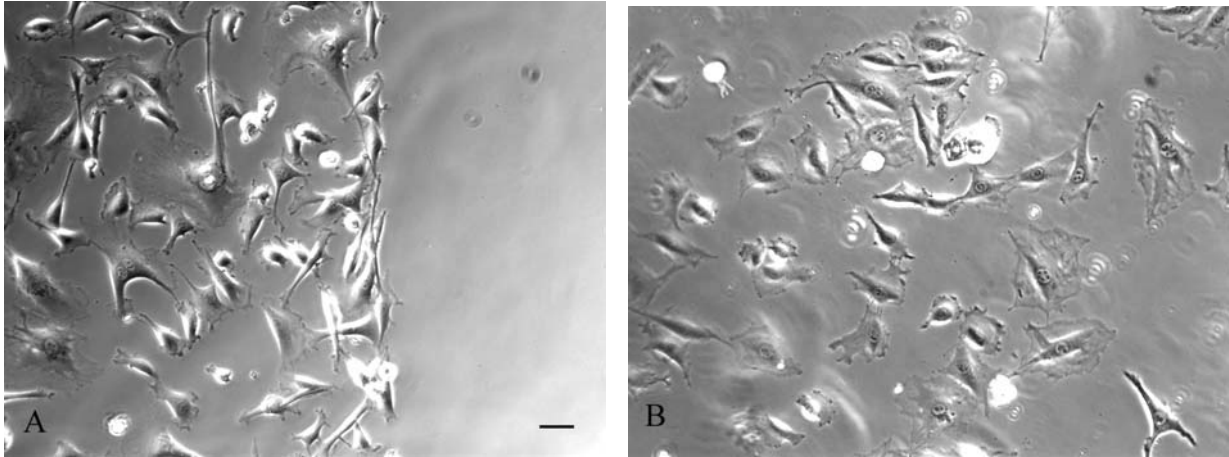


Figure 6.3: A. Cells adhere to the RGD nanostructured surface, but not to the bare PEG gel. No nanostructures are located on the right side of the images. B. Cell spreading well after 24h on a PEG gel whose surface has been covered with a homogenous gold film that more than functionalized with RGD. Scale bar 50 μm .

6.3.2 The distance between RGD-nanodots modulates cell adhesion on PEG gel.

We have investigated whether the presence of RGD-ligands bound to nanodots placed with different spacings (39, 79 and 100 nm) on the surfaces effects cell adhesion on hydrogels. Cells were seeded on nanopatterned hydrogel and examined after one day by phase contrast microscopy (Fig. 6.3). Half of the glass substrate area was patterned with gold nanodots with different spacing between the dots. The gold nanodots were functionalized with RGD peptides. The other part of the substrate was only PEG gel. A distance of 39 nm between gold nanoparticles on nanopatterned surfaces was sufficient to support cell adhesion and spreading, but cells could not adhere to the substrates where the spaces were 79 nm and 100 nm (Fig. 6.4).

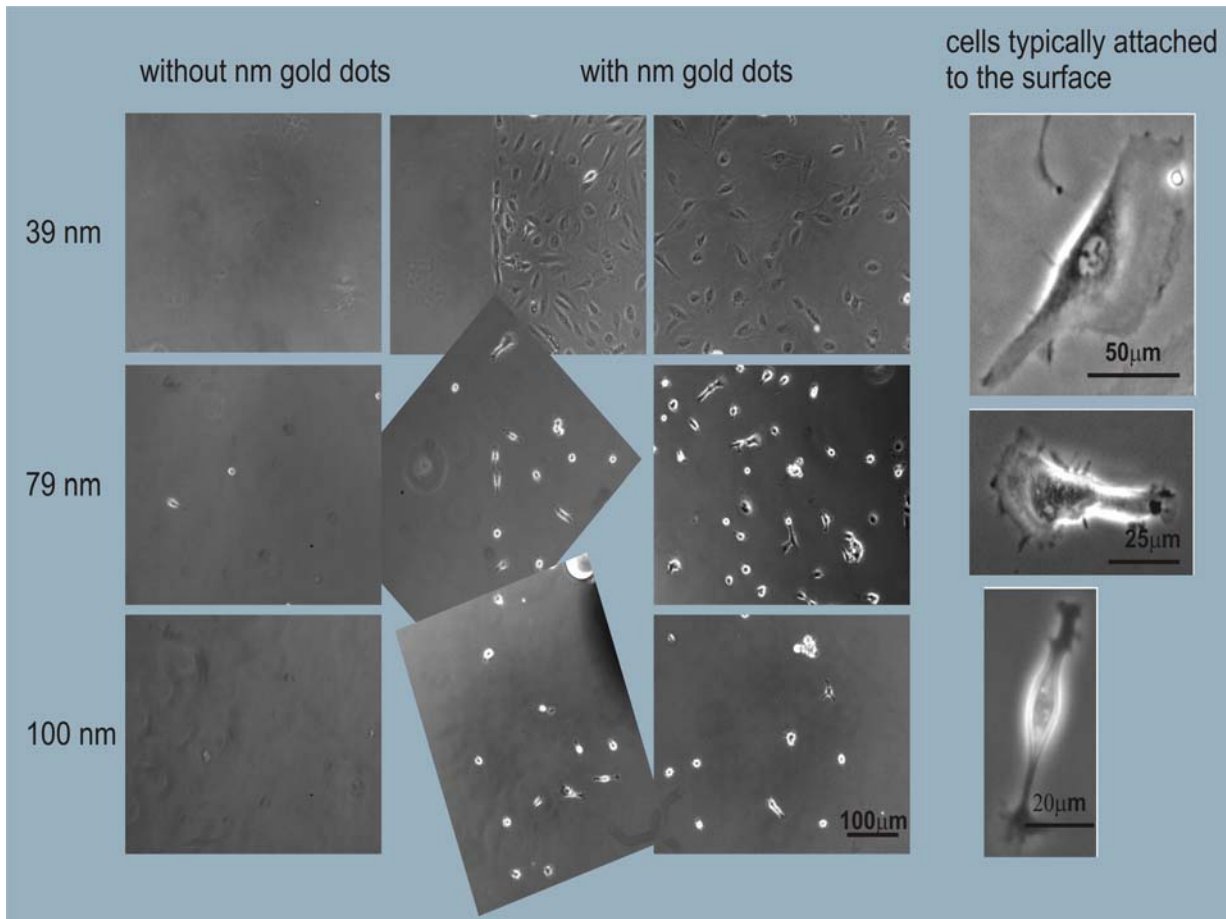


Figure 6.4: Cell spreading on different distances of dot-dot hydrogel. No nanostructures are located on the left side of the images. High magnification images of cells are shown on the right side of the figure.

This figure is kindly provided by Stefan Gräter (Department of Biophysical Chemistry, Group of Prof. J. Spatz, University of Heidelberg).

6.4 Discussion

We found that cells do not adhere to PEG gel in the absence of gold nano dots, when the gel was immersed in RGD solution for a long time. PEG has several characteristics, such as, highly hydrophobic and optical transparency. PEG can be absorbed on an oxidized surface, that exhibit notable resistance against the non-specific adsorption of proteins from solution. In our system, PEG does not affect cell binding. The reason could be that the inter-dot PEG is not arranged in a brush-like order. Therefore, we avoid the problem of endogenously secreted ligands between cells and substrate.

The solid nanopatterns have been successfully transferred to soft materials surface. The C(RGDfK)-thiols with Au dots have been employed to study cell adhesion on hydrogels. The use of RGD peptides attached via thiol groups to gold dots provided specific bonds which were linked with integrin. By varying the spacing between gold nanoparticles, functionalized with

RGD peptides, we can identify the critical distance between integrin ligands to promote cell adhesion and spreading on PEG gel. In Maheshwari's paper, a YGRGD peptide was attached to the PEG hydrogel using star PEO tether. This approach allows the average surface density and local (scale of approx. 50 nm) spatial distribution of RGD peptide to be controlled independently¹⁶⁰. However, the distance of stars is fixed after polymerization. In order to modify the RGD density, the arms of star PEO tether linked with RGD in random. It is difficult to accurately control the distance between each RGD.

Why do we study cell adhesion on nanostructured surface with a dot-dot distance starting from 28 nm? In literature, Danilov and Juliano estimate a characteristic peptide-to-peptide spacing required for full attachment of 22 nm¹⁵⁵. Singer et al. used a similar system that the minimal spacing requirement was estimate to be 16nm¹⁵⁶. These RGD surface concentration values are in excess of that obtained. The diameter of integrin in the cell membrane is between 8-12 nm. The peptide ligand can be conjugated to all sides of other proteins of cell in these short distances, so some fraction of ligand is shielded from the cell. Brandley and Schnaar addressed the issue of the minimal ligand density (A peptide-to-peptide spacing is 76 nm) by covalently incorporating an RGD-containing peptide into a polyacrylamide gel¹⁵⁷. This idea is close to our studying, but the quantitation of ligand concentration actually at the polyacrylamide is quite difficult to control. Typical integrin expression is in the order of 100,000 receptors / cell¹⁵⁸. This yield a receptor density of approx. 1000 integrins / μm^2 for spread cells. The cell area was measured at approx 1500 μm^2 . A range of average ligand densities 1,000-200,000 ligands/ μm^2 was examined in Maheshwari's experiment. In our present studied, we try to find out the maximal distance for cell adhesion. In order to do so, we study cell adhesion on nanostructured surface with a dot-dot distance starting from 28 nm. We count the number of separated dots on 28 nm separated dots nano structured surfaces. The total number of dots is 1100 dots / μm^2 . Every gold dot is considered to be linked with a RGD molecular. Cell can grow well in this substrate. Our data is consistent with Maheshwari's result in lowest RGD density.

To compare with literature, we chose 28, 58 and 73 nm dot-dot distance for sample's preparation. The gold nanoclusters distribute in hexagonal shape. During substrate swelling, this structure is kept stable. The distances of golddots were 39, 79 and 109 nm, for 28, 58 and 73 nm respectively, after hydrogel swelling. The total number of dots when we separate them at regular distance of 28, 58, 73 and 85 nm is 1100, 280, 190 and 100 dot/ μm^2 , respectively. If we compare an arbitrary in figure 6.5, the total numbers of dots in 39, 79 and 100 nm separated dots nanostructure are 680, 66 and 56 dots/ μm^2 , respectively. In literature, the methods

provided rather high densities RGD substrates for cell adhesion (about 10 to 200-fold bigger than the approximate receptor density). There is few available data showing cell behaviour on this low RGD density hydrogel. Maheshwari reported that the lowest homogeneous RGD density is correspond to 270 RGD molecular/ μm^2 . Our present work is an extension of Maheshwari's experimental set up. We can observe cell adhesion under a low RGD density which can be controlled by di-block polymer micelles and polymer swelling.

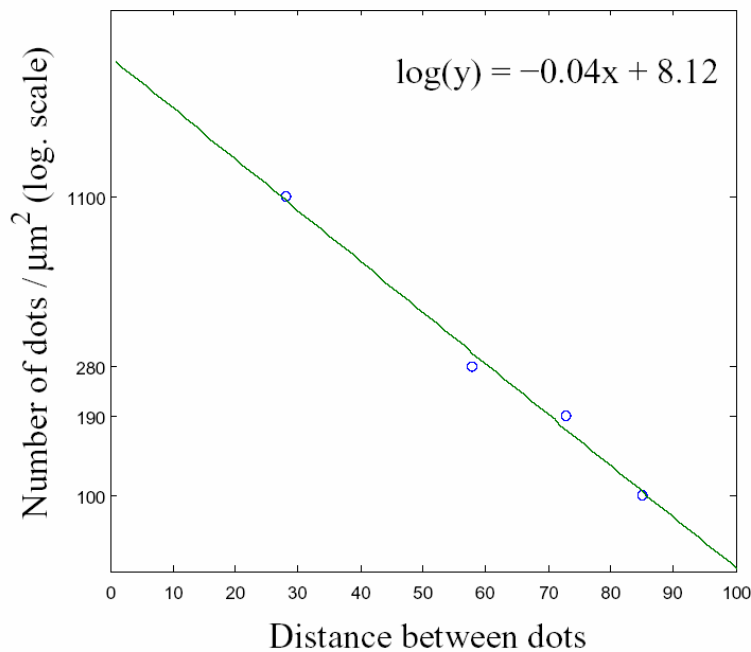


Figure 6.5: Scaling factor for the density of dots in nanostructured surface.

In our previous studies, the cell attachment, growth and differentiation were investigated under different distances. Those on the 28 and 58 nm nanopattern could form stress fibers and assemble focal adhesions, while cells on the 73 and 85 nm nanopattern failed to do it. The increase in dot separation above 58 nm causes a decrease in the number of dots. There is a linear relationship between dots density and dot-dot distance. Therefore, the observed limitation of cell adhesion at increased dot separation could be reasoned due to either the lower number of gold dots covered with RGD peptides, or to the increased local dot-to-dot distance. Modulation of peptide distance is expected to dramatically influence cellular adhesion behaviour. In present result, the distances between dot-dot are 39, 79 and 100 nm. The cells grow well on substrates with a dot distance of 39 nm. The increase in dot separation causes a decrease in the number of dots, cell can not adhere on the 79 nm and 100 nm separated dot substrates. The soft and glass

nanostructured surfaces follow the same trend in the relationship between cell adhesion and dots distance.

This approach has revealed that the distance of RGD strongly controls the cell adhesion and that large distances of RGD were ineffective in cell adhesion. Several studies simulated the effect of ligand surface distributions and cell adhesion. Darrell used a Monte Carlo simulation of equilibrium model and a two-dimensional (for the description of the substrate interface). They anticipate that the ligand binding energy is not affected by nearest-neighbour interactions between the receptors^{159, 160}. Our experiments can exactly explain this phenomenon without using any simulations.

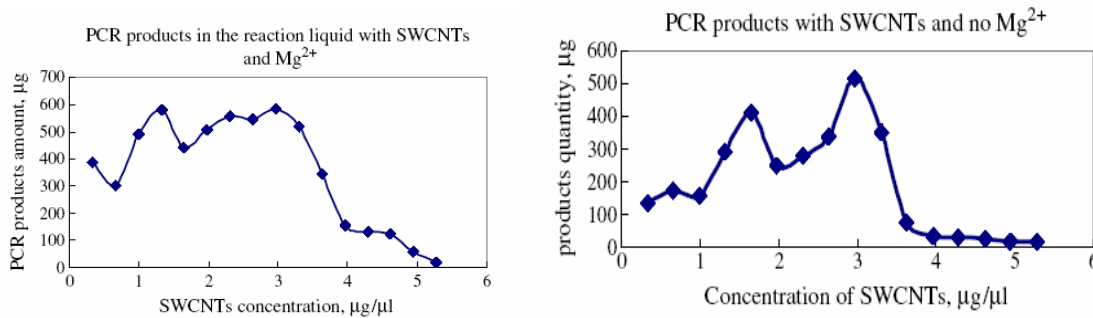
What is the molecular mechanism in which cell senses and responds to soft substrates? If it is possible to find the relationship between gene expression and softness substrate, it will provide important clue of regulation mechanism of gene-expression. In future, we will focus on observing some cell adhesion related proteins, cell survival and apoptosis on this kind of soft materials.

Zusammenfassung

Die biologischen Anwendungen von neuen Nanomaterialien hat großes Interesse erzeugt. Kohlenstoffnanoröhrchen (CNT) wurden in den letzten Jahren auf Grund ihrer einzigartigen Eigenschaften in Bezug auf molekulare Elektronik und Biosensoren intensiv untersucht. Nanostrukturen werden in verschiedenen Gebieten wie der Physik, der physikalischen Chemie, der Materialwissenschaften sowie der Chemo- und der Elektrotechnik benutzt. Nanostrukturierte Oberflächen können verwendet werden, um eine kleine Zahl chemischer Einheiten zu verwalten/kontrollieren und Zelladhäsion auf molekularer Ebene zu untersuchen. Das Ziel dieser Arbeit war es die Mechanismen der Wechselwirkungen zwischen Nanomaterialien und Zellen zu untersuchen. Zwei unterschiedliche Nanomaterialien wurden in dieser Arbeit verwendet: einwandige Kohlenstoffnanoröhren (engl. Single wall carbon nanotube, SWCNT) und nanostrukturierte Hydrogele. In Kapitel 1 wird eine allgemeine Einleitung über das wissenschaftliche Anwendungsfeld von Nanomaterialien wie SWCNTs und nanostrukturierten Hydrogelen gegeben.

Es ist von großem Interesse, Methoden zur Effizienzsteigerung der Polymerase-Kettenreaktion (engl. polymerase chain reaction, PCR) zu erforschen. In Kapitel 2 wird der Einfluß von SWCNT`s auf die PCR durch quantitative Bestimmung der PCR-Produkte mit Hilfe von Rasterelektronenmikroskopie (SEM), hochauflösender Transmissionselektronen mikroskopie (HRTEM) und Röntgen-Photoelektronenspektroskopie (XPS) untersucht.

Die Messungen zeigen, daß die Zugabe von SWCNTs bei einer Konzentration von weniger als 3 µg/µl zur Reaktionslösung zu einer Zunahme der PCR- Produkte führt, während höhere Konzentrationen zu einem umgekehrten Effekt führen.



Die PCR hat ein Maximum bei eine SWCNT Konzentration von 3 µg/µl.

Ähnliche Ergebnisse wurden bei Zugabe von Mg²⁺-Additiven zur PCR-Reaktion erhalten. Sowohl SEM- als auch HRTEM-Messungen zeigen, daß die DNA-Template und Taq-Enzyme an SWCNT-Bündel in den PCR-Produkten gebunden sind.

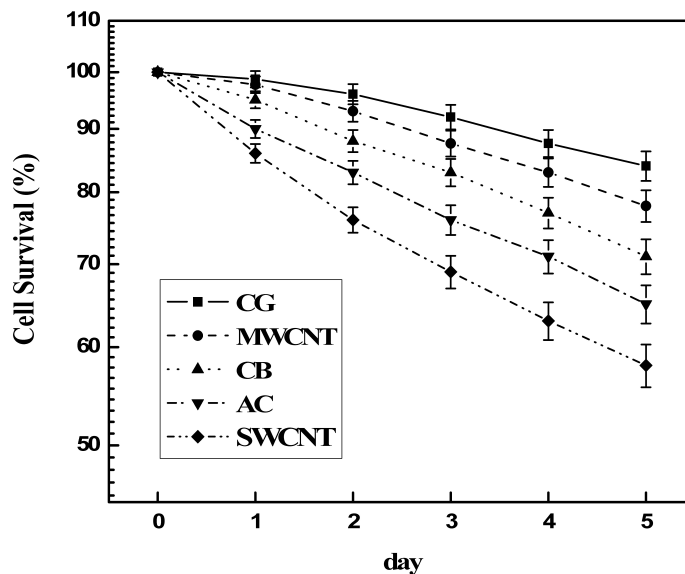
Vergleicht man die XPS-Spektren der Kohlenstoffnanoröhren von vor der Reaktion mit denen nach der Reaktion, so weisen die PCR-Produkte eine höhere C1s-Bindungsenergie auf, wie das Auftreten zweier neuer Signale neben dem Hauptpeak zeigt. Dies weist auf eine chemische Reaktion zwischen SWCNTs und PCR-Komponenten hin.

Letztendlich können folglich SWCNTs in einem Konzentrationsbereich von unter 3 µg/µl in der Reaktionslösung die PCR-Effizienz erhöhen und haben das Potential in vielfältigen biochemischen Reaktionen als Katalysatoren zu dienen.

Materialien, ähnlich den Nanotubes, werden heute täglich zu hunderten Kilogramm produziert, was zum Aufkommen gesundheitlicher Bedenken führt. Bezüglich Nanopartikel gibt es viele Unsicherheiten um Gesundheit, Sicherheit und Umwelt. Die Toxizität, Epidemiologie, Persistenz und Bioakkumulation von Nanopartikeln muss weiter erforscht werden. Die Effekte von carbon nanotubes auf Zellen und ihre Interaktionsmechanismen zu untersuchen ist daher sehr wichtig. In Kapitel 3 ist eine systematische Studie an menschlichen Fibroblasten in der Gegenwart von aufgereinigten CNTs verschiedener Geometrien und Größen dargestellt. Die Ergebnisse werden mit denen anderer Kohlenstoffmaterialien verglichen. Insbesondere wurde das Überleben der Zellen in Anwesenheit von fünf verschiedenen

Kohlenstoffmaterialien untersucht. In der Reihenfolge zunehmender Ordnung sind dies: i) SWCNT, ii) Aktivkohle, iii) Kohlenstoff Schwarzes, iv) mehrwandige Kohlenstoffnanoröhren und v) Graphit.

Interessanterweise wurde dabei eine starke Abhängigkeit des Zelltods von der Größe, Zeit und Dosis der Kohlenstoffverbindungen festgestellt.



Einfluß von SWCNT auf die Überlebensrate von menschlichen Fibroblasten.

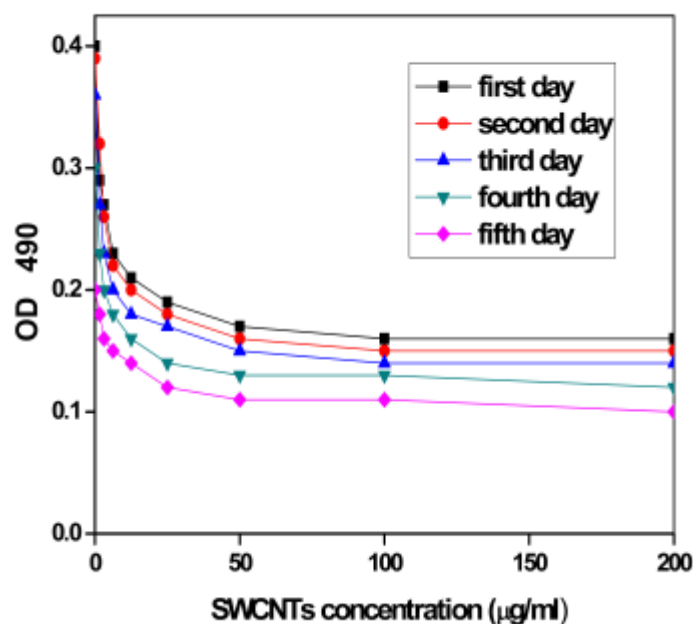
Des weiteren konnte gezeigt werden, daß bereits Konzentrationen ($25\mu\text{g/ml}$) unter den in der Literatur dargestellten Werten zum Tod der Zellen führen können.

Da Kohlenstoffverbindungen störend auf die Zellmembran wirken und deshalb zur Zellablösung vom Substrat führen können, wurde der Expression von Zellzyklus Adhäsion zusammenhängenden Proteine, wie Laminin, Collagen-IV, Fibronectin, P-Cadherin und focal adhesion Kinase gemessen.

Zuletzt wird ein biologischer Mechanismus dargestellt, der erklärt warum kleinere Partikel, wie z.B. SWCNT, einen größeren Einfluß haben.

In Kapitel 4 wird der Einfluß der SWCNTs auf menschliche HEK293-Zellen untersucht, um Aufschluss über die Biokompatibilität der SWCNTs zu gewinnen.

Die Ergebnisse zeigen, daß SWCNTs die HEK293-Zellproliferation inhibieren können, sowie die Adhäsionseigenschaften der Zellen abhängig von Zeit und Dosis schwächen.



Der Einfluß von SWCNT auf die Lebensfähigkeit von HEK293 Zellen.

HEK293-Zellen zeigen aktive Reaktionen auf SWCNTs, wie die Absonderung verschiedener 20-30 kD schwerer Proteine welche dann die SWCNTs umgeben, als auch die Aggregation von SWCNTs und die Bildung von knotenförmige Strukturen.

Zellzyklus- Untersuchungen zeigten, dass eine Konzentration an SWCNTs von 25µg/ml im Zellmedium bei HEK293-Zellen einen G1 Arrest sowie Apoptose hervorrufen.

Biochip Analysen zeigten, dass SWCNTs Hochregulation der Expression von Zellzyklus assoziierten Genen wie *p16*, *bax*, *p57*, *hrk*, *cdc42* und *cdc37* sowie Herabregulation der Expression von Zellzyklus assoziierten Genen wie *cdk2*, *cdk4*, *cdk6* und *Cyclin D3* bzw. Herabregulation der Expression von an der Signaltransduktion beteiligter Gene wie *mad2*, *jak1*, *ttk*, *pcdha9* und *erk* bewirken können.

Western blot Analysen zeigten, dass SWCNTs eine verminderte Produktion von mit der Zelladhäsion zusammenhängenden Proteinen wie Laminin, Fibronectin, Cadherin, FAK und Kollagen IV bewirken können.

Diese Ergebnisse legen nahe, dass Herabregulierung von G1 assoziierten Cdk's und Cyclinen sowie Heraufregulation von Apoptose assoziierten Genen zu dem von SWCNTs induzierten G1-Phasen-Arrest beitragen. Andererseits können HEK293 Zellen auch aktiv Antworten anschalten, dazu zählt das Ausscheiden von kleinen Proteinen, um die an SWCNT attachierten Zellen von der restlichen Zellmasse zu isolieren. Dieses Phänomen hat potentielle Anwendbarkeit in medizinischer Chemie und Therapie von Krankheiten. Die ausgeschiedenen Proteine sind vielleicht wertvolle Targetmoleküle.

Unsere Ergebnisse können deshalb zukünftige Untersuchungen und die Risikoeinschätzung von SWCNT Einwirkung leiten. Wir bestätigen daher dass die Größe von Kohlenstoffmaterialien ein wichtiger Faktor ist. Da die Nanotechnologie sich anschickt, in großem Maßstab genutzt zu werden, sollten die Gesundheits- und Sicherheitsaspekte von SWCNTs baldigst angegangen werden. Wir denken, dass weitere Cytotoxizitätsstudien darauf abzielen sollten, Grenzwertdosen von SWCNTs verschiedener Größe zu finden. In Zukunft können wir diese Studie verfeinern, indem wir den Durchmesser von carbon nanotubes z.B. via Nanolithographie kontrollieren.

Die Ligandenichte spielt eine wichtige Rolle bei der Zelladhäsion. Allerdings waren bislang Informationen über die strukturelle Anordnung der Liganden nicht zugänglich, da keine Methoden zur Verfügung standen, biofunktionelle Oberflächen mit hoher räumlicher Auflösung

zu strukturieren. Spatz entwickelte Oberflächen die eine regelmäßige Strukturierung von Goldpartikeln im Nanometerbereich aufweisen⁹¹. Diese Technik wurde erfolgreich bei der

Untersuchung von Zelladhäsion angewendet. Die Ligandendichte kann durch diese nanostrukturierten Oberflächen gesteuert werden. Das Ziel dieser Arbeit ist es die Zellreaktion im Hinblick auf zwei Faktoren zu untersuchen: den Einfluß der Elastizität des Substrates sowie die nanostrukturierte Oberfläche des Substrates auf das Zellverhalten. Das primäre Ziel der vorliegenden Arbeit lag in das sich Entwickeln eine Methode für das Studieren von Zellenadhäsion auf Hydrogel. In Kapitel 5 wird eine neue lithographische Methode entwickelt, die sich eines Thiol Ankers bedient, um Nanostrukturen auf weiche Materialien zu übertagen. Diese Mizellen werden homogen auf flachen Substraten, wie Glasdeckgläschen. In einem darauf folgenden Plasma-Prozess werden alle organischen Bestandteile mittels Wasserstoff, Sauerstoff oder Argon entfernt und die monodispersen Au Nanoteilchen erzeugt, deren Größe durch die Menge des zugefügten Ausgangsmaterials bestimmt wird. Der Abstand der Nanoteilchen zueinander wird durch das Molekulargewicht des verwendeten Polymers bestimmt. Die Au Nanopartikel bedecken die Oberfläche homogen in einer quasi-hexagonalen Anordnung. Es werden dabei hexagonal geordnete Muster von Gold- Nanopartikeln großflächig auf Glasplättchen erzeugt und unter Beibehaltung der ursprünglichen Ordnung auf Hydrogele transferiert. Das Muster aus Goldpunkten stellt eine Nano- Maske dar, die es ermöglicht, auf der Polymer- Oberfläche an kontrolliert geordneten Positionen Moleküle anzubinden. Die nanostrukturierten Hydrogele werden als Substrate für Zelladhäsionsversuche verwendet, womit die Anwendbarkeit der mizellären Nano- und Soft- Lithographie in diversen Forschungsbereichen gezeigt wird. Unter anderem ermöglicht dieses Verfahren zum Beispiel auf Grund der mechanischen Eigenschaften der generierten Substrate zu erforschen, wie bzw. inwieweit Zellen deformierbare Substrate wahrnehmen und darauf reagieren.

Vorhergehende Studien zeigten, daß Zellenzubehör vom Goldnano-Punktabstand abhing. Daher bestand das zweite Ziel der Arbeit darin, die Rolle der räumlichen Anordnung auf Hydrogel. Die Zellenadhäsion ist auf dem nanostructured hydrogel nachgeforscht worden, das gesteuert werden kann durch Di-blockieren Polymer-Plastik Micelle und Polymer-Plastik Swelling. Dazu wurden REF 52 auf Oberflächen ausplatiert, die eine hochgeordnete

Nanostrukturierung von 8nm Goldpartikeln im Abstand von 39, 79 und 100 nm aufwies. Der Raum zwischen den Gold-Nanopartikeln war durch Polyethylenglykol (PEG). Ein zyklisches RGD-Peptid wurde kovalent über eine Thiolgruppe an das Gold gebunden. Jeder Goldpunkt selbst ist so klein, dass nur ein einziger Integrin-Rezeptor anbinden kann. Bis zu einem Abstand von 39nm zwischen den RGD-Peptiden konnte eine gute Ausbreitung und Adhäsion der Zellen. Eine Erhöhung des Goldpunkteabstandes auf über 79nm hatte eine Verringerung der Zellkontakte und eine eingeschränkte Zellausbreitung zur Folge. Dieses hat gezeigt, daß der Abstand von RGD eine wichtige Rolle bei der Zelladhäsion spielt. Das gleiche Verhältnis zwischen Zellenverhalten und Goldpunktstand wurde bei Zellen auf weichen nanostrukturierten Oberflächen beobachtet.

Um den molekularen Mechanismus bei welchem die Zelle ein weiches Substrat spürt und auf es reagiert, zu untersuchen, ist es notwendig das Verhältnis zwischen der Genexpression und Weichheit des Substrates zu untersuchen. Dies wird einen Hinweis auf den Regulierungsmechanismus der Genexpression liefern. Es wäre interessant sich auf einige Proteine die mit Zelladhäsion in Beziehung stehen sowie Zellproliferation und Apoptosis zu konzentrieren.

Appendix A

Characterization of BRCAA1 and Its Novel Antigen Epitope Identification

Abstract

Looking for novel breast cancer antigen epitopes is helpful for its treatment, diagnosis, and prevention. Brca1 gene is mapped at 1q42.1-q43, its whole genome is 93.857 kb, including 18 exons and 17 introns. BRCAA1 protein is composed of 1,214 amino acids with 10 glycosylate sites, and shares 37% amino acid identity and an identical antigen epitope with Rb binding protein 1. The novel antigen epitope, SSKKQKRSHK, was predicted to locate in the region 610 to 619 sites, was synthesized, and its antibody was fabricated. Competent inhibition analysis showed that SSKKQKRSHK is the shortest effective peptide. The antigen epitope was mapped in the cytoplasm of MCF-7 cells. Immunohistochemistry analysis showed that the antigen epitope exhibited positive expression in 65% (39 of 60) breast cancer specimens and negative expression in 60 noncancerous tissues. Statistical analysis shows that its expression is closely associated with status of ER and PR, with sensitivity of 100% and specificity of 81%, and confidence interval of 85.9% to 96.9%. ELISA analysis showed that the mean absorbance of sera antibody titers from breast cancer patients and healthy donors were 0.401 ± 0.163 SD and 0.137 ± 0.121 SD, respectively. Sixty-four percent breast cancer patient sera and 13% healthy donor sera had higher titer than mean titer of healthy donors, and there exists significant difference between breast cancer patients and healthy donors ($P < 0.001$). In this study, a novel breast cancer antigen epitope, SSKKQKRSHK, is identified. Its expression is associated with characteristics that are themselves associated with prognosis of breast cancer, and its sera antibody level may be helpful for breast cancer diagnosis.

Introduction

Breast cancer is a common tumor among women. In the United States, for example, one in every eight women will develop breast cancer in life¹⁶¹. Despite the advances in treating breast cancer, the causal mechanisms underlying this disease have yet to be fully elucidated. Eighty-five

Breast cancer is a common tumor among women. In the United States, for example, one in every eight women will develop breast cancer in life¹⁶¹. Despite the advances in treating breast cancer, the causal mechanisms underlying this disease have yet to be fully elucidated. Eighty-five percent of breast cancer cases occur sporadically without any known genetic mutation¹⁶². Therefore, looking for its antigen epitopes and fabricating corresponding antibodies is a central objective in developing its specific immunologic diagnosis and immunotherapies. Breast cancer associated antigens can elicit both antibody and cellular immune responses that are active and specific. Therefore, these human antibodies, specific for breast cancer, can be used as probes for the molecular identification of associated breast cancer antigens or genes¹⁶³, in favor of its treatment, diagnosis, and prevention.

So far, some useful biomarkers associated with breast cancer have been recognized. For example, HER-2 predicts prognosis of breast cancer and may influence treatment responses.¹⁶⁴ Ras expression has been suggested as a marker for tumor aggressiveness of breast cancer, including the degrees of invasion and tumor recurrence.¹⁶⁵ γ -Synuclein (SNCG), also referred to as breast cancer-specific gene 1, is highly expressed in human-infiltrating breast carcinomas but not expressed in normal or benign breast tissues. The expression of SNCG was strongly correlated to the stage of breast cancer.¹⁶⁶ MUC1 and Met-HGF/SF can be detected in the axillary fluids of patients with breast cancer. The expression of both markers in the axillary drainage is strongly associated with unfavorable tumor features and can be used as a prognostic factor^{167,168}. Ki67 antigen is expressed by proliferating cells in the late G1, S, and G2-M phases of the cell cycle. Its expression in breast cancer samples correlates with mitotic activity, recurrence rates after mastectomy, and survival¹⁶⁹. Nuclear matrix protein (NMP) is detected in the blood of women at the early stage of breast cancer, which is absent in the blood of healthy women. NMP66 has been selected as a marker for further developments and clinical trials of a test to be used in the detection and monitoring of women with, or at risk of, breast cancer¹⁷⁰. These tumor markers, such as estrogen receptor (ER), progesterone receptor (PR), p53, and cyclin D1, are also most useful for monitoring response to therapy and detecting early relapse of breast cancer¹⁷¹.

Here we reported the characterization of a novel breast cancer associated antigen BRCAA1 and investigation of its novel antigen epitope and clinical significance. The *brcaa1* gene, a breast cancer associated antigen 1 gene (GenBank no. AF208045), was cloned in 1999. So far in GenBank, there are some homology sequences, such as NM_031371, AF214114, NM_053421, AF083249, AL133418, etc. For example, RBP1L1 gene, a gene similar to *brcaa1*, exhibited up-regulated expression in breast cancer, lung carcinoma, colon cancer, ovary carcinoma and testis,

chromosomal location of *brca1* was investigated by fluorescence *in situ* hybridization, and its genomic and protein structure characterization was analyzed. According to antigenic index (AI), a novel breast cancer antigen epitope was predicted and confirmed by a series of experiments, and its clinical significance was further investigated.

Materials and methods

PCR primers and short peptides. A pair of PCR primers, with introduction of a COOH-terminal His-tag, was chemically synthesized. The sequences were as follows: primer-C1: 5'-CTT TAA GAA GGA GAT ATA CCA TGA GAG TGA AAG ATG CTC AG-3', primer-C2: 5'-TGA TGA TGA GAA CCC CCC CCA CTC CAT TTG TAA ACT TTG G-3'. Short peptide SSKKQKRSHK, SKKQKRSHK, and SSKKQKRSH with keyhole limpet hemocyanin (KLH) were chemically synthesized.

Selection criteria of breast cancer patients and healthy donors and sample resource. The criteria for the sporadic patients were: primary invasive breast carcinoma less than 5 cm, no axillary metastases, age at diagnosis less than 55 years, and no previous malignancies. The criteria for hereditary patients were: carriers of a germline mutation in *BRCA1* or *BRCA2*, and primary invasive breast carcinoma. ER and PR expressions were determined by immunohistochemical staining. The criteria for healthy donors were: women without hereditary diseases, malignancies, cardiac vascular diseases and haematological diseases; age ranging from 28 to 55 years. Sixty pairs of primary breast cancer specimens and non-cancerous breast specimens were collected from patients with breast cancer. Sixty specimens of breast cancer sera were collected from same patients with breast cancer before operation and treatment. Thirty specimens of normal sera were taken from a randomly selected set of healthy female donors. All collected sera were kept in -20°C refrigeration. All these specimens were collected from 1996 to 1999 in Xijing Hospital, China. These breast cancer cases were diagnosed by the Department of Pathology of Xijing Hospital. Tumors and non-cancerous tissues were preserved in liquid nitrogen within 30 minutes after surgery. Non-cancerous tissues were picked up at 5 cm distance away from primary breast cancer sites. Formalin-fixed, paraffin-embedded tumor tissues and lymph nodes were used to evaluate the tumor type, histologic grade, and the presence of metastasis and extensive lymphocytic infiltrate. The data are shown in Table A.1. Our study was approved by administration of scientific research of Fourth Military Medical University

Table A.1: Breast cancer samples classification

Sample no	Age	Grade	ERp	PRp	Brcal or Brca2 mutation	Metastasis	Lymphocytic infiltrate	Detecting results*
1	43	2	80	80	0	0	0	+
2	44	1	50	50	0	0	0	+
3	41	3	10	5	0	0	0	-
4	41	3	50	70	0	0	1	+
5	48	3	100	80	0	0	0	+
6	49	2	80	80	0	0	0	+
7	46	1	80	50	0	0	0	+
8	48	3	0	0	0	0	0	-
9	48	3	60	80	0	0	1	+
10	38	2	100	10	0	0	0	+
11	37	3	90	70	0	0	0	+
12	46	3	0	0	0	0	0	-
13	41	3	10	5	0	0	1	-
14	48	1	100	80	0	0	0	+
15	46	3	30	10	0	0	0	-
16	49	3	50	50	0	0	0	+
17	48	2	90	90	0	0	0	+
18	32	1	40	90	0	0	0	+
19	48	1	80	30	0	0	0	+
20	34	3	0	0	0	1	1	-
21	39	1	50	50	0	0	0	+
22	45	2	60	80	0	1	1	+
23	41	2	70	70	0	0	0	+
24	49	3	0	0	0	0	0	-
25	45	2	100	100	0	0	0	+
26	40	3	100	40	0	0	0	-
27	45	1	80	90	0	0	0	+
28	40	3	100	0	0	0	0	-
29	52	2	100	80	0	0	0	+
30	54	2	100	40	0	0	0	-
31	52	2	80	90	0	0	0	+
32	54	2	100	0	0	0	0	-
33	52	2	100	80	0	0	0	+
34	54	3	100	40	0	0	0	-
35	54	3	90	10	0	0	0	+
36	52	3	0	0	0	0	0	+
37	54	2	70	30	0	0	0	+
38	52	2	100	100	0	0	0	-
39	46	2	50	50	0	0	0	+
40	53	3	70	10	0	0	0	+
41	54	3	100	0	0	0	0	-
42	54	3	50	40	0	0	0	+
43	54	3	50	5	0	0	0	-
44	53	1	0	0	0	0	0	+
45	37	2	100	60	0	0	0	+
46	44	3	50	100	0	0	0	-
47	43	3	90	5	0	0	0	+
48	30	3	0	0	2	1	1	+
49	39	2	80	100	0	0	0	+
50	39	3	100	0	0	0	0	-
51	41	3	80	80	1	0	0	+
52	45	3	50	50	0	1	1	+
53	28	3	0	0	0	0	0	-
54	43	3	90	90	0	0	0	+
55	41	2	100	100	0	0	0	+
56	30	2	70	20	0	0	0	-
57	28	3	0	0	01	1	1	-
58	38	3	70	90	0	0	0	+
59	44	3	50	0	2	0	0	-
60	45	3	70	70	0	0	0	+

*Detection of expression of novel antigen epitope in breast cancer tissues by immunohistochemistry.

Mapping of brca1 on human chromosome by fluorescence in situ hybridization.

Chromosome slides were made using peripheral blood lymphocytes (PBL) and stained with G strip according to standard methods.¹⁷⁵ brca1 fragments (5.3 kb) were labeled with fluorescence dye according to the manual of the labeling reagent kit. Chromosome slides were prehybridized overnight, and then hybridized with denatured probes for 24 hours. The slides were subsequently washed twice in solutions of 2xSSC + 0.2% SDS, 0.1 x SSC + 0.2% SDS, and 0.1xSSC, 10 minutes each time, then dried at room temperature, observed under fluorescence microscope, and photographed for mapping analysis¹⁷⁶. According to hybridization results and searching against Human Genomic Resource, the brca1's concrete position on human chromosome was determined.

Characterization of genomic structure and protein structure. In accordance with brca1 gene sequence, its exons and introns were identified by searching against Human Genomic Resource, and its amino acids sequence was derived. Its hydrophilicity, surface probability, flexibility, antigen index, secondary structure, and glycosyl site were analyzed by using GCG software (Genetics Computer Group, Madison, WI)¹⁷⁷.

Expression of short peptide A via rapid translation system. DNA fragment matching with 600 to 700 amino acid sites in Fig. 3 was selected. A pair of primers with introduction of a COOH-terminal His-tag, primer-C1 and primer-C2, was designed and chemically synthesized. PCR reaction 1 was used to obtain specific fragments: 10x PCR buffer 3 μ L, 2.5 mmol/L deoxynucleotide triphosphate 3 μ L, primer-C1 1 μ L, primer-C2 1 μ L, brca1 vector template 2 μ L, 25 mmol/L MgCl₂ 3 μ L, and Taq enzyme 1 μ L. Sterilized minipure water was added until the total volume was up to 30 μ L. PCR reaction condition: predenature at 94 °C for 4 minutes, then 94 °C for 1 minute, 55 °C for 1 minute, 72 °C for 1 minute, 25 cycles, finally extended at 72 °C for 7 minutes. The PCR product was purified with a PCR purification kit. PCR reaction 2 was used to obtain the products with regulatory elements and His-tag by using rapid translation system (RTS) E. coli Linear Template Generation Set and His-tag kit (Roche Diagnostics GmbH, Penzberg, Germany). The PCR products were purified by PCR purification kit. The purified products were used for expressing corresponding proteins by RTS 100 E. coli kit (Roche Diagnostics)¹⁷⁸. The protein products were rapidly purified using Vivapure S Spin column. The expressed protein, named as short peptide A, was confirmed by Western blotting using anti-His antibody as first antibody.

Rabbit IgG antibody against the peptide SSKKQKRSHK

A rabbit antibody against SSKKQKRSHK was developed. Five hundred micrograms of SSKKQKRSHK were mixed with Freund's complete adjuvant and injected around the lymph nodes of two rabbits. Twenty days later, the rabbits received an i.m. injection of 250 µg of SSKKQKRSHK in Freund's incomplete adjuvant, followed by three immunizations with the same dose every 20 days. Ten days later, the rabbits were bled, sera were collected, and serum IgG antibody titers were tested for SSKKQKRSHK using ELISA. The anti-SSKKQKRSHK IgG antibody was purified from the serum using an affinity column with the synthetic peptide.

Labeling of rabbit IgG antibody and determination of antigen epitope specificity.

Rabbit IgG antibody was purified after the precipitation by standard affinity chromatography on protein G-Sepharose 4 Fast Flow. Coupling of purified antibody to peroxidase was made in accordance with the method of Nakane and recommendations of Boehringer Mannheim Biochemica (Mannheim, Germany)¹⁷⁹. For a determination of epitope specificity, a 96-well plate was coated with peptide A (1 µg/mL) in 100 AL of 0.1 mol/L sodium bicarbonate buffer (pH 9.6). Nonspecific binding sites of the wells were then blocked with a solution of 1% bovine serum albumin in PBS for 1 hour at 37 °C. After washing with PBS containing 0.1% Tween 20 (PBS-T), 100 µL of rabbit IgG antibody were added and incubated for 1 hour at 37 °C. Then, the plate was washed 5 times with PBS-T and 100 AL of a 5,000-fold diluted solution of goat antirabbit IgG antibody labeled with peroxidase were added to each well. After incubation for 1 hour at room temperature and washing with PBS-T, 100 µL of the mixture of o-phenylenediamine (0.43 mg/mL in 0.1 mol/L citrate buffer, pH 5.0) and H₂O₂ (0.002%) were added in each well. Then, the mixture was incubated for 30 minutes at room temperature in darkness. The reaction was stopped by adding 50 µL of 1 mol/L HCl. The absorbance of the product was measured at 490 nm using Bio-Rad 680 Microplate Reader.

Screening and purification of positive sera to bind peptide A. Purified peptide A in 5 Ag/mL PBS solution was coated onto 96-well polystyrene plates and incubated overnight at 4 °C. The wells were then incubated with blocking buffer for 2 hours. One hundred microliters of 1:500 diluted individual human sera were added in triplicate to the peptide A-coated plates and incubated for 2 hours at room temperature. Controls included 1:500 diluted individual human sera plus the second antibody added to the wells without peptide A. The remaining steps followed standard ELISA procedure. A specific absorbance was obtained by subtracting background absorbance from experimental absorbance. Sixty sera from breast cancer patients and 30 sera from healthy women were screened for their antibody reactivity to expressed peptide A. The positive sera from breast cancer patients were measured the titer of IgG antibody to peptide A by ELISA. The immunoglobulin fraction of those positive sera was precipitated by 40% saturation ammonium sulfate, resuspended in PBS (pH 7.4), and dialyzed at

4 °C against PBS. The IgG was purified by passing through a protein G column. The bound IgG was eluted with 0.3 mol/L acid glycine buffer (pH 3.0), neutralized with 1 mol/L Tris (pH 8.0), and dialyzed against PBS¹⁸⁰.

Immunoprecipitation and western blotting analysis.

All steps of the immunoprecipitation were carried out on ice. MCF-7 cells were lysed in an NP40 isotonic lysis buffer with freshly added protease inhibitors (142.5 mmol/L KCl, 5 mmol/L MgCl₂, 10 mmol/L HEPES (pH 7.2), 1 mmol/L EGTA, 0.2% NP40, 0.2 mmol/L phenylmethylsulfonyl fluoride, 0.1% aprotinin, 0.7% µg/mL pepstatin, and 1 µg/mL leupeptin) by shaking for 30 minutes. Nuclei and unlysed cellular debris were removed by centrifugation at 15,000xg for 10 minutes. Purified human IgG antibody and anti-SSKKQKRSHK antibody were added for 90 minutes, and immunoprecipitates were captured with 10% (v/v) protein G-Sepharose for 60 minutes. Immunoprecipitates were washed 3 times in lysis buffer. Immunoprecipitates were solubilized with SDS-PAGE sample buffer and electrophoresed through 15% SDS-polyacrylamide gels. For Western blotting, proteins were electrotransferred during 1 hour (400 mA) on polyvinylidene difluoride membranes. Filters were blocked for 2 hours with PBS-T containing 5% nonfat milk. All immunostaining steps were done in PBS-T at room temperature. Filters were incubated with human IgG antibody or anti-SSKKQKRSHK IgG antibody for 2 hours, respectively. After washing, secondary antibodies labeled with peroxidase were added for 2 hours. Then filters were washed in PBST and developed by the enhanced chemiluminescence system¹⁸¹.

ELISA competition inhibition assays with synthetic peptide antigens. For ELISA competition inhibition assays, 100 µL of human antibody in 5 µg/mL PBS were added to 96-well polystyrene plates, incubated overnight at 4 °C, and then blocked with 1% bovine serum albumin. Specific IgG antibody (1.7×10^9 mol/L) was incubated overnight at 4 °C with peptides SSKKQKRSHK, SKKQKRSHK, and SSKKQKRSH at concentrations of 1.7×10^{-9} , 1.7×10^{-8} , 1.7×10^{-7} , 1.7×10^{-6} , 1.7×10^{-5} and 1.7×10^{-4} mol/L. Pre- and post-inhibited antibodies were then added in triplicate to peptide-coated plates and incubated for 3 hours at room temperature. Peroxidase-conjugated goat anti-human IgG was added for 1 hour at room temperature, followed by the addition of o-phenylenediamine dihydrochloride peroxide substrate solution. Reactivity was measured by absorbance at 490 nm.

Immunohistochemical analysis with human specific antibody. Sixty pairs of breast cancer specimens and non-cancerous tissues were analyzed by immunohistochemistry. The avidin-biotin complex (ABC) technique was used for immunohistochemical staining of these

temperature for 1 hour. Alkaline phosphatase substrate was then added for color development. The slides were counterstained with H&E¹⁸².

Statistical analysis. Paired and unpaired t test and X^2 analysis were used to explore the correlation of the expression of novel antigen epitope and sera antibody levels with patient ages, breast cancer stages, ERp, and PRp. Values of $p \leq 0.05$ were considered to be statistically significant. The model based on the threshold on ERp and PRp was established to explain the data, and was obtained after applying dimensionality reduction with a stepwise forward selection, using X^2 to rank the worth of each variable with respect to the outcome. The final predictor was chosen in the form of classification trees, with informational loss function¹⁸³. A logistic regression with stepwise forward selection¹⁸⁴ was found to be less accurate than a classification tree. Neither PCA dimensionality reduction nor Bayesian modeling (in which ERp and PRp were assumed Gaussian distributions) did not show any clear advantage compared with classification trees. All statistical analyses were done with statistical Package for the social science software (SPSS, Chicago, IL), and S-plus language.

Results

Human Chromosomal Location. Fluorescence *in situ* hybridization result showed that *brca1* was mapped at 1q42.1-q43 as shown in Figure A.1. Searching against Human Genome Resource, NT_004836.14/Hs1_4993 clone on human No. 1 chromosome was found to include the whole *brca1* cDNA sequence. Further analysis showed that the cDNA of *brca1* is located between 167428 and 73571 sites, that is, 1q42.1-q43. Therefore, *brca1* is confirmed to locate 1q42.1-q43. Final result was submitted to GenBank (AF208045).

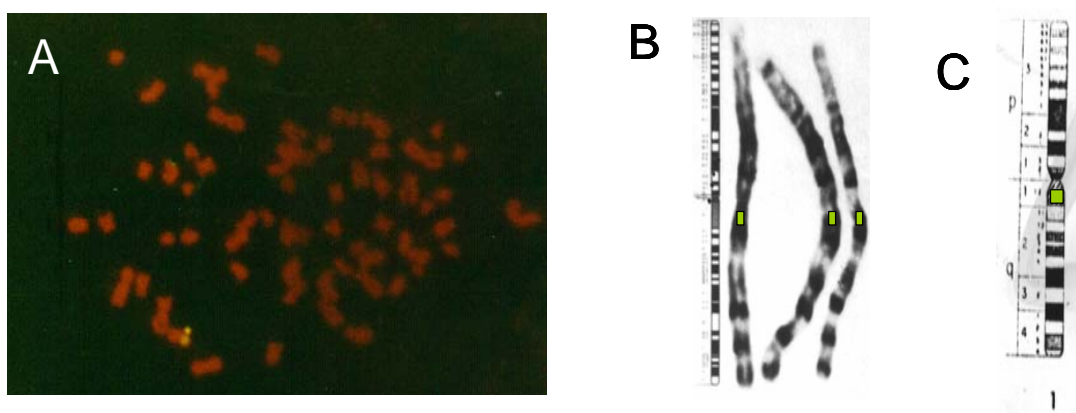


Figure A.1: Human chromosome location of *brca1* by fluorescence in situ hybridization. A. Fluorescence in situ hybridization map; B and C. Concrete location of *brca1* gene on No. 1 chromosome with G band, Schematic of concrete location of *brca1* on No. 1 chromosome with G band.

Characterization of genomic structure and protein structure. Searching against Genome resource, the region of 167428 to 73571 nucleotide sites in NT_004836.14/Hs1_4993 clone was found to include the full-length cDNA sequence of brca1. The region of 167428 to 73571 nucleotide sites in NT_004836.14/ Hs1_4993 is genomic region of brca1. The whole length of this region is 93.857 kb, including 18 exons and 17 introns, as shown in Figure B.2.

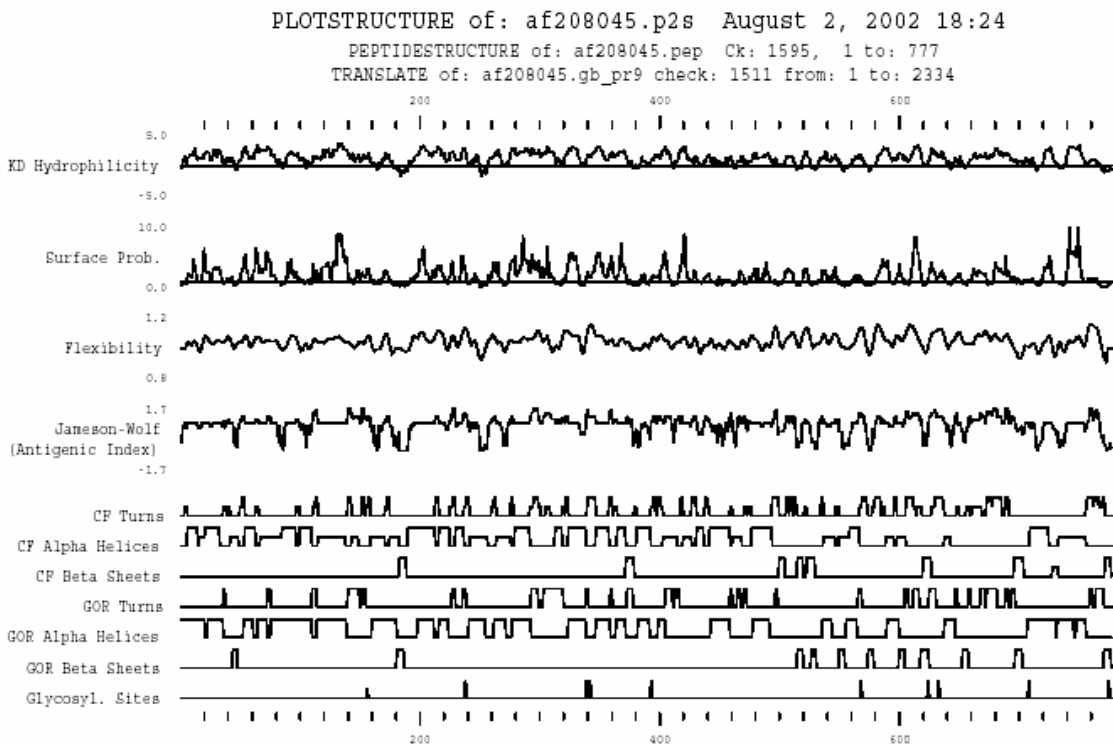


Figure B.2: Plotstructure graph of BRCAA1 protein created by the PLOTSTRUCTURE command of GCG software.

Compared with GenBank Database, BRCAA1 protein has 37% amino acid identity compared with RB binding protein1. BRCAA1 protein includes two known antigen epitopes, such as KASIFLK (sites 250 to 256, RBP1) and IKPSLGSKK (sites 34 to 42, BRCAA1, Fig. A.2). Its peptide is predicted to include 10 glycosylate sites. The region 740 to 750 at NH2 terminus is very hydrophilic, indicating that this region may be exposed to solvent, and it may form a helix. Its probability, flexibility, AI, and secondary structure are shown in Figure A.3.

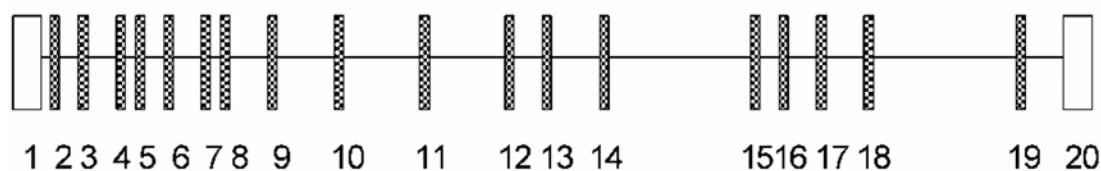


Figure A.3: Schematic of genomic structure of brca1. Black column, exon; short line between black columns, intron; white column, 5V and 3V untranslated regions.

In the region 580 to 620 sites, the AI values are higher than average; therefore, potential antigen epitope likely exists in this region. Especially in the region 610 to 619 sites, SSKKQKRSHK, their AI values are the highest, suggesting that the peptide SSKKQKRSHK possibly is a potential antigen epitope.

Expression and confirmation of peptide A by using RTS and Western blotting. Western blotting result, as shown in Figure B.4, shows that peptide A, composed of 100 amino acids (600 to 700 sites, Figure A.2), including predicated antigen epitope with His-tag, was successfully expressed by RTS.

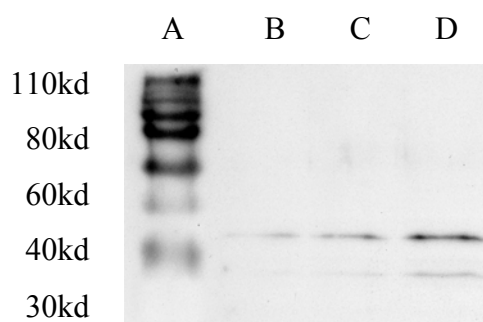


Figure A.4: Western blotting analysis of peptide A by using antihis antibody as first antibody. A. Protein marker; B-D, hybridization bands of peptide A with His-tag expressed by RTS.

Screening positive sera with peptide A. ELISA results are shown in Figure A.5; some statistical analyses are shown in Tables A.2 and 3. No statistical difference is found between the age distribution of breast cancer patients and healthy donors as shown in Table A.2. The mean absorbance of serum IgG antibody from patients and healthy donors were 0.401 ± 0.163 SD and 0.137 ± 0.121 SD, respectively. Sixty-five percent (39 of 60) of breast cancer patients and 13% (4 of 30) of healthy donors had a specific absorbance of IgG antibody against peptide A greater than the mean absorbance of healthy donors; there exists a statistically significant difference between serum antibody levels from patients and healthy donors (*t* test, $P < 0.001$). This result strongly indicates that the antigen expressed by breast cancer cells may be responsible for the higher level of sera antibody in breast cancer patients.

Table A.2: Comparison of ages and sera antibody levels between patients and donors

	Mean \pm SD		Percentage of difference*	P from unpaired <i>t</i> test
	Patients	Donors		
Age (y)	44.63 \pm 7.05	43.89 \pm 6.09	1.6	0.96
Sera level	0.401 \pm 0.163	0.137 \pm 0.121	192.7	<0.001

*Expressed as $(\text{mean}_{\text{patients}} - \text{mean}_{\text{donors}}) / \text{mean}_{\text{donors}}$.

Further analysis showed that sera antibody levels in 33 cases of stage III is likely associated with menopause status. Sera antibody levels of patients before menopause are significantly higher than sera level of patients after menopause, as shown in Table A.3. However, no difference of sera antibody levels was found between patients before and after menopause in the cases of breast cancer stage I or II. Similarly, no difference of sera antibody levels was found between health donors before menopause (0.102 \pm 0.117 SD) and after menopause (0.182 \pm 0.114SD) ($P = 0.071$).

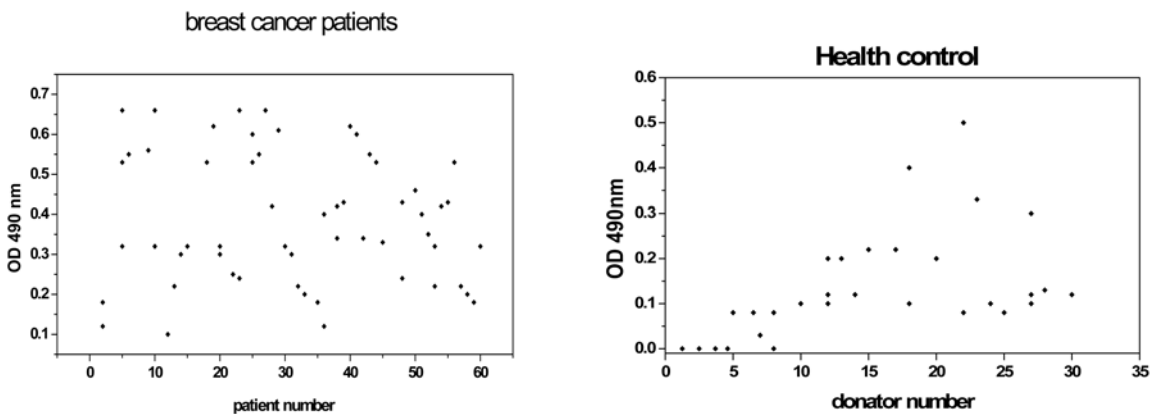


Figure A.5: ELISA analysis of peptide A in serum from 60 patients with breast cancer and 30 healthy female donors. A. Scatter plot of the titers of peptide A in breast cancer patients sera; B. Scatter plot of the titers of peptide A in healthy donors.

Determination of antigen epitope specificity. ELISA competition inhibition assay results (Fig. A.7) show that labeled anti-SSKKQKRSHK antibody was completely inhibited by the unlabeled anti-SSKKQKRSHK antibody and human IgG antibody from positive sera. Results also showed that anti-SSKKQKRSHK antibody is specific to an antigen epitope on peptide A. ELISA Competition Inhibition Assays with Synthetic Peptides. ELISA competition inhibition assay results (Fig. 6) show that SSKKQKRSH was the shortest peptide with optimal inhibition effect among synthetic peptides SSKKQKRSHK, SKKQKRSHK, and SSKKQKRSH.

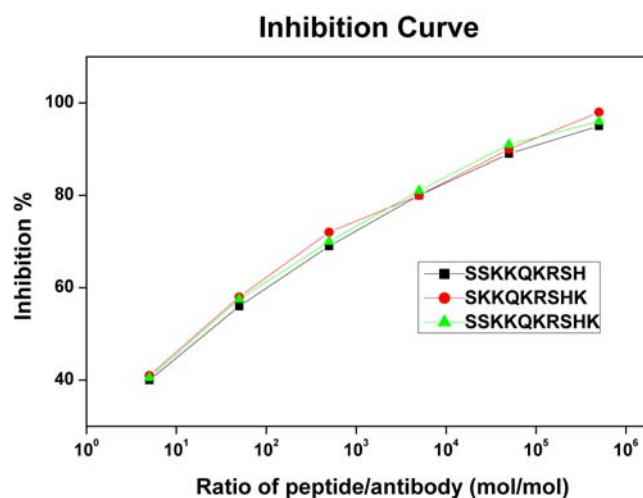


Figure A.6: Competition inhibition assays of synthetic peptides by ELISA. Synthetic peptides SSKKQKRSHK, SKKQKRSHK, and SSKKQKRSH were used for competition inhibition assays at concentrations of 1.7×10^{-9} , 1.7×10^{-8} , 1.7×10^{-7} , 1.7×10^{-6} , 1.7×10^{-5} and 1.7×10^{-4} mol/L. Three inhibition curves were drawn. SSKKQKRSH is the shortest peptide with optimal inhibition effect.

Immunoprecipitation and Western blotting analysis. Immunoprecipitation and Western blotting results (Fig. A.7) show that the IgG antibody reactivity to peptide A was completely absorbed by the soluble cytoplasmic fraction of MCF-7 cells; there was no absorption by cell membrane or the nuclear fractions. The results also show that SSKKQKRSHK peptide epitope is in the cytoplasm of breast cancer cells.

Table A.3: Comparison of sera antibody levels between breast cancer stage and menopause status

	Pre-menopause	Post-menopause	P value from t test
	N (mean \pm SD) 95% CIs	N (mean \pm SD) 95% CIs	
Stage I	5 (0.446 \pm 0.230) (0.220-0.672)	3 (0.460 \pm 0.147) (0.168-0.752)	0.929
Stage II	10 (0.432 \pm 0.175) (0.328-0.536)	9 (0.362 \pm 0.133) (0.252-0.472)	0.346
Stage III	18 (0.327 \pm 0.125) (0.256-0.398)	15 (0.462 \pm 0.173) (0.384-0.540)	0.014

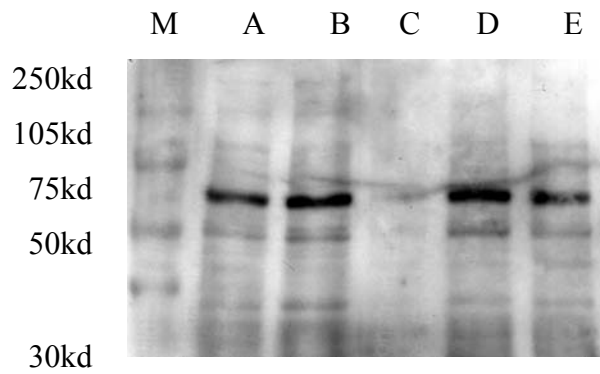


Figure A.7: Western blotting comparing the absorption of specific IgG antibody with a control using preabsorbed antibody (A), membrane protein (B), cytoplasmic protein (C), and nuclear protein obtained from MCF-7 cells (D, E). M, protein marker.

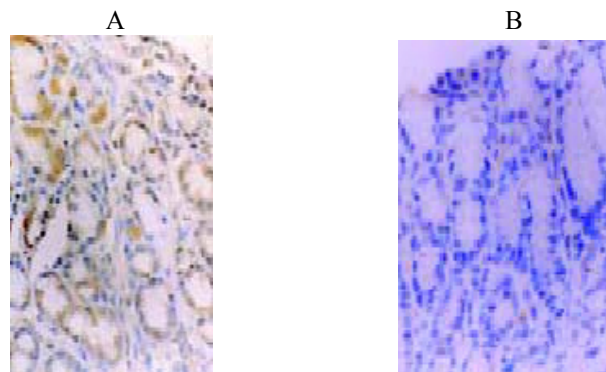


Figure A.8: Immunohistochemical analysis using specific IgG antibody to SSKKQKRSHK of human breast cancer tissues and normal breast tissues. The cytoplasmic protein of breast cancer tissues stained intensive positive (A, magnification, X200). No positive cytoplasmic staining existed in normal breast tissues (B, magnification, X200).

Immunohistochemical staining and statistical analysis. Immunohistochemical staining results are shown in Table A.1. Thirty-nine of 60 primary breast cancer tissues showed a strong positive staining, which is only in the cytoplasm, as shown in Figure 8.A. No positive staining was found in the non-cancerous tissues. There is a statistically significant difference between expression levels of novel antigen epitope in breast cancer tissues and in noncancerous tissues ($P < 0.01$), this result indicates that the expression of novel antigen epitope is associated with breast cancer status. Positive rate of novel antigen epitope in patients before menopause and after menopause are 56.4% (22 of 39) and 43.59% (17 of 39), respectively. X^2 analysis showed that the expression of novel antigen epitope is uncorrelated with patient ages, even if they are classified as pre- and post-menopause. Further statistical analysis showed that novel antigen epitope expression is closely associated with the values of ERp and PRp in breast cancer tissues, as shown in Table 4.

Table A.4: Comparison of ERp and PRp association with expression of novel antigen epitope.

	Positive novel antigen epitope N (mean \pm SD) 95% CIs	Negative novel antigen epitope N (mean \pm SD) 95% CIs	<i>P</i> value from <i>t</i> test
ERp	39 (76.9 \pm 19.4) (67.21 to 86.63)	21 (39 \pm 44.1) (25.82 to 52.28)	<0.001
PRp	39 (64.9 \pm 29.5) (56.67 to 73.08)	21 (8.10 \pm 15.6) (-3.085 to -19.28)	<0.001

As shown in Table A.5, ERp is associated with either metastasis or infiltrate of breast cancer, whereas PRp is not associated with either metastasis or infiltrate of breast cancer.

Table A.5: Comparison of ERp and PRp association with breast cancer metastasis and infiltrates

	Metastasis or infiltrate N (mean \pm SD) 95% CIs	No metastasis or No infiltrate N (mean \pm SD) 95% CIs	<i>P</i> value from <i>t</i> test
ERp	8 (20 \pm 27.8) (-1.832 to 41.83)	52 (70.4 \pm 31.2) (61.82 to 78.95)	<0.001
PRp	8 (25 \pm 35.5) (-1.005 to 51)	52 (48.1 \pm 36.9) (37.88 to 58.28)	0.104

Clinical data showed that among 39 positive specimens of novel antigen epitope, 35 positive specimens were with non-metastasis and non-lymphocytic infiltrates, and with ERp > 30 and PRp > 30; the remaining 4 positive specimens were respectively found in 1 of 4 specimens of hereditary breast cancer, 1 of 5 metastasis specimens, and 2 of 6 specimens with lymphocytic infiltrates; these specimens all exhibited ERp < 30 and PRp < 30. Further statistical analysis showed that ERp was associated with metastasis or infiltrate in the cases of breast cancer with positive novel antigen epitope; PRp was not associated with metastasis or infiltrate (PER = 0.044, and PPR = 0.619). Therefore, positive expression of novel antigen epitope, simultaneously with ERp > 30 and PRp > 0, possibly predicts good prognosis of breast cancer patients, such as no-metastasis and no-lymphocytic infiltrate. Conversely, the positive expression of novel antigen epitope, ERp \leq 30 and null PRp, possibly predicts bad prognosis of breast cancer, such as metastasis and lymphocytic infiltrate.

Positive ratio of novel antigen epitope in breast cancer tissues with I, II, III grade were 87% (57.20% to 98.84%), 79% (60.12% to 90.56%), and 45% (29.58% to 53.29%), respectively; all CI with a 90% of confidence, *P* = 0.0989. This result indicates that the expression of novel antigen epitope has no difference with histologic grade I, II, and II.

According to the abovementioned results, a simple prognosis model based on PR and ER thresholds is established to explain the data. A prognosis based on PR and ER thresholds may be reasoned as a Bernoulli process, in which each patient is an independent event that either has expression of novel antigen epitope or not. Therefore, confidence limits can be

estimated for with a two-tailed probability $\Pr[-z \leq x \leq z] = 90\%$, $z = 1.65$, $N = 60$. Thus, the probability of issuing a successful prognosis lies between 85.9% and 96.9%.

The model we found is depicted in Figure A.9 A, and it implies that a good prognosis (positive novel antigen epitope) is associated to $ERp > 30$ and $PRp > 0$; meanwhile the bad prognosis (negative novel antigen epitope) sets two cases: (i) $ERp \leq 30$ and null PRp , and (ii) when PRp is null. The classification result with the model is shown in Figure A.9 B. Its sensitivity is 100% and its specificity is 81%; false positives or misclassifications were found in four cases, such as No. 26, 30, 39, 56 samples, which actually exhibited negative expression of novel antigen epitope and positive expression of $ERp > 30$ and $PRp > 0$.

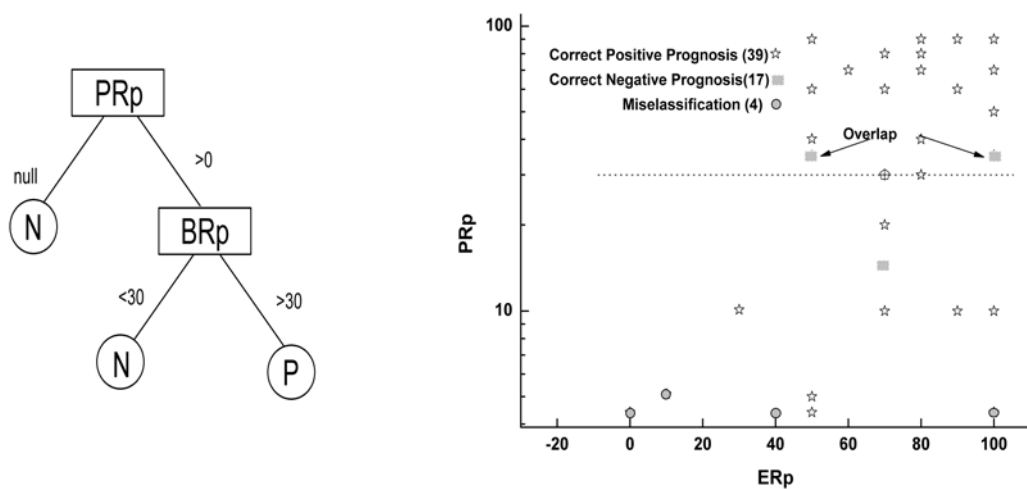


Figure A.9: Model based on ERp and PRp and classification result with model. A. Resulting prognosis model found by stepwise forward selection. This tree shows how the coexpression between PRp and ERp is related to novel antigen epitope. N, negative novel antigen epitope; P, positive novel antigen epitope. B. Classification result with the model based on PR and ER thresholds. Correct positive prognosis, specimen with positive expression of novel antigen epitope. Correct negative prognosis, specimen with negative expression of novel antigen epitope. Misclassification, specimen with mistaken positive or negative expression of novel antigen epitope.

Discussion

Looking for novel antigen epitopes of breast cancer helps us to clarify its mechanism in favor of its diagnosis, treatment, and prevention^{185, 186}. The *brca1* gene (breast cancer associated antigen 1 gene, AF208045), which we previously cloned, exhibits differential expression between breast cancer and normal breast tissues. Its genomic characteristics, such as location at 1q42.1-43 on human chromosome, full-length sequence of 93.857 kb, including 18 exons and 17 introns, are identified. Its protein structure characteristic also has been analyzed

as shown in Figure A.3. For example, its second structure includes 10 glycosylate sites; the region 740 to 750 sites at NH₂ terminus is very hydrophilic, indicating that this region may form helix^{187, 188}.

Because BRCAA1 protein includes the same antigen epitope IKPSLGSKK as RB binding protein 1, BRCAA1 protein may be one member of RB binding protein family. Rb is an important antioncogene; RB protein regulates transcriptional events, which are important for cell proliferation. A major target of pRB is the E2F family of transcription factors that controls expression of many genes required for DNA synthesis and cell cycle progression. Binding of pRB to E2F species inhibits expression of E2F-regulated genes, resulting in withdrawal from the cell cycle. pRB and related pocket proteins use multiple mechanisms to elicit this effect^{189,190}. RB family members are able to recruit the mSIN3-HDAC complex via a pocket-dependent association with RBP1 to actively repress transcription. RBP1 is the first molecule described that seems to contribute to two separated classes of transcriptional repression activities, which are important for transcriptional repression by RB family members, both by recruiting the mSIN3-HDAC complex via R2 and via an as yet unidentified repression mechanism using the R1 domain. These dual repression activities of RBP1 may account for the ability of pRB to repress transcription in a variety of promoters, including those that have been reported to be insensitive or only partially sensitive to the HDAC inhibitor tissue specific antige¹⁹¹. Therefore, BRCAA1 may be associated with regulating cell cycle. Further clarification of its concrete function is under way.

Besides the known antigen epitopes, another novel antigen epitope inside BRCAA1 protein has been predicted by AI, and identified by series of experiments.¹⁹² The novel antigen epitope is in the region 610 to 619 sites; its shortest sequence is SSKKQKRSHK. The antigen epitope is in the cytoplasm of breast cancer cells by immunohistochemical staining. In our experiments, the peptide A, including predicted antigen epitope, was expressed by using RTS system. This RTS system is very useful, which can produce 50 to 100 mg target proteins with natural activity in 3 to 5 hours, and the target protein is easily purified and kept active¹⁹³. Our experiments also fully demonstrate that AI can be used to predict the potential antigen epitope.

In our study, the clinical significance of novel antigen epitope was investigated. Its expression levels in breast cancer and non-cancerous tissues were analyzed via immunohistochemistry. Our initial exploration showed that the expression of novel antigen epitope seems to be associated with breast cancer, but not associated with histologic grade of breast cancer, uncorrelated with patient ages and menopause status. Later, further statistical analysis also shows that it is closely associated with the status of ER and PR in breast cancer

tissues. A simple model to explain the data is established based on two variables, ERp and PRp. The model is described in the previous section. This analysis unravels an astonishing model with 100% of sensitivity and 81% of specificity. Unfortunately, this model is unable to capture four cases, such as four patients of No. 26, 30, 39, and 56, who actually exhibited negative expression of novel antigen epitope, but positive expression of ERp > 30 and PRp > 0. Confidence limits show that the probability of issuing a successful prognosis lies between 85.9% and 96.9%. The model also fully supports that the expression of novel antigen epitope is closely associated with the status of ER and PR in breast cancer.

Previous studies have shown that ER- and PR-positive breast cancers compared with ER- and PR-negative ones have a less aggressive, more differentiated phenotype, and a more favorable prognosis¹⁹⁴. In this study, the expression level of ER was found to be associated with prognosis of breast cancer, such as metastasis or infiltrate. Our result also corresponds with some reports¹⁹⁵. Conversely, the expression level of PR was not found to be associated with prognosis, such as metastasis or infiltrate of breast cancer ($P = 0.104$). This result conflicts with some reports¹⁹⁶. This may be because our analysis is based on a small data set. Increasing the sample number may result in more precise results. The status of ER and PR in breast cancer is an important reference factor for breast cancer therapy.

Muss et al. reported that tamoxifen therapy can significantly decrease the risk of recurrence and improve survival in women of all ages having ER- or PR-positive invasive breast cancer^{197, 198}. Therefore, the status of novel antigen epitope in breast cancer tissues is also possibly an important reference factor for breast cancer therapy. Investigation for its significance on breast cancer therapy is under way.

In our study, the sera antibody levels of novel antigen epitope in breast cancer patients and healthy female donors were investigated via ELISA. The results showed that titer levels of sera antibody from breast cancer patients are dramatically higher than healthy donors, highly indicating that sera antibody level of novel antigen epitope is helpful for breast cancer diagnosis, although the result is based on a small sample. Statistical analysis also shows that sera antibody levels of breast cancer stage III are associated with menopause status; the sera antibody level of patients before menopause is significantly higher than ones of patients after menopause. However, no difference of sera antibody levels was found between patients before and after menopause in breast cancer stage I or II. Similarly, no difference was found between healthy female donors before menopause and after menopause. So far the critical threshold of sera antibody for distinguishing the breast cancer patients from non-breast cancer patients still needs to be further determined by screening a lot of breast cancer sera.

In conclusion, a breast cancer associated antigen 1 gene, *brca1*, genomic characteristics were obtained, such as location in 1q42.1-43 and full length of 93.857 kb, including 18 exons and 17 introns. BRCAA1 protein structure is characterized as being composed of 1,214 amino acids, including 10 glycosylate sites and two known antigen epitopes, such as KASIFLK and IKPSLGSKK, the region 740 to 750 sites at NH₂ terminus being very hydrophilic, indicating that this region may form helix. Its novel antigen epitope, SSKKQKRSHK, was identified and found in the cytoplasm of breast cells. The expression of novel antigen epitope in breast cancer tissues is closely associated with the status of ER and PR in breast cancer tissues. Its sera antibody level is helpful for early diagnosis of breast cancer. Because our result is based on a small sample, BRCAA1 function and its novel antigen epitope potential significance still need to be further investigated.

Appendix B

Transitorily Influence of Magnetic Fields and Ionizing Radiation on c-jun, c-fos and BRCA1

Abstract

Epidemiological studies suggest that exposure to power frequency magnetic fields maybe a risk factor for breast cancer in humans. If exposure to 60-Hz ELF magnetic fields contributes to the etiology of breast cancer, it is likely that it must affect genetic material. The effect of magnetic fields (50Hz, 5mT) and/or X-rays on the expression of the BRCA1, p21, c-myc, c-jun and c-fos proteins was investigated in MCF-7 cells. Transitorily of induction of c-jun, c-fos and BRCA1 were evidenced after either ionizing radiation or magnetic fields exposure, but there is not effect on c-myc and p21. These finding suggest that magnetic fields explored in the present study may be considered as a transiently insult cellular level.

Introduction

Possible health effects due to exposure to power frequency magnetic fields have already become a public concern. Some epidemiological studies have indicated that residential or occupational exposure to power frequency magnetic fields may increase the risk of breast cancer^{199, 200}. The BRCA1 tumor suppressor gene is found in many families with inherited breast and ovarian cancers. The effect of BRCA1 as a cofactor in the transcriptional regulation of a gene may thus occur through direct activity at the promoter or, indirectly, by the relief of transcriptional repression through titration of s corepression or by suppression of a transcription factor^{201,202}. Harkin group showed that enhancing BRCA1 can activate JNK phosphorylation²⁰³. A characteristic feature of c-fos and c-jun are that its expression can be rapidly and transiently induced by a variety of extracellular stimuli through several second messenger pathways²⁰⁴. Some laboratory studies have indicated that MFs (magnetic fields) exposure appeared to increase c-fos and c-jun expression²⁰⁵. Unfortunately, there are discrepancies between no less than 7 labs in the gene expression of c-myc and c-fos, especially for low fields (< 0.05 mT)²⁰⁶. The reason why seems to be different magnetic flux and parameters. Repeating experiment is needed to confirm these results.

Growth associated genes, such as c-myc and p21 proto-oncogenes are activated during cellular proliferation processes. The c-myc activation is hue to signal transmitted from the cellular membrane to its nucleus. In our earlier experiments, we found that exposure to ELF following irradiation can decrease the levels of caspase-3, p21, p53 and phosphor-p53 and increase bcl-2 expression in xrs-5 cell, decrease bax and increase bcl-2 in MCF-7 cell1. These results to suggest that MFs could interfere with affect genetic material the repair of DNA

damage cause by irradiation and affect genetic material. If ELF magnetic field is associated with an increased risk of cancer, it is likely that it must affect genetic material.

What is required is a detailed understanding of how EMF exposure affect signal transduction pathways that lead to gene transcription, and it is in this area that efforts should be concentrated. The possibility of health risk provides a strong motivation to provide possible mechanisms by which EMF could affect cell function using mechanisms consistent. It is necessary to carry out laboratory experiments to analyze the biological mechanisms that are affected by EMF company X-rays. We used MCF-7 cells, a cellular model reported usefully for detecting environmental toxicants in different stages of the multi step carcinogenesis.

Material and methods

Cell culture

The human breast adenocarcinoma cell lines MCF-7 is obtained from ATCC (Manassas, VA). The MCF-7 cells was cultured in Dulbeccos modified Eagle medium (Nikken Bio medical Laboratory, Kyoto, Japan) supplemented with 10% bovine calf serum (GIBCO, BRL), 0.1mM pyruvate (GIBCO, BRL), 0.01mg/ml insulin (GIBCO, BRL), 100units/ml penicillin G, 100mg/ml streptomycin, and 2mM glutamine, at 37°C in an atmosphere of 95% air and 5% CO₂.

ELF Magnetic field and X-ray exposure

The exposure apparatus for 5mT EMF is described elsewhere²⁰⁷. Environmental 60Hz EMF during the sham exposure were <0.5μT. Static magnetic fields, other than geomagnetism, was undetectable (<0.1μT) for all experiments and residual geomagnetism was <1μT. The atmosphere in the incubator for both units was saturated with humidified of 95% air plus 5% CO₂. The conditions for X-irradiation have been described previously. Cells were irradiated with X-rays at 1.0Gy/min.

Cell survival assay

A colony formation assay was performed. The MCF-7 cells were plated in dishes at a density of 2X10⁶ cells/dish. Cells were allowed to adhere for 5h and then exposed to X-rays. Immediately after irradiation, Cell number was determined with a particle counter (Beckman coulter) and cells were then plated appropriately. The cells were exposed to a 5mT ELF for 14d. Fourteen days later, the cells were fixed and stained with crystal violet. The survival of the irradiated cells was normalized by comparison to the plating efficiency of non-irradiated control.

Western blotting

Our previously reported method was used for the preparation of cell protein extracts¹⁵. Protein extract was boiled in sample buffer for 3min and loaded onto 7%, 10% and 12% SDS-polyacrylamide gels. Details of the western immunoblotting procedure have been described elsewhere. The antibodies used in this experiment were as follows: BRCA1, P21, c-myc, c-fos and c-jun (Oncogen Science, Inc., Uniondale, NY, 1000:1 dilution) anti-mouse IgG horseradish peroxidase (Amersham Pharmacia Biotech, 1500:1 dilution), The blot was visualized with an

ECL kit (Amersham Pharmacia Biotech). Densitometric analysis was performed using NIH Imaging 1.61.

Result

Effect of exposure to Magnetic on Cell Survival

The influence of the magnetic field on the survival of MCF-7 cells was evaluated. Figure B.1 Shows that exposure to the 60-Hz MF has little or no effect on the survival of MCF-7 after X-ray irradiation.

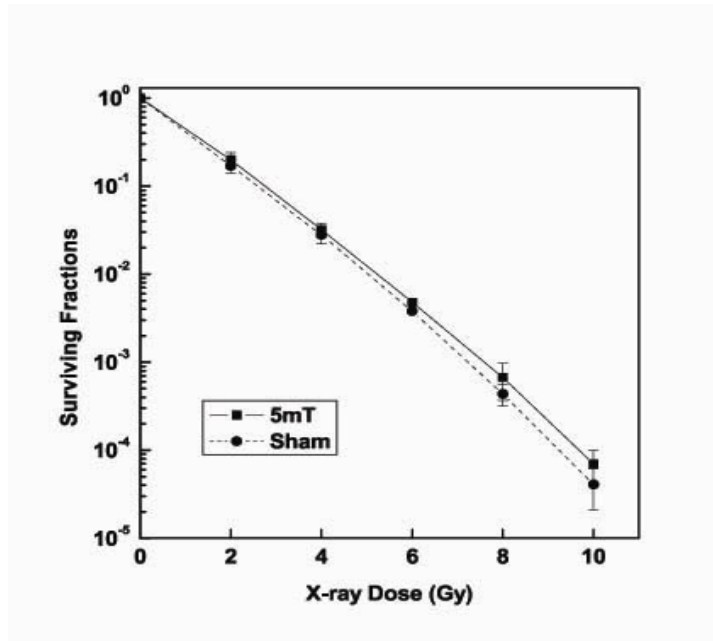


Figure B.1: Effect of exposure to ELF electromagnetic fields on cell survival in MCF-7. Cell were exposure or shamexposure to ELF electromagnetic fields for 24h after X-ray irradiation. Five replicate plates were used for each time point, and the experiment were performed at least three times. Error bars show the standard deviation.

Protein expression after exposure to magnetic fields and/or X-rays

In order to confirm the effect of ELF magnetic fields on X-rays, in this study, we showed that X-rays and MF affected the expression of both c-jun and c-fos encoded proteins in breast cancer cells with early courses. Relative protein levers in control and irradiated and/on MF exposed cells are presented in Figure B.2.

Exposure to ELF magnetic field alone can induction occurred c-jun expression at 8h. At longer exposure time, c-jun expression decreased to control level after exposure 12h (Fig. B.2 B) .However, there was no similar change in the levers of c-fos proteins over 24h exposed to ELF magnetic field alone (Fig. B.2 C). After 2h exposure to MF or X-rays irradiation alone there is not expression in c-fos and c-jun. X-rays company MF can statistically significant increase in c-jun expression was observed in MCF-7 cells from 2h (Fig. B.2 A). The c-jun expression increased with increasing ELFMF exposure time after X-ray, similar phenomena were observed in X-rays company ELFMF, but the c-jun expression of X-rays company ELFMF is higher than X-ray alone's. There is not significant change between X-rays alone and

X-rays company ELFMF in c-fos expression at 24h after radiation. Similar induction occurred in c-fos 8h after irradiation. X-rays company ELFMF a significant 1.5-fold increase in c-fos expression was observed (Fig. B.2 B). At longer exposure time, c-fos expression decreased to control level interaction was observed between ELFMF and ionizing radiation (Fig. B.2 C).

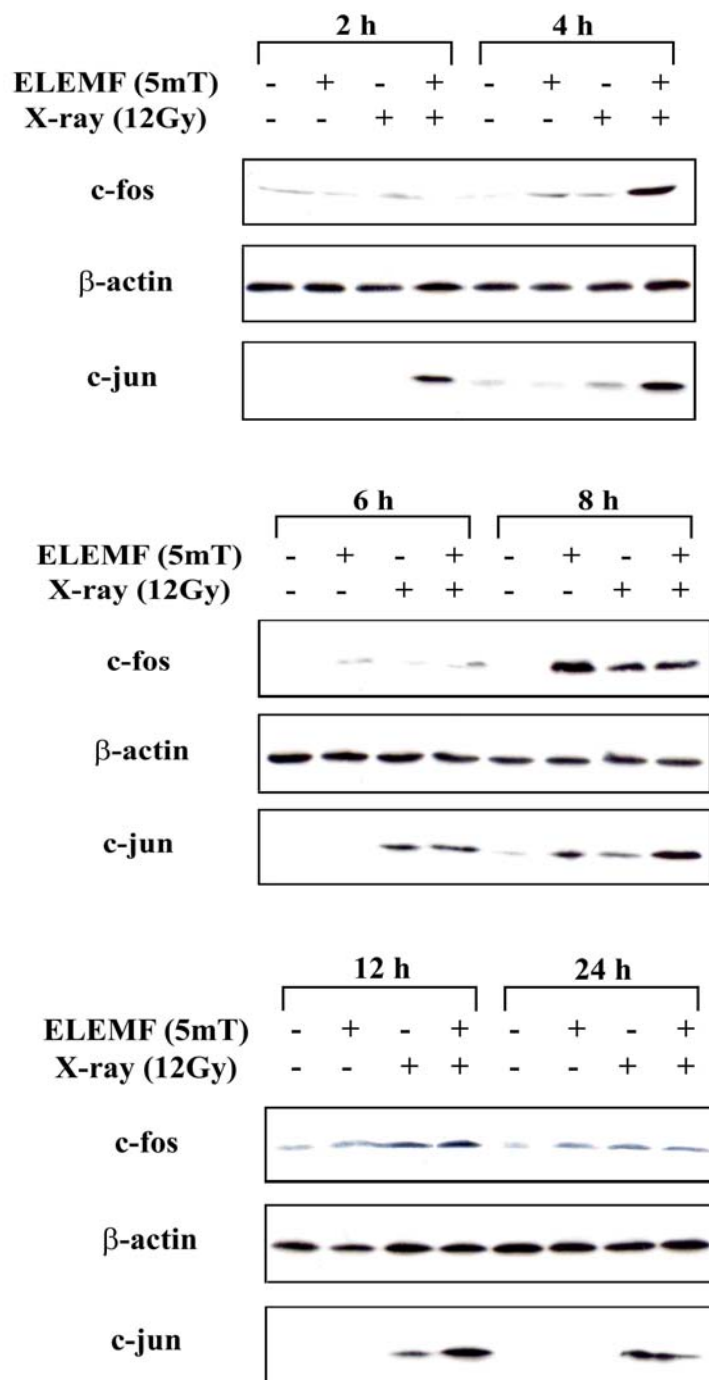


Figure B.2: Induction of c-fos and c-jun after exposure to ELF electromagnetic fields and/or X-ray irradiation in MCF-7 cells. Cells were exposed to ELF electromagnetic fields for 2h, 4h, 6h, 8h (early courses), 12h and 24h, with or without X-ray(12Gy) pretreatment. Western blots were performed as described in material and methods, and a representative Western blot is shown.

In order to confirm the effect of ELF magnetic field on X-rays induced Cell cycle related gene c-myc, p21 and BRCA1 expression levels were determined by Western blotting. After 12Gy X-ray irradiation, c-myc, p21 and BRCA1 expression clearly increased. No induction of P21 and c-myc were observed in MF alone and 2-fold increase occurred after exposure to either X-ray treatment (Fig.3). There is not significant change between X-rays alone and X-rays company ELFMF in c-myc and p21. The significant 2-fold increase in BRCA1 expression was observed. The BRCA1 expression of X-rays company ELFMF is higher than X-ray alone's after a 12h exposure to MF.

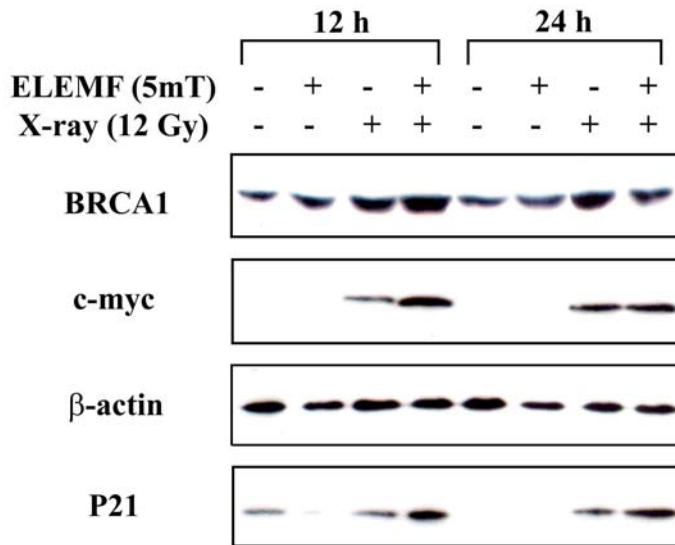


Figure B.3: Induction of BRCA1, c-myc, and p21 after exposure to ELF electromagnetic fields and/or X-ray irradiation in MCF-7 cells. Cells were exposed to ELF electromagnetic fields for 12h and 24h, with or without X-ray(12Gy) pretreatment. Western blots were performed as described in material and methods, and a representative Western blot is shown.

Discussion

Exposure to ionizing radiation is known to increase the risk of breast cancer, and to upregulate the expression of c-fos, c-jun, c-myc, p21 and BRCA1. The p21 and c-myc genes are thought to directly regulate the cell cycle, and the p21 protein product inhibits DNA replication by blocking cyclin dependent kinase (CDK)²⁰⁸. In present study, 2-fold increase occurred after exposure to either X-ray treatment. Exposure to ELF electromagnetic fields at 5mT showed no effect on P21 and c-myc (Fig. B.3). These results are consistent with our previous report on P21 and cell cycle distribution in MCF-7 cells. It was found that MCF-7 cells to 60Hz ELFMF have little or no effect on the survival after X-ray irradiation (Fig. B.1). 60-Hz ELFMF failed to induce cell cycle relative genes p21 and c-myc expression in MCF-7 cells after X-rays radiation. Our data suggest that MF has no effect on cell survival.

Exposure to ELF magnetic field alone can induction occurred c-jun expression at 8h. At longer exposure time, c-jun expression decreased to control level after exposure 12h. The c-fos

and c-jun gene are rapidly and transiently induced in a stereotyped fashion in wide range of cell types by a variety of extracellular signals. Our present result suggest that 60Hz 5mT ELF magnetic field alone can induction occurred c-jun expression.

Ionizing radiation has been widely demonstrated to induce early response gene transcription. Therefore, MF appeared more efficient in ionizing radiation-transformed cells, in which genomic damage would be greater than in normal or spontaneous immortalized cells. In present study, exposure to ELF at 5mT can increase expression in c-fos and c-jun within the first 24h after 12Gy irradiation. These results are consistent with reports: MF exposure appeared to increase c-fos expression in a manner similar to anisomycin²⁰⁹. 1 gauss Sinusoidal magnetic field at 60Hz change the transcription of c-fos, c-jun, c-myc and protein kinase C in CEM-CM3 T-lymphoblastoid cells²¹⁰.

Interesting, quite similar patterns and amplitudes of induction of these proteins were evidenced after either ionizing radiation or magnetic field exposure (Fig. B.2). The synergism after both treatments was observed in c-jun and c-fos. That EM fields may act as co-promoter was supported by EM fields activate involving AP-1 binding activation²¹¹. The BRCA1, c-fos and c-jun, function in the cell as transcriptional regulators, their protein products controlling the expression of 'downstream' genes. The BRCA1, c-fos and c-jun expression of X-rays company ELFMF is higher than X-ray alone's after a 12h exposure to MF (Fig. B. 2 and Fig. B.3). This result is consistent with enhanced BRCA1 activate the c-jun N-terminal kinase (JNK) pathway. BRCA1 expression is capable of responding to MFs with activating stress responses such as the c-fos and c-jun pathway. Activation or repression of transcriptional targets of the BRCA1 protein might play a role in tumor initiation or progression. These changes in gene expression may underpin some of the pathological changes associated with the tumors.

In our previous studies, we have reported that exposure to ELFMF can transiently increase the ratio of bcl-2 to BAX in MCF-7 cells and in NF-kB-inhibited cells, decreasing the levels of p21, caspase-3, p53, phosphor-p53 in xrs5 cells. Another mechanism that has been suggested is association with the modulation of Ca²⁺ influx by magnetic fields²¹². We showed that X-rays and MF affected the expression of both c-jun and c-fos encoded proteins in breast cancer cells with early courses. The MF does not only interact with the various membrane receptors to activate parallel cascades, but the magnetic fields can interact with conducting electrons in the early irritability response protein c-jun and c-fos. Here, we provide the first report that BRCA1 is affected by ELF magnetic fields. This result may provide a necessary biological mechanism to explain EMF effect on breast cancer.

Acknowledgments

Finally, after three years, the time to thank a lot of people that made this time a wonderful experience both professionally and personally have arrived. I will keep in mind that it is difficult to find the words to express what I really feel.

First I would like to thank my promoter Professor Prof. Dr Eduard Arzt for the privilege and opportunity he has given me to work in Max-Planck Institute where is cumulated higher level scientists.

I want to thank my supervisor Prof. Dr Joachim P. Spatz for providing me the chance to study in his group and giving me all the freedom that I never predicted before. He guided me through the necessary process to get this thesis done, had his office's door always open for me, even when he was really busy. The research described in Chapter 5 and 6 is performed in his department.

I must thank many and many people who help me during my research. First, I would like thank Stefan Gräter for the collaboration in the experiments reported in (Chapter 5 and 6). I thank Giovani Gomez Estrada for encouraging me to learn European research which is far different from the Asian one. He has always been eager to help me, to give me advices and suggestion, to listen to my complains. Julia Schölermann, Francesca Corbellini, Ralf Kemkemer, Beri Nsoyani Mbenkum, Eva Bock, Hatice Acunman, Nicole Rauch, Raquel Martin, Josif-Dorin Manciuła, Steffen Albrecht, Michael Hirscher, Stanislav Gorb, Silvia Casanova and Elisabeth Pfeilmeier made my life positive and refreshed my general knowledge from different countries and different continents. I can say I learned many things which I have not seen before.

If I look back to the past three years and I consider the good and bad aspects of dealing with a multidisciplinary project, I can not deny that what I have mostly enjoyed is the opportunity and pleasure to cooperate and interact with many people. I also thank Prof H. Gao to let me join a very young and intriguing project. The research described in Chapter 2 to 4 is

performed in his department. I would like to thank Dr. Cui for accepting me for his project and allowing me to share achievements with him in Chapter 2 to 4 and Appendix A. I wish to thank Ms. M. Kelsch and Dr. F. Phillipp from the Max Planck Institute for Metals Research (Stuttgart) for their help with the HRTEM measurements, Heinz Schwarz and Mr. J. Berger of the Max Planck Institute for Developmental Biology for technical assistance with TEM and SEM.

I want to thank Francesca Corbellini and Iain Dunlop for reading and correcting my concept thesis, I hope that they did it with smile.

Curriculum vitae

Name: Furong Tian

Birth: April, 14th, 1971

Place of birth: in Shannxi, China

Gender: Female

Nationality: Chinese

Marry status: single

1983-1989: Qingan high school, Shannxi, China

1989-1994: Study Medicine in Jiaotong University, Xi'an, China

1994: Medicine diploma in 1994 in Xi'an Jiao Tong University, China

1994-1999: Work in radiology department in Fourth Military Medical University, China

1999-2002: Study Biochemistry in Fourth Military Medical University, China

2000-2002 Radio-Genetic Department, Kyoto University, Japan

2002: Master degree in Fourth Military Medical University, China

2002-2005, PhD student in Max-Planck Institute metal research in Stuttgart.

REFERENCES

- ¹ The Royal Society and the Royal Academy of Engineering, commissioned by the UK Government, issued a report (Royal Soc. 2004) on nanotechnologies.
- ² Bruchez M., Moronne J.M., Gin P., Weiss S., and Paul A. Alivisatos Semiconductor Nanocrystals as Fluorescent Biological Labels. *Science* 1998, 281, 1201-1206.
- ³ Das B., McGinnis S.P., and Sines P. Nanostructured Arrays for Multijunction Solar Cells NAMBE 2004 - 22nd North American MBE conference – Banff, Alberta, Canada
- ⁴ Khitun A. and Wang K., Cellular Nonlinear Network Based on Semiconductor Tunneling Nanostructured IEEE transactions on electron devices. 2005, 53,183.
- ⁵ Karuri N. W., Liliensiek S., Teixeira A. I., Abrams G., Campbell S., Nealey P. F. and Murphy C. J. Biological length scale topography enhances cell-substratum adhesion of human corneal epithelial cells. *J. Cell. Science* 2004, 117, 3153-3164.
- ⁶ Iijima S. and Ichihashi T. Single-shell carbon nanotubes of 1-nm diameter, *Nature* 1993, 363, 603.
- ⁷ Ebbesen T W. Molecular mechanics of binding in carbon-nanotube-polymer composites. *Annu. Rev. Mater. Sci.* 1994, 24, 235–264.
- ⁹ Chen C. S., Mrksich M., Huang S., Whitesides G. M., Ingber, D. E. *Biotech. Prog.* 1998, 14, 356-363.
- ⁹ Lee K. B., Park S. J., Mirkin C. A., Smith J. C. and Mrksich M. *Science (Washington, D.C.)* 2002, 295, 1702-1705.
- ¹⁰ Ebbesen T. W. Molecular mechanics of binding in carbon-nanotube-polymer composites. *Annu. Rev. Mater. Sci.* 1994, 24, 235–64
- ¹¹ Bahr J.L., Tour J.M. Covalent chemistry of single-wall carbon nanotubes. *J. Mater. Chem.* 2002, 12, 1952–1958.
- ¹² Baughman R.H., Zakhidov A.A. and Heer D.A. Carbon nanotubes—the route toward applications. *Science* 2002, 297, 787–792.
- ¹³ Nogao E., Nishijima H., Akita S., Nakayama Y. and Dvorak J.A. The cell biological application of carbon nanotube probes for atomic force microscopy: comparative studies of malaria-infected erythrocytes. *J. Electron Microsc.* (Tokyo) 2000, 49, 453–458.
- ¹⁴ Bianco A. and Prato M. Can carbon nanotubes be considered useful tools for biological applications? *Adv. Mater.* 2003, 15, 1765–1766.
- ¹⁵ Gao H., Kong Y., Cui D., Ozkan C.S., 2003. Spontaneous insertion of DNA oligonucleotides into carbon nanotubes. *Nano. Lett.* 3, 471–473.
- ¹⁶ Cui D., Ozkan C.S., Ravindran S., Kong Y. and Gao H.. Encapsulation of Pt-labelled DNA molecules inside carbon nanotubes. *Mech. Chem. Biosystems* 2004, 1, 113–121.

-
- ¹⁷ Shim M., Kam N.W.S., Chen,R.J., Li Y. and Dai, H.Functionalization of carbon nanotubes for biocompatibility and biomolecular recognition. *Nano Lett.* 2002, 2, 285–288.
- ¹⁸ Huczko A. and Lange H. Carbon nanotubes: experimental evidence for a null risk of skin irritation and allergy. *Fullerene Science and technology* 2001, 9, 247-250.
- ¹⁹ Huczko A., Lange H., Calko E. Physiological testing of caeon nanotubes:Are they asbestos-like? *Fullerene Science and technology* 2001, 9, 251-254.
- ²⁰ Lam C.W., James J.T., McCluskey R. and Hunter, R.L. Pulmonary toxicity of single-wall carbon nanotubes in mice 7 and 90 days after intratracheal instillation. *Toxicol. Sci.* 2004, 77, 126–134.
- ²¹ Warheit D.B., Laurence B.R., Reed K.L., Roach D.H., Reynolds G.A. and Webb T.R. Comparative pulmonary toxicity assessment of single-wall carbon nanotubes in rats. *Toxicol. Sci.* 2004, 77, 117–125.
- ²² Mattson M.P., Haddon R.C. and Rao A.M.. Molecular functionalization of carbon nanotubes and use as substrates for neuronal growth. *J. Mol. Neurosci.* 2001, 14, 175–182.
- ²³ Shvedova A.A., Catranova V., Kisin E.R. Exposure to carbon nanotube material: assessment of nanotube cytotoxicity using human keratinocyte cells. *J. Toxicol. Environ. Health A.* 2003, 66, 1909-26.
- ²⁴ Adelmann P., Baierl T., Drosselmeyer E., Politis C., Polzer G., Seidel A., Schwegler-Berry D. and Steinleitner C. Effects of fullerenes on alveolar macrophages *in vitro*. In *Toxic and Carcinogenic Effects of Solid Particles in the Respiratory Tract* 1994, 405–407, ILSI Press, Washington, DC
- ²⁵ Benson J. M., Tibbetts B. M. and Barr E. B. The uptake, distribution, metabolism, and excretion of methyl tertiary-butyl ether inhaled alone and in combination with gasoline vapor. *J. Toxicol. Environ. Health A/* 2003, 66, 1029-1052.
- ²⁶ St. John P. M., Kam L., Turner W. T., Craighead H., Isaacson M., Turner J. N., and Shain W. Preferential glial cell attachment to microcontact printed surfaces. *J. Neurosci. Meth.* 1997, 75, 171–177.
- ²⁷ Khitun A. and Kang L. Wang, On the modeling of lattice thermal conductivity in semiconductor quantum dot superlattices. *Applied Physics Letters.* 2004, 84, 1762-1764.
- ²⁸ Lee H., Johnson J.A., He M.Y., Speck J.S. and Petroff P.M. Strain engineered self-assembled semiconductor quantum dot lattices” *Applied Physics Letters* 2001, 78, 1, 105.
- ²⁹ Roberts C., Chen S. C., Mrksich M., Martichonok V., Ingber D. E. and Whitesides G. M. Using Mixed Self-Assembled Monolayers Presenting RGD and (EG)₃OH Groups To Characterize Long-Term Attachment of Bovine Capillary Endothelial Cells to Surfaces *J. Am. Chem. Soc.* 1998, 120, 6548-6555.
- ³⁰ Kantlehner M., Schaffner P., Finsinger D., Meyer J., Jonczyk A., Diefenbach B., Nies B., Hölzemann G., Goodman S. L. and Kessler H. *Chembiochem* 2000, 1, 107-114.

REFERENCES

- ³¹ Geiger B., Bershadsky R., Pankov R., Yamada K. M., Transmembrane crosstalk between the extracellular Matrix and the cytoskeleton. *Nature Rev. Cell Biol.* 2001, 2, 793.
- ³² Lo C. M., Wang H. B., Dembo M., and Wang Y. L. 2000. Cell movement is guided by the rigidity of the substrate. *Biophys. J.* 2000, 79, 144–152.
- ³³ Pelham R. J. J. and Wang Y. L. 1998. Cell locomotion and focal adhesions are regulated by the mechanical properties of the substrate. *Biol. Bull.* 1998, 194, 348–350.
- ³⁴ Beningo K. A., and Y. L. Wang. 2002. Fc-receptor-mediated phagocytosis is regulated by mechanical properties of the target. *J. Cell Sci.* 2002, 115, 849–856.
- ³⁵ Deroanne C. F., Lapiere C. M. and Nusgens B. V. In vitro tubulogenesis of endothelial cells by relaxation of the coupling extracellular matrix-cytoskeleton. *Cardiovasc. Res.* 2001, 49, 647–658.
- ³⁶ Geiger B. Encounters in space. *Science* 2001, 294, 1661–1663.
- ³⁷ Cukierman E., Pankov R., Stevens D. R. and K. M. Yamada. Taking cell-matrix adhesions to the third dimension. *Science* 2001, 294, 1708–1712.
- ³⁸ Engler A., Bacakova L., Newman C., Hategan A., Griffin M. and Discher D. Substrate Compliance versus Ligand Density in Cell on Gel Responses. *Biophysical J.* 2004, 86, 617–628.
- ³⁹ Glass R., Arnold M., Cavalcanti-Adam E. A., Blümmel J., Haferkemper C., Dodd C. and Spatz J. P. *New J. Physics* 2004, 6, 101-118.
- ⁴⁰ Glass R., Möller M. and Spatz J. P. Block copolymer micelle nanolithography. *Nanotechnology* 2003, 14, 1153-1160.
- ⁴¹ Hafner J.H., Cheung C.L., Woolley A.T. and Lieber C.M., Structural and functional imaging with carbon nanotube AFM probes. *Prog. Biophys. Mol. Biol.* 2001, 77, 73–110.
- ⁴² Chen R. J., Zhang Y. G., Wang D. W. and Dai H. J. Noncovalent Sidewall Functionalization of Single-Walled Carbon Nanotubes for Protein Immobilization. *J. Am. Chem. Soc.* 2001, 123, 3838–3839.
- ⁴³ Dwyer C., Guthold M., Falvo M., Washburn S., Superfine R. and Erie D. DNA-functionalized single-walled carbon nanotubes *Nanotechnology* 2002, 13, 601–604.
- ⁴⁴ Morinobu E., Kenji T., Susumu I., Kiyoharu K., Minoru S., and Harold W.K. The production and structure of pyrolytic carbon nanotubes (PCNTs). *Journal of Physics and Chemistry of Solids* 1993, 54, 1841-1848.
- ⁴⁵ Sellner L. N., Coelen R. J. and Mackenzie J. S. Reverse transcriptase inhibits Taq polymerase activity. *Nucl. Acids Res.* 1992, 20, 1487–1490.
- ⁴⁶ Borresen A. L. The 1993 Nobel Prize in chemistry--polymerase chain reaction and directed mutagenesis. *Tidsskr. Nor. Laegeforen* 1993, 113, 3668–3669.

-
- ⁴⁷ Hajime G., Terumi F., Yoshiya F., and Toshiyuki O. Method of purifying single wall carbon nanotubes from metal catalyst impurities. (Honda Giken Kogyo Kabushiki Kaisha, Japan. 11-6-2002.
- ⁴⁸ Yasuda A., Kawase N. and Mizutani W. Carbon-Nanotube Formation Mechanism Based on in Situ TEM Observations. *J. Phys. Chem. B* 2002, 106, 13294-13298.
- ⁴⁹ Chiang I. W., Brinson B. E., Smalley R. E., Margrave J. L., Hauge R. H. Purification and Characterization of Single-Wall Carbon Nanotubes. *J. Phys. Chem. B* 2001, 105, 1157-1161.
- ⁵⁰ Harutyunyan A. R., Pradhan B. K., Chang J., Chen G. and Eklund P. C. Purification of Single-Wall Carbon Nanotubes by Selective Microwave Heating of Catalyst Particles. *J. Phys. Chem. B* 2002, 106, 8671-8675.
- ⁵¹ Farkas E., Anderson M. E., Chen Z. H. and Rinzler A. G., Length sorting cut single wall carbon nanotubes by high performance liquid chromatography. *Chem. Phys. Letters* 2002, 363, 111-116.
- ⁵² Moon J.-M., An K. H., Lee Y. H., Park Y. S., Bae D. J. and Park G.-S. High-Yield Purification Process of Singlewalled Carbon Nanotubes. *J. Phys. Chem. B* 2001, 105, 5677-5681.
- ⁵³ Mertig M., Ciacchi L. C., Seidel R., Pompe W., De Vita, A. DNA as a selective metallization template, *Nano Lett.* 2002, 2,841-844.
- ⁵⁴ Chisholm S. A., Teare E. L., Patel B. and Owen R. J. Determination of *Helicobacter pylori* vacA allelic types by single-step multiplex PCR. *Lett. Appl. Microbiol.* 2002, 35, 42-46.
- ⁵⁵ Kenneth J. B., Ronald F., Helmut B., and Luis A. Marky Predicting DNA Duplex Stability from the Base Sequence. *PNAS* 1986, 83, 3746-3750.
- ⁵⁶ Benson J.M., Tibbetts B.M., Barr E.B. The uptake, distribution, metabolism, and excretion of methyl tertiary-butyl ether inhaled alone and in combination with gasoline vapor. *J. Toxicol. Environ. Health A* 2003, 66, 1029-1052.
- ⁵⁷ Lotz M.M., Burdsal C.A., Erickson H.P. and Mc Clay D.R. Cell adhesion to fibronectin and tenascin: quantitative measurements of initial binding and subsequent strengthening response. *J. Cell Biol.* 1989, 109, 1795-1805.
- ⁵⁸ Hynes, R.O. Integrins: versatility, modulation, and signalling in cell adhesion. *Cell* 1992, 69, 11-25.
- ⁵⁹ Hafner J.H., Cheung C.L., Woolley A.T. and Lieber C.M. Structural and functional imaging with carbon nanotube AFM probes. *Prog. Biophys. Mol. Biol.* 2001, 77, 73-110.
- ⁶⁰ Kleinman H.K., Klebe R.J. and Martin G.R. Role of collagenous matrices in the adhesion and growth of cells. *J. Cell Biol.* 1981, 88, 473-485.
- ⁶¹ Trentin A.G., De Aguiar C.B., Garcez R.C.. Thyroid hormone modulates the extracellular matrix organization and expression in cerebellar astrocyte: effects on astrocyte adhesion. *Glia* 2003, 42, 359-369.

REFERENCES

- ⁶² Pucillo C.E., Colombatti A., Vitale M.. Interactions of promonocytic U937 cells with proteins of the extracellular matrix. *Immunology* 1993, 80, 248-252.
- ⁶³ Miyakoshi J., Yoshida M., Yaguchi H. Exposure to extremely low frequency magnetic fields suppresses x-ray-induced transformation in mouse C3H10T1/2 cells. *Biochem. Biophys. Res. Comm.* 2000, 272,323-327.
- ⁶⁴ Lippmann M. Nature of exposure to chrysotile. *Ann Occup Hyg* 1994, 38, 459-67.
- ⁶⁵ Boateng S.Y., Hartman T.J., Ahluwalia N.. Inhibition of fibroblast proliferation in cardiac myocyte cultures by surface microtopography. *Am. J. Physiol. Cell Physiol.* 2003, 285, C171-172.
- ⁶⁶ Miranti C.K. and Brugge J.S. Sensing the environment: a historical perspective on integrin signal transduction. *Nat. Cell Biol.* 2002, 4, E83-90.
- ⁶⁷ Guilak F. Compression-induced changes in the shape and volume of the chondrocyte nucleus. *J. Biomech.* 1995, 28, 1529-1541.
- ⁶⁸ Hendrix M.J., Seftor E.A., Hess A.R.I. Molecular plasticity of human melanoma cells. *Oncogene* 2003, 22, 3070-3075.
- ⁶⁹ Nakagawa S., Takeichi M. N-cadherin is crucial for heart formation in the chick embryo. *Dev. Growth Differ.* 1997, 39, 451-455.
- ⁷⁰ Baughman R.H., Zakhidov A.A. and Heer D.A. Carbon nanotubes—the route toward applications. *Science* 2002, 297, 787–792.
- ⁷¹ Hayashi, M. Tokyo: The world of cell adhesion molecules. *Youdosha*, 1995.
- ⁷² Agami R. and Bernards R. Convergence of mitogenic and DNA damage signaling in the G1 phase of the cell cycle. *Cancer Lett.* 2002, 177, 111–118.
- ⁷³ Wang, Y.P., Yuan, S.L., Chen, X.H., Yang, Y., Song, Y., Chen, N.Y., 2001. Experimental study of apoptosis and its molecular mechanisms of nasopharyngeal carcinoma cell induced by millimetre wave irradiation. *J. Infr. Milli. Wav.* 20, 283–286.
- ⁷⁴ Tsai L.H., Lees E., Faha B., Harlow E. and Riabowol K., The cdk2 kinase is required for the G1-to-S transition in mammalian cells. *Oncogene* 1993, 8, 1593–1602.
- ⁷⁵ Miranti C.K. and Brugge J.S. Sensing the environment: a historical perspective on integrin signal transduction. *Nat. Cell Biol.* 2002, 4, E83-90.
- ⁷⁶ Sasada T., Iwata S., Sato N., Kitaoka Y., Hirota K., Nakamura K., Nishiyama A., Taniguchi Y., Takabayashi A. and Yodoi, J. Redox control of resistance to cis-diamminedichloroplatinum (II) (CDDP)—protective effect of human thioredoxin against CDDP-induced cytotoxicity. *J. Clin. Invest.* 1996, 97, 2268–2276.

-
- ⁷⁷ Akiko Y., Shuzo M., Norio M. and Masae S. Quantitative evaluation of cell attachment to glass, polystyrene, and fibronectin or collagen-coated polystyrene by measurement of cell adhesive shear force and cell detachment energy. *J. Biomed. Mater. Res.* 2000, 50, 114–124.
- ⁷⁸ Alley M.C., Scudiero D.A., Monks A., Hursey M.L., Ceerwinski M.J., Fine D.L., Abbott B.J., Mayo J.G., Shoemaker R.H. and Boyd M.R. Feasibility of drug screening with panels of human-tumor cell lines using a microculture tetrazolium assay. *Cancer Res.* 1988, 48, 589–601.
- ⁷⁹ DeRisi J.L., Iyer V.R. and Brown P.O. Exploring the metabolic and genetic control of gene expression on a genomic scale. *Science* 1997, 278, 680–686.
- ⁸⁰ Cui D., Tian F., Kong Y., Igor T. and Gao H. Effect of single wall carbon nanotubes on polymerase chain reaction. *Nanotechnology* 2004, 15, 154–158.
- ⁸¹ Cui D., Ozkan C.S. Ravindran S., Kong, Y. and Gao, H. Encapsulation of Pt-labelled DNA molecules inside carbon nanotubes. *Mech. Chem. Biosystems* 2004, 1, 113–121
- ⁸² Sherr C.J. and Roberts J.M. Inhibitors of mammalian G1 cyclin-dependent kinases. *Genes Dev.* 1995, 9, 1149–1163.
- ⁸³ Baldin V., Lukas J., Marcote M.J., Pagano M. and Draetta G. Cyclin D1 is a nuclear protein required for cell cycle progression in G1. *Genes Dev.* 1993, 7, 812–821.
- ⁸⁴ Liu D.X. and Greene L.A. Neuronal apoptosis at the G1/S cell cycle checkpoint. *Cell Tissue Res.* 2001, 305, 217–228.
- ⁸⁵ Reed J.C. Bcl-2 family proteins: regulations of apoptosis and chemoresistance in hematologic malignancies. *Semin. Hematol.* 1997, 34, 9–19.
- ⁸⁶ Boudreau N., Sympton C.J., Werb Z., Bissell M.J. Suppression of ICE and apoptosis in mammary epithelial cells by extracellular matrix. *Science* 1995, 267, 891–893.
- ⁸⁷ Karuri N. W., Liliensiek S., Teixeira A. I., Abrams G., Campbell S., Nealey P. F. and Murphy C. J. Biological length scale topography enhances cell-substratum adhesion of human corneal epithelial cells. *J. Cell Science* 2004, 117, 3153–3164.
- ⁸⁸ Foley J. D.; Grunwald E. W.; Nealey P. F. and Murphy C. J. Topography modulates neuriteogenesis by PC12 cells cultured under sub-optimal conditions. *Biomaterials* 2005, 26, 3639–3644.
- ⁸⁹ Zhu B., Lu Q., Yin J., Hu J. and Wang Z. Effects of laser-modified polystyrene substrate on CHO cell growth and alignment. *Journal of Biomedical Materials Research Part B: Applied Biomaterials* 2004, 70B, 43–48.
- ⁹⁰ Arnold M., Cavalcanti-Adam E. A., Glass R., Blümmel J., Eck W., Kanthlener M., Kessler H. and Spatz J. P. Activation of integrin function by nanopatterned adhesive interfaces. *Chemphyschem* 2004, 5, 383–388.
- ⁹¹ Bovey F.A. and Winslow F.H. Macromolecules and introduction to polymer science. 1981 Academic press ISBN 0-12-119756-5.

REFERENCES

- ⁹² Kartini I., Menzies D., Blake D., Riches J.D. and Lu G.Q. Hydrothermal Seeded Synthesis of Mesoporous Titania for Application in Dye-Sensitized Solar Cells", *J. Mat. Chem.* 2004, 14, 2917-2921.
- ⁹³ Yokoyama M., Anazawa H., Takahashi A. and Inoue S. Synthesis and permeation behavior of membranes from segmented multiblock copolymers containing poly(ethylene oxide) and poly(b-benzyl L-aspartate) blocks. *Makromol Chem* 1990,191, 301-311.
- ⁹⁴ Mol A., van Lieshout M.I., Dam G.C., Hoerstrup S.P., Baaijens F.P.T. and Bouten C.V.C. Fibrin as a cell carrier in cardiovascular tissue engineering applications, *Biomaterials* 2005, 26, 3113-3121.
- ⁹⁵ Driessen N. J. B., Bouten C. V. C. and Baaijens F. P. T. A structural constitutive model for collagenous cardiovascular tissues incorporating the angular fiber distribution. *J. Biomech. Engng.* 2005, 127, 494-503.
- ⁹⁶ Hubbell J. A. Bioactive biomaterials. *Curr. Op. Biotech.* 10, 1999, 123-129.
- ⁹⁷ Bakker D., van Blitterswijk C. A., Hesseling S. C., Koerten H. K., Kuijpers W. and Grote J. J. Biocompatibility of a polyether urethane, polypropylene oxide, and a polyether-polyester copolymer. A qualitative and quantitative study of three alloplastic tympanic membrane materials in the rat middle ear. *J. Biomed. Mater. Res.* 1990, 24, 489-515.
- ⁹⁸ Radder A.M., Leenders H. and van Blitterswijk C.A. Bone-bonding behavior of poly(ethylene oxide)Dpoly(butylene terephthalate) copolymer coatings and bulk implants: a comparative study. *Biomaterials* 1995, 16, 507-513.
- ⁹⁹ Hesel U. Dahmen C. Kessler H. RGD modified polymers: biomaterials for stimulated cell adhesion and beyond. *Biomaterials* 2003, 24, 4385-4415.
- ¹⁰⁰ Ferruti P., Penco M., D'Addato P., Ranucci E. and Deghenghi R. Synthesis and properties of novel block copolymers containing poly(lactic-glycolic acid) and poly(ethylene glycol) segments. *Biomaterials* 1995, 16, 1423-1428.
- ¹⁰¹ Nishimura T., Sato Y., Yokoyama M., Okuya M. and Inoue S. Adhesion behavior of rat lymphocytes on poly(c-benzyl L-glutamate) derivatives having hydroxyl groups or poly(ethylene glycol) chains. *Makromol. Chem.* 1984, 185, 2109-2116.
- ¹⁰² Wang S. G., Chen C. F., Li Z. F., Li X. F. and Gu H. Q. Mixed polyetherpolyester multiblock copolymer and its blood compatibility. *J. Macromol. Sci. Chem.* 1989, A26, 505-518.
- ¹⁰³ Tziampazis E., Kohn J. and Moghe V. PEG-variant biomaterials as selectively adhesive protein templates: model surfaces for controlled cell adhesion and migration *Biomaterials* 2000, 21, 511-520.
- ¹⁰⁴ Pfaff M., Tangemann K., Muller B., Gurrath M., Muller G., Kessler H., Timpl R. and Engel J. Selective recognition of cyclic RGD peptides of NMR defined conformation by $\alpha_{II}\beta_3$, $\alpha_v\beta_3$ and $\alpha_5\beta_1$ integrins. *J. Biol. Chem.* 1994, 269, 20233-20238.

-
- ¹⁰⁵ Wu C., Bauer J. S., Juliano R. L. and McDonald J. A. The $\alpha 5 \beta 1$ integrin fibronectin receptor, but not the $\alpha 5$ cytoplasmic domain, functions in an early and essential step in fibronectin matrix assembly. *J. Biol. Chem.* 1993, 268, 21833-21888.
- ¹⁰⁶ Wennerberg K., Lohikangas L., Gullberg D., Pfaff M., Johansson S. and Fässler R. Beta 1 integrin-dependent and -independent polymerization of fibronectin, *J. Cell. Biol.* 1996, 132, 227-238.
- ¹⁰⁷ Mosher D. F., Sottile J., Wu C. and McDonald J. A. Assembly of extracellular matrix. *Curr. Opin. Cell Biol.* 1992, 4, 810-818.
- ¹⁰⁸ Main A. L., Harvey T.S., Baron M., Boyd J. and Campbell I.D. The three-dimensional structure of the tenth type III module of fibronectin: an insight into RGD-mediated interactions. *Cell* 1992, 71, 671-678.
- ¹⁰⁹ Pierschbacher M. D. and Ruoslahti E. Influence of stereochemistry of the sequence Arg-Gly-Asp-Xaa on binding specificity in cell adhesion. *J. Biol. Chem.* 1987, 262, 17294-17298.
- ¹¹⁰ Pierschbacher M. D., Ruoslahti E. Variants of the cell recognition site of fibronectin that retain attachment-promoting activity. *Proc Natl Acad Sci USA*, 1984, 81, 5985-5988.
- ¹¹¹ Müller G., Gurrath M., Kessler H. and Timpl R. Dynamic Forcing, a Method for Evaluating Activity and Selectivity Profiles of RGD (Arg-Gly-Asp) Peptides. *Angew. Chem. Int. Ed. Engl.* 1992, 31, 326-328.
- ¹¹² Massia S. P. and Hubbell J. A. An RGD Spacing of 440 nm Is Sufficient for Integrin $\alpha_v \beta_3$ -mediated Fibroblast Spreading and 140 nm for Focal Contact and Stress Fiber Formation. *The Journal of Cell Biology* 1991, 114, 1089-1100.
- ¹¹³ Dee K. C., Rueger D. C., Andersen T. T. and Bizios R. Conditions which promote mineralization at the bone-implant interface: a model *in vitro* study. *Biomaterials* 1996, 17, 209-215.
- ¹¹⁴ Rezania A., Thomas C. H., Branger A. B., Waters C. M. and Healy K. E. The detachment strength and morphology of bone cells contacting materials modified with a peptide sequence found within bone sialoprotein. *J. Biomed. Mater. Res.* 1997, 37, 9-19.
- ¹¹⁵ McFarland C. D., Mayer S., Scotchford C., Dalton B. A., Steele J. G. and Downes S. Attachment of cultured human bone cells to novel polymers. *J. Biomed. Mater. Res.* 1999, 44, 1-11.
- ¹¹⁶ Grzesik W. J., Ivanov B., Robey F. A., Southerland J. and Yamauchi M. Synthetic integrin binding. Peptides promote adhesion and proliferation of human periodontal ligament cells *in vitro*. *J Dent Res* 1998, 77, 1606-1612.
- ¹¹⁷ Haubner R., Bruchertseifer F., Bock M., Kessler H., Schwaiger M. and Wester H. J. Synthesis and biological evaluation of a (99m)Tc-labelled cyclic RGD peptide for imaging the $\alpha_v \beta_3$ integrins expression. *Nuclearmedicine* 2004, 43, 26-32.

REFERENCES

-
- ¹¹⁸ Anzai J., Kobayashi Y., Nakamura N., Nishimura M. and Hoshi T. Layer-by-Layer Construction of Multilayer Thin Films Composed of Avidin and Biotin-Labeled Poly(amine)s. *Langmuir* 1999, 15, 221-226.
- ¹¹⁹ Zhu H. and Snyder M. Protein arrays and microarrays. *Curr. Opin. Chem. Biol.* 2001, 5, 40-45.
- ¹²⁰ Pathak S., Singh A. K., McElhanon J. R. and Dentinger P. M. Dendrimer-Activated Surfaces for High Density and High Activity Protein Chip Applications. *Langmuir*, 2004, 20, 6075-6079
- ¹²¹ Yang X.B., Roach H.I., Clarke N.M., Howdle S.M., Quirk R., Shakesheff K.M. and Oreffo R.O. Human osteoprogenitor growth and differentiation on synthetic biodegradable structures after surface modification. *Bone* 2001, 29, 523-531.
- ¹²² Craig W.S., Cheng S., Mullen D.G., Blevitt J. and Pierschbacher M.D. Concept and progress in the development of RGD-containing peptide pharmaceuticals. *Biopolymers* 1995, 37, 157-175
- ¹²³ Varani J., Inman D.R., Fligiel S.E. and Hillegas W.J., Use of recombinant and synthetic peptides as attachment factors for cells on microcarriers. *Cytotechnology* 1993, 13, 89-98.
- ¹²⁴ Quirk R.A., Chan W.C., Davies M.C., Tendler S.J.B. and Shakesheff K.M. Poly(L-lysine)-GRGDS as a biomimetic surface modifier for poly(lactic acid). *Biomaterials* 2001, 22, 865-872.
- ¹²⁵ Besselink G. A. J., Beugeling T. and Bantjes A. N-hydroxysuccinimide-activated glycine-sepharose—hydrolysis of activated groups and coupling of amino-compounds. *Appl. Biochem. Biotechnol.* 1993, 43, 227-246.
- ¹²⁶ Morpurgo M., Bayer E. A. and Wilchek M., N-hydroxysuccinimide carbonates and carbamates are useful reactive reagents for coupling ligands to lysines on proteins. *J. Biochem. Biophys. Methods.* 1999, 38, 17-28.
- ¹²⁷ Kugo K., Okuno M., Masuda K., Nishino J., Masuda H. and Iwatsuki M. Fibroblast attachment to Arg-Gly Asp peptide-immobilized poly(γ -methyl L-glutamate). *J. Biomater. Sci. Polym. Ed.* 1994, 5, 325-337.
- ¹²⁸ Neff J. A., Caldwell K. D. and Tresco P. A. A novel method for surface modification to promote cell attachment to hydrophobic substrates. *J. Biomed. Mater. Res.* 1998, 40, 511-519.
- ¹²⁹ Ivanov B., Grzesik W. and Robey F.A. Synthesis and use of a new bromoacetyl-derivatized heterotrifunctional amino acid for conjugation of cyclic RGD-containing peptides derived from human bone sialoprotein. *Bioconjug. Chem.* 1995, 6, 269-277.
- ¹³⁰ Scheibler L., Dumy P., Boncheva M., Leufgen K., Mathieu H.-J., Mutter M. and Vogel H. Functional molecular thin films: topological templates for the chemoselective ligation of antigenic peptides to self-assembled monolayers. *Angew. Chem. Int. Ed.* 1999, 38, 696-699.
- ¹³¹ Mol A., van Lieshout M.I., Dam G.C., Hoerstrup S.P., Baaijens F.P.T., Bouten C.V.C., Fibrin as a cell carrier in cardiovascular tissue engineering applications. *Biomaterials* 2005, 26, 3113-3121.

-
- ¹³² Yokoyama M., Anazawa H., Takahashi A. and Inoue S. Synthesis and permeation behavior of membranes from segmented multiblock copolymers containing poly(ethylene oxide) and poly(b-benzyl L-aspartate) blocks. *Macromol. Chem.* 1990, 191, 301-311.
- ¹³³ Shim J., Bersano-Begey T.F., Zhu X., Tkaczyk A.H. and Linderman J. J. Micro- and Nanotechnologies for Studying Cellular Function Takayama S. *Current Topics in Medicinal Chemistry* 2003, 3, 687-703.
- ¹³⁴ Singhvi R., Kumar A., Lopez G., Stephanopoulos G. N., Wang D. I. C., Whitesides G. M., Ingber D. E. Engineering cell shape and function. *Science* 1994, 264, 696-698.
- ¹³⁵ Dike L., Chen C.S., Mrkisch M., Tien J., Whitesides G.M and Ingber DE. Geometric control of switching between growth, apoptosis, and differentiation during angiogenesis using micropatterned substrates. *In Vitro Cell Dev. Biol.* 1999, 35, 441-448.
- ¹³⁶ Lopez G. P., Albers M. W., Schreiber S. L., Carroll R., Peralta E. and Whitesides G. M. Convenient methods for patterning the adhesion of mammalian cells to surfaces using self-assembled monolayers of alkanethiolates on gold . *J. Am. Chem. Soc.* 1993, 115, 5877-5878.
- ¹³⁷ Curtis A.S., Casey B., Gallagher J.O., Pasqui D. and Wood M.A. Wilkinson C.D. Substratum nanotopography and the adhesion of biological cells. Are symmetry or regularity of nanotopography important? *Biophys. Chem.* 2001, 94, 275-283.
- ¹³⁸ Spatz J. P., Mößmer S., Möller M., Herzog T., Boyen H.G., Ziemann P. and Kabius B. Metal and Metaloxide Nanodot Pattern by Means of a Diblock Copolymer Template *Langmuir* 2000, 16, 407-415.
- ¹³⁹ Spatz J. P., Sheiko S. and Moller M. Ion-Stabilized Block Copolymer Micelles: Film Formation and Intermicellar Interaction. *Macromolecules* 1996, 29, 3220-3226.
- ¹⁴⁰ Hamley, I.W. Nanostructured fabrication using block copolymers. *Nanotechnology* 2003, 14, R39-R54.
- ¹⁴¹ Korgel B. A. and Fitzmaurice D. Condensation of Ordered Nanocrystal Thin Films. *Physical review letters* 1998, 80, 3531-3534.
- ¹⁴² Lee W., Hara M., Lee H. Construction of molecular probe on Au surface for detecting the tri-strand β -sheet structure. *Materials Science & Engineering.* 2004, 315-317.
- ¹⁴³ Kralchevsky P. A., Paunov V. N., Ivanov I. B. and Nagayama K. Capillary meniscus interaction between colloidal particles attached to a liquid—fluid interface. *J. colloid interface sci.* 1992, 151, 79-94.
- ¹⁴⁴ Denkov N. D., Velev O. D., Kralchevsky P. A., Ivanov I. B., Yoshimura H. and Nagayamat K. Mechanism of Formation of Two-Dimensional Crystals from Latex Particles on Substrates. *Langmuir* 1992, 8, 3183-3190.

REFERENCES

- ¹⁴⁵ Michel M., Aichinger P-A., Kolodziejczyk E., Sagalowicz L., Hughes E., Watzke H.J. and Leser M.E. Application of self-assembly principles in foods. Nanotech 2005 Conference Program.
- ¹⁴⁶ Morkved T. L., Lu M., Urbas A. M., Ehrichs E. E., Jaeger H. M., Mansky P., and Russell T. P. Local Control of Microdomain Orientation in Diblock Copolymer Thin Films with Electric Fields. *Science* 1996, 273, 931-933.
- ¹⁴⁷ Lin X. M., Parthasarathy R., and Jaeger M H. Direct patterning of self-assembled nanocrystal monolayers by electron beams. *Applied Physics Letters* 2001, 78, 1915-1917.
- ¹⁴⁸ Spatz J. P., Eibeck P., Möller M., Kramarenko E. Yu., Khalatur P. G., Potemkin I. I., Khokhlov A. R., Winkler R.G. and Reineker P. Order-Disorder Transition of Lateral Phase Separated Diblock Copolymer Films. *Macromolecules* 2000, 33, 150-157.
- ¹⁴⁹ Spatz J. P., Mößmer S., Kamm F.-M., Plettl A., Ziemann P. and Möller M. A combined top down / bottom up approach for nanolithography. *Advanced Materials* 2002, 14, 1827-1831.
- ¹⁵⁰ Dalby M.J., Silvio L.D., Harper E.J., Bonfield W. In vitro adhesion and biocompatibility of osteoblast-like cells to poly(methylmethacrylate) and poly(ethylmethacrylate) bone cements. *J Mater Sci Mater Med* 2002, 13, 311-314.
- ¹⁵¹ Curtis A.S., Gadegaard N., Dalby M.J., Riehle M.O., Wilkinson C.D. and Aitchison G. Cells react to nanoscale order and symmetry in their surroundings. *IEEE Trans Nanobioscience* 2004, 3, 61-65.
- ¹⁵² Maheshwari G., Brown G, Lauffenburger D. A., Wells A., and Griffith L. G. Cell adhesion and motility depend on nanoscale RGD clustering. *J. Cell Sci.* 2000 113: 1677-1686.
- ¹⁵³ Maheshwari G., Wells A., Griffith L. G. and Lauffenburger D. A. Biophysical Integration of Effects of Epidermal Growth Factor and Fibronectin on Fibroblast Migration. *Biophysical J.* 1999, 76, 2814-2823.
- ¹⁵⁴ Cavalcanti-Adam E.A. The control of cell adhesion and adhesion-dependent events by nanotemplates regulating the spatial arrangement of integrin ligands. Heidelberg, Univ., Diss., 2005.
- ¹⁵⁵ Danilov Y. N. and Juliano R. L. (Arg---Gly---Asp)_n-Albumin conjugates as a model substratum for integrin-mediated cell adhesion. *Exp. Cell Res*, 1989, 182, 186-196.
- ¹⁵⁶ Singer I.I., Kawka D.W., Scott S., Mumford R.A. and Lark M.W. The fibronectin cell attachment sequence Arg-Gly-Asp-Ser promotes focal contact formation during early fibroblast attachment and spreading *J. Cell Biol.* 1987, 104, 573-584.
- ¹⁵⁷ Brandley B.K., Schnaar R.L. Covalent attachment of an Arg-Gly-Asp sequence peptide to derivatizable polyacrylamide surfaces: support of fibroblast adhesion and long-term growth. *Anal Biochem.* 1988, 172, 270-278.

-
- ¹⁵⁸ Sofia S.J., Kuhl P.R., and Griffith L.G. Methods for the preparation and use of tethered ligands as biomaterials and tools for cell biology. *Methods in Tissue Engineering*, M.L. Yarmush and J. Morgan, eds., Humana Press 1998.
- ¹⁵⁹ Darrell J. Irvine, Kerri-Ann Hue, Anne M. Mayes, and Linda G. Griffith Simulations of Cell-Surface Integrin Binding to Nanoscale Clustered Adhesion Ligands. *Biophys. J.* 2002, 82, 120-132.
- ¹⁶⁰ Irvine, D.J., Hue, K.A., Mayes, A.M., and Griffith, L.G. Simulations of cell surface integrin binding to nanoscale clustered adhesion ligands. *Biophys. J* 2002, 82, 120-132.
- ¹⁶¹ Wright T. and McGechan A. Breast cancer: new technologies for risk assessment and diagnosis. *Mol. Diagn.* 2003, 7, 49-55.
- ¹⁶² Cao J.N., Gao T.W., Giuliano A.E. and Irie R.F. Recognition of an epitope of a breast cancer antigen by human antibody. *Breast Cancer Res. Treat.* 1999, 53, 279-290.
- ¹⁶³ Young R.A. and Davis R.W. Efficient isolation of genes by using antibody probes. *Proc. Natl. Acad. Sci. USA* 1983, 80, 1194-1198.
- ¹⁶⁴ Winters Z.E., Leek R.D., Bradburn M.J., Norbury C.J. and Harris A.L. Cytoplasmic p21WAF1/ CIP1 expression is correlated with HER-2/ neu in breast cancer and is an independent predictor of prognosis. *Breast Cancer Res.* 2003, 5, R242-249.
- ¹⁶⁵ Kim M.S., Lee E.J., Kim H.R. and Moon A. p38 kinase is a key signaling molecule for H-Ras-induced cell motility and invasive phenotype in human breast epithelial cells. *Cancer Res* 2003, 63, 5454-5458.
- ¹⁶⁶ Wu K., Weng Z. and Tao Q. Stage specific expression of breast cancer-specific gene g synuclein. *Cancer Epidemiol, Biomarkers & Prev.* 2003, 12, 920-925.
- ¹⁶⁷ Greenberg R., Barnea Y., Schneebaum S., Kashtan H., Kaplan O. and Skornik Y. Detection of hepatocyte growth factor/scatter factor receptor (c-Met) and MUC1 from the axillary fluid drainage in patients after breast cancer surgery. *Isr. Med. Assoc. J.* 2003, 5, 649-652.
- ¹⁶⁸ Kotera Y., Fontenot J.D., Pecher G., Metzgar R.S. Humoral immunity against a tandem repeat epitope of human mucin MUC-1 in sera from breast, pancreatic, and colon cancer patients. *Cancer Res* 1994, 54, 2860-2865.
- ¹⁶⁹ Gaforio J.J., Serrano M.J., Sanchez-Rovira P. Detection of breast cancer cells in the peripheral blood is positively correlated with estrogen-receptor status and predicts for poor prognosis. *Int. J. Cancer* 2003, 107, 984-990.
- ¹⁷⁰ Samuel S.K., Minish T.M., Davie J.R. Nuclear matrix proteins in well and poorly differentiated human breast cancer cell lines. *J. Cell Biochem.* 1997, 66, 9-15.
- ¹⁷¹ Kler C.G., Cao Q., Varambally S. EZH2 is a marker of aggressive breast cancer and promotes neoplastic transformation of breast epithelial cells. *Proc. Natl. Acad. Sci. USA* 2003, 100, 11606-11611.

REFERENCES

- ¹⁷² Cao J.N., Gao T.W., Giuliano A.E., Irie R.F. RBP1L1, a retinoblastomabinding protein-related gene encoding an antigenic epitope abundantly expressed in human carcinomas and normal testis. *J. Natl. Cancer Inst.* 2001, 93, 1159-1165.
- ¹⁷³ Fattaey A.R., Helin K., Dembski M.S. Characterization of the retinoblastoma binding proteins RBP1 and RBP2. *Oncogene* 1993, 8, 3149-3156.
- ¹⁷⁴ Sahin U., Tureci O., Schmitt H., Cochlovirus B. Human neoplasmas elicit multiple specific immune responses in the autologous host. *Proc. Natl. Acad. Sci.* 1995, 92, 11810-11813.
- ¹⁷⁵ Liu Z., Hansen M., Womack J.E., Antoniou E. A comparative map of interstitial bovine chromosome 5 with human chromosomes 12 and 22. *Cytogenet Genome Res* 2003, 101, 147-154.
- ¹⁷⁶ Mihaila D., Gutierrez J.A., Rosenblum M.L., Newsham I.F., Bogler O., Rempel S.A. NABTT CNS Consortium. Meningiomas: analysis of loss of heterozygosity on chromosome 10 in tumor progression and the delineation of four regions of chromosomal deletion in common with other cancers. *Clin Cancer Res* 2003, 9, 4435-4442.
- ¹⁷⁷ Hidetoshi K., Akinori S. Structure-based prediction of DNA target sites by regulatory proteins. *Proteins* 1999, 35, 114-131.
- ¹⁷⁸ Zubay G. In vitro synthesis of protein in microbial systems. *Annu. Rev. Genet.* 1973, 7, 267-287.
- ¹⁷⁹ Afanassiev V., Troppmair J., Schuler M. Production and characterization of monoclonal antibodies against human BAD protein. *Hybridoma*. 1998, 17, 383-387.
- ¹⁸⁰ Mattes M.J., Thomson T.M., Old L.J., Lloyd K.O. A pigmentation associated, differentiation antigen of human melanoma defined by a precipitating antibody in human serum. *Int. J. Cancer*. 1983, 32, 717-721.
- ¹⁸¹ Sambrook J., Fritsch E.F. and Maniatis T. Molecular cloning, a laboratory manual. 2nd ed. Cold Spring Harbor Laboratory Press; 1989, 538-598.
- ¹⁸² Chen Y., Chen C.F. and Riley L. Aberrant subcellular location of BRCA1 in breast cancer. *Science* 1995;270:789-91.
- ¹⁸³ Breitman L., Friedman J. and Olshen R., Monterey C.S. Classification and regression trees. CA: Wadsworth, 1984.
- ¹⁸⁴ Hosmer D.W. and Lemeshow S. Applied logistic regression. New York: John Wiley & Sons, 1989.
- ¹⁸⁵ Disis M.L., Calenoff E. and Mclaughlin G. Existent T cell and antibody immunity to HER-2/new protein in patients with breast cancer. *Cancer Res* .1994, 54, 16-20.

-
- ¹⁸⁶ Choi D.H., Shin D.B. and Lee M.H. A comparison of five immunohistochemical biomarkers and HER-2/neu gene amplification by fluorescence in situ hybridization in white and Korean patients with early-onset breast carcinoma. *Cancer* 2003, 98, 1587-1595.
- ¹⁸⁷ Perczel A., Jakli I. and Csizmadia I.G. Intrinsically stable secondary structure elements of proteins: a comprehensive study of folding units of proteins by computation and by analysis of data determined by X-ray crystallography. *Chemistry* 2003, 9, 5332-5342.
- ¹⁸⁸ Zhao Y., Pinilla C., Valmori D., Martin R. and Simon R. Application of support vector machines for T-cell epitopes prediction. *Bioinformatics* 2003, 19, 1978-1984.
- ¹⁸⁹ Nevins J.R. The Rb/E2F pathway and cancer. *Hum. Mol. Genet.* 2001, 10, 699-703.
- ¹⁹⁰ Bremner R., Miska E.A., McMance D.J., Reid J.L., Bannister A.J. and Kouzarides T. Retinoblastoma protein recruits histone deacetylase to repress transcription. *Nature* 1998, 391, 597-601.
- ¹⁹¹ Albert L., Brian K. and David A.B. RBP1 recruits the mSIN3-Histone deacetylase complex to the pocket of retinoblastoma tumor suppressor family proteins found in limited discrete regions of the nucleus at growth arrest. *Mol. Cell Biol.* 2001, 21, 2918-2941.
- ¹⁹² Das A.K., Mitra D. and Harboe M. Predicted molecular structure of the mammalian cell entry protein Mce1A of Mycobacterium tuberculosis. *Biochem. Biophys. Res. Commun.* 2003, 302, 442-447.
- ¹⁹³ Spirin A.S., Baranov V.I., Ryabova L.A., Ovodov S.Y. and Alkhov Y.B. A continuous cell-free translation system capable of producing polypeptides in high yield. *Science* 1988, 242, 1162-1164.
- ¹⁹⁴ Chebil G., Bendahl P.O., Idvall I. and Ferno M. Comparison of immunohistochemical and biochemical assay of steroid receptors in primary breast cancer—clinical associations and reasons for discrepancies. *Acta. Oncol.* 2003, 42, 719-725.
- ¹⁹⁵ . Dodin S., Blanchet C. and Marc I. Phytoestrogens in menopausal women: a review of recent findings. *Med. Sci. (Paris)* 2003, 19, 1030-1037.
- ¹⁹⁶ Balleine R.L., Earl M.J., Greenberg M.L. and Clarke C.L. Absence of progesterone receptor associated with secondary breast cancer in postmenopausal women. *Br. J. Cancer* 1999, 79, 1564-1571.
- ¹⁹⁷ Muss H.B. Adjuvant therapy for older women with breast cancer. *Breast* 2003, 12, 550-557.
- ¹⁹⁸ Levine M., Moutquin J.M., Walton R. and Feightner J. Early breast cancer trialists collaborative group. Tamoxifen for early breast cancer: an overview of the randomized trials. *Lancet* 1998, 351, 1451-1467.
- ¹⁹⁹ Stevens R.G. Re: "Risk of premenopausal breast cancer and use of electric blankets". *Am. J. Epidemiol.* 1995, 142, 446-447.

REFERENCES

- ²⁰⁰ Loomis D.P., Savitz D.A. and Ananth C.V. Breast cancer mortality among female electrical workers in the United States. *J. Natl. Cancer Inst.* 1994, 86, 921-925.
- ²⁰¹ Thangaraju M., Kaufmann S.H. and Couch F.J. BRCA1 facilitates stress-induced apoptosis in breast and ovarian cancer cell lines. *J. Biol. Chem.* 2000, 275, 33487-33496.
- ²⁰² Lafarge S., Sylvain V., Ferrara M. and Bignon Y.J. Inhibition of BRCA1 leads to increased chemoresistance to microtubule-interfering agents, an effect that involves the JNK pathway. *Oncogene* 2001, 4, 65976-65606.
- ²⁰³ Harkin D.P., Bean J.M., Miklos D., Song Y.H., Truong V.B., Englert C., Christians F.C., Ellisen L.W., Maheswaran S., Oliner J.D. and Haber D.A. Induction of GADD45 and JNK/SAPK-dependent apoptosis following inducible expression of BRCA1. *Cell* 1999, 97, 575-586.
- ²⁰⁴ Jia M.C., Ravindranath N., Papadopoulos V. and Dym M. Regulation of c-fos mRNA expression in Sertoli cells by cyclic AMP, calcium, and protein kinase C mediated pathways. *Mol. Cell Biochem.* 1996, 156, 43-49.
- ²⁰⁵ Jahreis G.P., Johnson P.G., Zhao Y.L. and Hui S.W. Absence of 60-Hz, 0.1-mT magnetic field-induced changes in oncogene transcription rates or levels in CEM-CM3 cells. *Biochim. Biophys. Acta.* 1998, 1443, 334-342.
- ²⁰⁶ Berg H. Problems of weak electromagnetic field effects in cell biology. *Bioelectrochem. Bioenerg.* 1993, 48, 355-360.
- ²⁰⁷ Miyakoshi J., Yoshida M., Yaguchi H., Ding G.R. Exposure to extremely low frequency magnetic fields suppresses x-ray-induced transformation in mouse C3H10T1/2 cells. *Biochem. Biophys. Res. Commun.* 2000, 272, 323-327
- ²⁰⁸ Gartel A.L. and Shchors K. Mechanisms of c-myc-mediated transcriptional repression of growth arrest genes. *Exp. Cell Res.* 2003, 283, 17-21.
- ²⁰⁹ Campbell-Beachler M., Ishida-Jones T., Haggren W. and Phillips J.L. Effect of 60 Hz magnetic field exposure on c-fos expression in stimulated PC12 cells. *Mol. Cell Biochem.* 1998, 189, 107-111.
- ²¹⁰ Phillips J.L., Haggren W., Thomas W.J., Ishida-Jones T. and Adey W.R. Magnetic field-induced changes in specific gene transcription. *Biochim Biophys Acta.* 1992, 1132, 140-144.
- ²¹¹ Lin H., Han L., Blank M., Head M. and Goodman R. Magnetic field activation of protein-DNA binding. *J. Cell. Biochem.* 1998, 70, 297-303.
- ²¹² Fanelli C., Coppola S., Barone R., Colussi C., Gualandi G., Volpe P. and Ghibelli L. Magnetic fields increase cell survival by inhibiting apoptosis via modulation of Ca²⁺ influx. *FASEB J.* 1999, 13, 95-102.